Normalised Transverse Emittance Reduction via Ionisation Cooling in MICE 'Flip Mode'

Paul Bogdan Jurj

Supervised by Jaroslaw Pasternak

Department of Physics

Imperial College London

A thesis submitted in fulfilment of the requirements for the degree of Doctor of Philosophy at Imperial College London

May 2022

Abstract

Low-emittance muon beams are central to the development of a Muon Collider and can significantly enhance the performance of a Neutrino Factory. The main challenge for muon acceleration stems from the large emittance with which the muon beam is produced. Maximising the muon yield while maintaining a suitably small aperture in the accelerator system requires that the muon beam emittance be reduced (cooled). The international Muon Ionisation Cooling Experiment (MICE) was designed to demonstrate the feasibility of the ionisation cooling technique, and provide the first measurement of normalised transverse emittance reduction in a muon beam.

This work focuses on the emittance reduction analysis of 140 MeV/c MICE muon beams that passed through a liquid hydrogen or a lithium hydride absorber. During the acquisition of the studied data sets, the magnetic channel produced a field that flipped polarity at the absorber, to prevent a canonical angular momentum increase. A novel beam sampling procedure was developed to account for imperfections in beam matching at the entrance into the cooling channel, which improved the cooling signal measurement. A reduction in the muon beam normalised transverse emittance that grows linearly with input emittance was observed, which is a clear signal of ionisation cooling. The measurement is consistent with the simulation and the theoretical model.

Furthermore, both the liquid hydrogen and the lithium hydride absorbers were found to induce a reduction in the mean canonical angular momentum of the beam. This effect can be attributed to energy loss at the absorber situated at the field polarity flip, combined with an increasing beam size across the absorber region. This result confirms that the field polarity flip at the absorber would maintain a low-magnitude canonical angular momentum within the cooling stage of a future muon facility.

Acknowledgements

First, I wish to express my gratitude to my supervisor, Jaroslaw, for giving me the opportunity to pursue a PhD in High Energy Physics. His uninterrupted support and guidance throughout the last four years were of great value. I would also like to show my appreciation to the MICE collaboration, which made the analyses presented in this thesis possible. In particular, I want to thank Chris Hunt for patiently introducing me to the analysis software, Paolo for going above and beyond in helping me with MAUS-related headaches, and Chris Rogers, Kenneth Long, Dan Kaplan, Paul Soler and John Cobb for the vast amounts of shared MICE wisdom and their insightful suggestions.

I am eternally grateful to my girlfriend, Sânziana, who has supported and endured an overly anxious boyfriend for a heroic amount of time, and found the energy to give me the confidence I sometimes lacked. Very special thanks to my parents who have supported me in every way throughout my academic pursuits ever since I left home 12 years ago.

Finally, I also wish to extend my thanks to the friends I made along the way – in particular, Alexa for the entertaining stories and amazing food, and Lewis and Maria for all the useful advice, and especially for our long chats in the improvised pandemic office / thesis writing den.

Declaration of Originality

The work in this thesis is my own unless explicitly stated otherwise. Chapter 1 contains a brief description of the main motivations for the construction of the Muon Ionisation Cooling Experiment. Chapter 2 reviews the theoretical concepts used throughout this thesis. Chapter 3 provides a detailed description of the Muon Ionisation Cooling Experiment, based on MICE publications and internal notes. In all three chapters, the literature resources are referenced where appropriate.

Chapters 4 and 5 detail the analysis efforts that were carried out personally. Both analyses employ reconstruction, simulation and analysis tools built in the MICE Analysis User Software (MAUS). The beam optics reconstruction and beam sampling algorithms used in Chapter 4 originate from work previously done by Christopher Hunt during his work on MICE, but their further development, testing and incorporation into the emittance reduction analysis are my own work.

Copyright Declaration

Contents

List of Tables

List of Figures

Chapter 1

Introduction

The discoveries of neutrino oscillations and the Higgs boson significantly shifted the outlook of particle physics. Even though the Higgs discovery by the Large Hadron Collider (LHC) at CERN [1][2] constitutes a remarkable experimental validation of the Standard Model (SM), no explicit signals of physics Beyond the Standard Model (BSM) have been detected thus far within the energy domain covered at LHC. New physics signals are crucial in the quest for understanding phenomena that are not prescribed by the SM, such as the matter-antimatter asymmetry, dark matter, dark energy or neutrino masses and flavor mixing.

The search for and study of BSM physics require machinery able to operate at the energy and intensity frontiers. Neutrino flavor mixing, a clear evidence of BSM phenomena, are described by the 3×3 PMNS (Pontecorvo, Maki, Nakagawa and Sakata) mixing matrix [3][4]. Precise measurements of the PMNS matrix parameters will help establish the degree to which the Charge-Parity (CP) symmetry is violated in the leptonic sector, and may shed light on the origins of neutrino mass or uncover further new physics. Such measurements require accelerating facilities able to provide intense neutrino beams with well-characterized fluxes and energy spectra. At the energy frontier, multi-TeV lepton-antilepton colliders able to perform precision measurements of the collision products are ideal candidates for both direct and indirect new physics searches.

1.1 Muon Acceleration

Muon-based accelerators have been considered as potential enablers for particle physics experiments at the energy and intensity frontiers. The benefit of using muons in circular colliders stems from being fundamental particles, which have a mass 207 times larger than that of electrons. The larger mass leads to a dramatic reduction in synchroton radiation losses, which scale as $1/m^4$. Furthermore, the spread in the effective centre-of-mass energy induced by beamstrahlung, the emission of radiation resulting from the interaction of a charged particle beam with the electric field produced by the incoming beam, is significantly lower for muons. Thus, a Muon Collider could achieve multi-TeV and precise centre-of-mass energies within a considerably smaller and more cost-effective facility than an electron-positron collider [5].

The potential of a Muon Collider is two-pronged. At multi-TeV level, it could serve as an exploratory machine [6], whereas at low energies, it could operate as a dedicated muon-based Higgs Factory and perform precision measurements of the Higgs resonance mass and width by directly scanning it [7].

The primary challenges in building a Muon Collider facility arise from the short muon lifetime (~ 2.2 μs at rest) and the difficulty to produce intense muon bunches with a small phase space volume. Due to its potential of generating intense beams, a muon source based on proton driver scheme has been pursued [5]. In this scheme, an intense proton beam impinges on a high-Z material target to produce a secondary beam composed primarily of pions and kaons. The pions and kaons decay into muons to create a so-called 'tertiary' muon beam. The resulting muon beam has an intrinsically large phase space volume, which must be reduced (cooled) to achieve efficient acceleration. The muon capture, cooling and acceleration must be executed on a time scale comparable to the muon lifetime at rest.

Furthermore, muon decays in a dedicated storage ring have been considered as a potential source for intense and well-characterized neutrino beams [8]. Such a facility, referred to as a Neutrino Factory, would enable the next generation of neutrino physics experiments. The current state-of-the-art technology for neutrino beam production relies on decays of charged pions created by a proton beam striking a graphite target. Due to the multiple decay modes of pions and kaons, which are also produced at the target, the resulting neutrino beam is mostly composed of ν_μ

(or $\bar{\nu}_\mu$), with a small $\bar{\nu}_\mu$ (or ν_μ), ν_e and $\bar{\nu}_e$ contamination. The limited precision with which the neutrino fluxes can be measured are an important systematic uncertainty in the oscillation analysis [9]. This limitation could be overcome at a Neutrino Factory, where muon decays ($\mu^+ \rightarrow e^+\nu_e\bar{\nu}_\mu$ or $\mu^- \rightarrow e^-\bar{\nu}_e\nu_\mu$) within a straight section of a storage ring would produce neutrino beams with a precisely determined composition.

The Neutrino Factory muon beams can be produced by the same proton driver source proposed for the Muon Collider. While cooling the muon beam is not a strict requirement, a moderate cooling stage has been considered to increase the number of muons that are transmitted into the acceleration stage [10].

The design and Research and Development (R&D) efforts for muon based facilities have culminated with the U.S. Muon Accelerator Program (MAP) [11]. The program was tasked to evaluate the feasibility of the technologies necessary for the building of a high intensity Neutrino Factory and a Muon Collider. As part of the program efforts, the Muon Accelerator Staging Study (MASS) [12] exploited the synergies between the Neutrino Factory and Muon Collider and developed a staged approach. Within this approach, each stage provides unique physics capabilities and serves as an R&D platform for the next stage.

The first proposed stage is a short baseline Neutrino Factory-like ring (such as NuSTORM [13]), which could be built with existing technologies and would facilitate sterile neutrino searches and neutrino cross-section measurements. This would be followed by a Neutrino Factory facility (NuMAX), which would serve as a tool for precision measurements in the neutrino sector. In the final stages, after the development of an adequate cooling stage and the construction of a collider ring, the facility could operate as a Higgs Factory or a multi-TeV Muon Collider. A diagram of the Neutrino Factory and Muon Collider staged facilities, as envisaged in the MAP studies, is shown in figure 1.1. It can be observed that the production, capture, initial cooling and linear acceleration systems are shared by the two facilities.

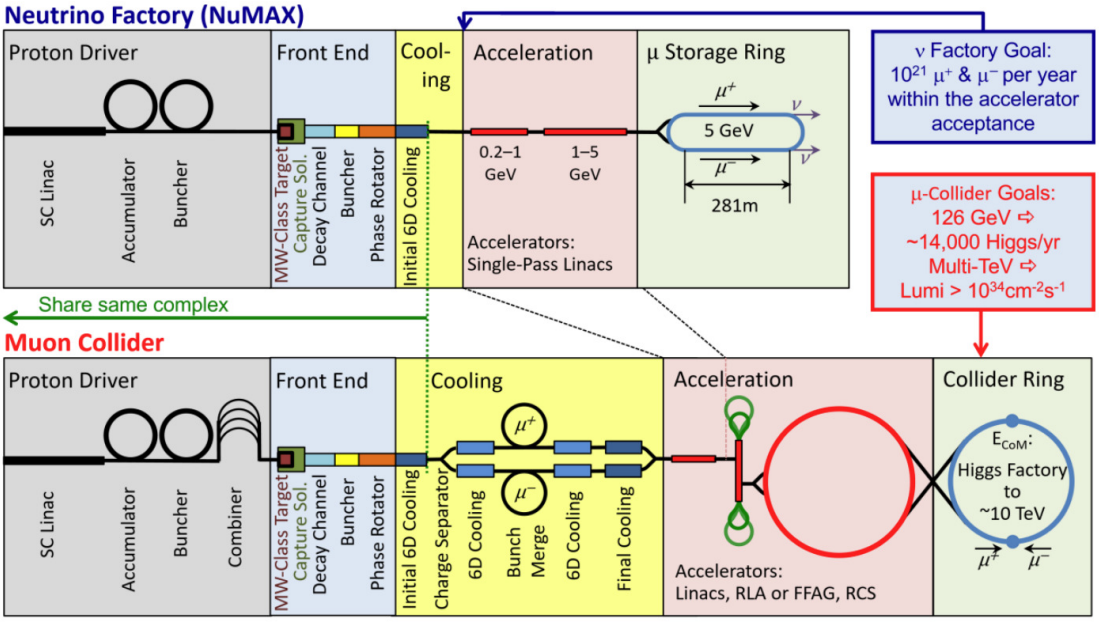

Figure 1.1: Diagram of (top) a Neutrino Factory and (bottom) a Muon Collider concept, with an emphasis on the synergies between various subsystems - the two concepts share the same muon production and initial cooling facilities [14].

1.2 Muon Cooling

As previously mentioned, a muon beam generated in the proton driver scheme has a large phase space volume due to the proton-target interaction and the pion decay kinematics. In order to achieve high intensity neutrino beams at a Neutrino Factory, or to fit a high brightness muon beam within the acceptance of the Muon Collider accelerating systems, the muon beam must be cooled.

Traditional cooling techniques such as stochastic cooling [15], electron cooling [16], synchrotron radiation cooling [17] or laser cooling [18] are impractical as the amount of time required to cool the beam adequately is longer than the muon lifetime. Ionisation cooling is the only technique by which the muon beam phase space volume can be adequately compressed before significant decay losses occur [19][20].

The Muon Ionisation Cooling Experiment (MICE) [21] was designed to provide a first demonstration of ionisation cooling and measure a reduction in the transverse muon beam emittance. A first analysis conducted by the MICE collaboration has demonstrated an unambiguous cooling signal by measuring an increase in the

number of muons with low amplitude upon passage through an absorber [22].

The work in this thesis focuses on the demonstration and quantification of the ionisation cooling signal in liquid hydrogen and lithium hydride absorbers, by measuring the reduction of the beam normalised transverse emittance. A novel beam sampling procedure is developed to recover the performance of the MICE cooling channel by selecting muon subsamples with optimal properties at the absorber.

Chapter 2

Beam Dynamics and Ionisation Cooling

In particle accelerators, stable and well controlled particles trajectories are required to ensure that the beam is contained within the apertures and that the beam acquires specific properties at certain locations, such as interaction points. In conventional accelerating structures, such as synchrotrons, this requirement is primarily achieved through dipole and quadrupole magnets used for beam steering and containment, respectively. In ionisation cooling lattices, beam confinement and strong focusing in the transverse phase space is provided by solenoid magnets, while longitudinally the beam is controlled by using radio frequency (RF) cavities.

The muon beam used in the MICE experiment, as well as those that would be used in proton-driven future muon accelerating facilities, have an intrinsically large phase space volume as tertiary beams produced via pion decay. Efficient acceleration and storage of the muon beams require that the phase space volume be reduced (cooled) before substantial decay occurs. Ionisation cooling is the technique proposed to cool muons, which is achieved via energy loss within an absorber material.

In this chapter, accelerator physics concepts pertinent to beam transport line design and ionisation cooling are defined first. These are then followed by a comprehensive description of the ionisation cooling process.

2.1 Phase Space

Each particle in a beam propagating along the z axis can be described by its 6-dimensional phase space vector (x, p_x, y, p_y, t, E), where t represents the time in the laboratory frame of reference, E is the total energy of the particle, x and y are the transverse spatial coordinates, and p_x and p_y are the corresponding momenta. In accelerator physics, it is typical to use the longitudinal position z as the independent variable, and studies can be carried out on the 4D transverse, (x, p_x, y, p_y), and longitudinal, (t, E) or (z, p_z), phase spaces separately. Moreover, studies on the entire 6D phase space can also be conducted.

In beam transport systems, the longitudinal momentum p_z is often approximately conserved and the transverse dynamics may be characterized by the geometric coordinates (x, x', y, y'), also known as trace space, where

$$\begin{aligned} x' &= \frac{dx}{dz} = \frac{p_x}{p_z}, \\ y' &= \frac{dy}{dz} = \frac{p_y}{p_z}, \end{aligned} \tag{2.1}$$

represent the deviation angles of the particle trajectory away from the propagation axis in the horizontal and vertical directions, respectively.

2.2 Liouville's Theorem

A key aspect in the framework of beam dynamics is Liouville's theorem. It states that the particle density in phase space remains constant under the influence of conservative forces, i.e., the ensemble of particles behaves like an incompressible fluid in phase space [23][24].

This statement can be proved by considering a closed system of non-interacting particles in the absence of external forces. Provided a sufficiently large number of particles in the system, a continuous density function $f(x, y, z, p_x, p_y, p_z, t)$ may be defined to model the ensemble in the six dimensional phase space. Using q_i and p_i as the canonical position and momentum variables, a phase space velocity vector may be defined for each particle as $\boldsymbol{v} = (\dot{q}_i, \dot{p}_i)$, where the dot represents derivation with respect to the time variable, and the index i represents the three spatial dimensions

x, y, z. Conservation of the total number of particles in the system implies that the phase space density f must satisfy the continuity equation [25]:

$$\frac{\partial f}{\partial t} + \boldsymbol{\nabla} \cdot (f\boldsymbol{v}) = 0, \tag{2.2}$$

$$\Rightarrow \frac{\partial f}{\partial t} + f\boldsymbol{\nabla} \cdot \boldsymbol{v} + \boldsymbol{v} \cdot \boldsymbol{\nabla} f = 0. \tag{2.3}$$

The term containing the divergence of the velocity vector may be simplified by using the Hamilton's equations for the system

$$\begin{aligned} \dot{q}_i &= \frac{\partial H}{\partial p_i}, \\ \dot{p}_i &= -\frac{\partial H}{\partial q_i}, \end{aligned} \tag{2.4}$$

where H is the Hamiltonian, as follows:

$$\boldsymbol{\nabla} \cdot \boldsymbol{v} = \frac{\partial \dot{q}_i}{\partial q_i} + \frac{\partial \dot{p}_j}{\partial p_j}, \tag{2.5}$$

$$\boldsymbol{\nabla} \cdot \boldsymbol{v} = \frac{\partial^2 H}{\partial q_i \partial p_i} - \frac{\partial^2 H}{\partial p_j \partial q_j} = 0, \tag{2.6}$$

where Einstein summation convention is used. Now the continuity equation reads

$$\frac{\partial f}{\partial t} + \boldsymbol{v} \cdot \boldsymbol{\nabla} f = 0, \tag{2.7}$$

$$\frac{\partial f}{\partial t} + \dot{q}_i \frac{\partial f}{\partial q_i} + \dot{p}_j \frac{\partial f}{\partial p_j} = \frac{df}{dt} = 0, \tag{2.8}$$

which confirms the invariance of the phase space density f.

If the system is subjected to conservative forces, it undergoes canonical transformations that preserve the phase space volume, and hence the density. This property is exploited in beam transport lines, as the forces induced by the magnetic fields are conservative. It also highlights the requirement for the application of non-conservative (dissipative) forces in scenarios where the phase space density must be increased, such as muon beam cooling.

2.3 Linear Beam Dynamics

A linear beam transport system consists of a series of bending and focusing magnets, which guide charged particles along a reference trajectory, or keep them close by. Rather than following the reference trajectory precisely, the particles experience restoring forces along the magnetic lattice and oscillate about this trajectory. Each element of the magnetic lattice is characterised by a magnet focusing strength parameter $\kappa_u(z)$, where $u = x, y$. In the first order approximation, the charged particle motion in the transverse phase space follows Hill's equations of motion [26]:

$$\frac{d^2u}{dz^2} + \kappa_u(z)u = 0. \tag{2.9}$$

2.3.1 Transfer Matrix Approach

The focusing strength parameter is dependent on the configuration of the magnetic lattice and is therefore an arbitrary function of the independent variable z. As such, the differential equation 2.9 does not have a general solution. However, by splitting the beam transport line into segments in which the focusing strength is constant, one can analytically compute the particle trajectory through the entire system. In this approximation, known as the hard edge model, within elements of $\kappa(z) = \kappa = \text{const.}$, the differential equations admit trivial solutions describing harmonic oscillator motion:

$$u(z) = u_0 C(z) + u_0' S(z), \tag{2.10}$$

where u_0 and u_0' are arbitrary initial conditions for the position and the angle of the particle, and the C and S functions are defined by

$$C(z) = \cos(\sqrt{\kappa}z) \quad \text{and} \quad S(z) = \frac{1}{\sqrt{\kappa}}\sin(\sqrt{\kappa}z) \quad \text{if } \kappa > 0, \tag{2.11}$$

$$C(z) = \cosh(\sqrt{|\kappa|}z) \quad \text{and} \quad S(z) = \frac{1}{\sqrt{|\kappa|}}\sinh(\sqrt{|\kappa|}z) \quad \text{if } \kappa < 0, \tag{2.12}$$

$$C(z) = 1 \quad \text{and} \quad S(z) = z \quad \text{if } \kappa = 0. \tag{2.13}$$

By taking the derivative of equation 2.10 with respect to the longitudinal position z, one obtains the solution describing the angle evolution:

$$u'(z) = u_0 C'(z) + u'_0 S'(z). \tag{2.14}$$

Equations 2.10 and 2.14 fully describe the motion in the transverse plane and can be expressed in matrix form

$$\begin{pmatrix} u(z) \\ u'(z) \end{pmatrix} = \underbrace{\begin{pmatrix} C(z) & S(z) \\ C'(z) & S'(z) \end{pmatrix}}_{\boldsymbol{M}(z)} \begin{pmatrix} u_0 \\ u'_0 \end{pmatrix}. \tag{2.15}$$

In the hard edge approximation, where the focusing strength is constant within each lattice element and evolves as a step function at the boundary between any two adjacent elements, one can obtain such a matrix transformation for each beam line element. This framework allows one to follow the particle trajectory through the whole beam transport system using a series of matrix multiplications. The individual element transfer matrix, $\mathbf{M}$, takes specific form depending on the element type, i.e., drift, dipole, quadrupole, and is orthogonal, with $|\mathbf{M}| = 1$. This property is an alternative formulation of the Liouville's theorem.

2.3.2 Analytical Approach

A deeper insight about particle trajectories can be achieved by attempting to solve equation 2.9 for an arbitrary $\kappa(z)$, using a trial, pseudo-harmonic oscillator solution with an z-dependent amplitude and phase [26],

$$u(z) = \sqrt{\epsilon}\sqrt{\beta(z)}\cos(\psi(z) - \psi_0), \tag{2.16}$$

where ϵ and ψ_0 are integration constants. Substituting this solution back into Hill's equation and choosing the normalisation $\beta(z)\psi'(z) = 1$ yields:

$$2\beta\beta'' - \beta'^2 + 4(\beta^2\kappa - 1) = 0, \tag{2.17}$$

where the explicit z dependence has been dropped for brevity. This differential equation models the lattice-dependent component of the oscillation amplitude, $\beta(z)$, known as the betatron function. One can gain more physical insight by using the

solution 2.16 and its derivative to obtain the so-called Courant-Snyder invariant [27],

$$\gamma(z)u^2 + 2\alpha(z)uu' + \beta(z)u'^2 = \epsilon, \tag{2.18}$$

where the parameters α and γ are given by

$$\begin{aligned} \alpha(z) &= -\frac{\beta'(z)}{2}, \\ \gamma(z) &= \frac{1+\alpha^2(z)}{\beta(z)}. \end{aligned} \tag{2.19}$$

This choice of parametrisation becomes apparent by noting that the expression 2.18 represents the equation of an ellipse with area $\pi\epsilon$, i.e., in trace space, the particle evolves along an elliptical contour with shape and orientation dictated by α, β and γ, which are known as the Twiss parameters. The constant of motion ϵ is called the single particle emittance, also known as amplitude. The Twiss parameters are z-dependent and the ellipse changes shape and orientation continually. However, as the single particle emittance is conserved, a particle that starts on the ellipse will remain on it. The elliptical trajectory in trace space, with its dimensions expressed as functions of the Twiss parameters, is depicted in figure 2.1.

2.4 Collective Motion

While the solution to the linear equations of motion allows one to compute a charged particle's trajectory through an arbitrary arrangement of magnets, repeating the procedure for an entire ensemble of particles becomes impractical. As such, a depiction of the entire particle beam must be considered. To study the collective motion of a beam, one can observe the dynamics of its constituent particles in phase space.

2.4.1 Beam Covariance Matrix

An ensemble of particles can be described by a probability density function in the 6D phase space. This allows for a quantitative description through first and second moments. In the 4D transverse trace space, the particle displacement and angle are usually defined relative to the reference trajectory that passes through the centre of the magnets. Consequently, the first moments are generally zero. Thus the second

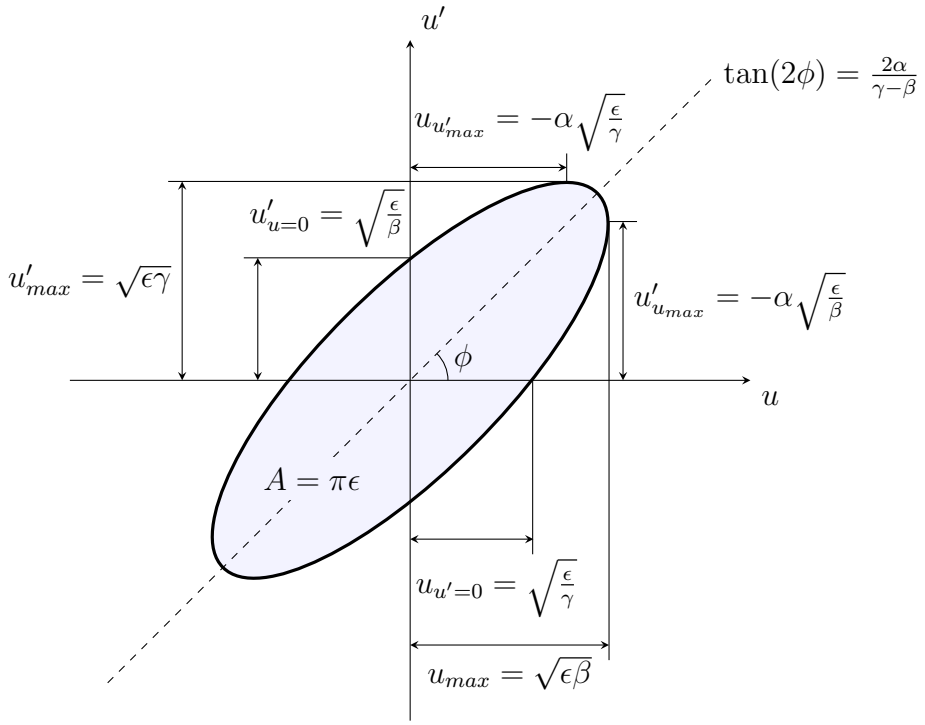

Figure 2.1: Diagram of the elliptical single particle trajectory in the 2D trace space. The dimensions are expressed in terms of the Twiss parameters α, β, γ and single particle emittance ϵ.

moments, which are provided by the covariance matrix, are typically used to define the trace space density of the beam.

The beam probability density function can be modelled as a Gaussian distribution. Using this approximation in 2D, the trace space probability distribution for a beam centred at $(0, 0)$ is given by [28]

$$f(\mathbf{u}) = \frac{1}{2\pi\sqrt{|\mathbf{\Sigma}_u|}} \exp\left[-\frac{1}{2}\mathbf{u}^T\mathbf{\Sigma}_u^{-1}\mathbf{u}\right], \tag{2.20}$$

where $\mathbf{u} = (u, u')$ and the covariance matrix $\mathbf{\Sigma}_u$ is defined as

$$\mathbf{\Sigma}_u = \begin{pmatrix} \sigma_{uu} & \sigma_{uu'} \\ \sigma_{u'u} & \sigma_{u'u'} \end{pmatrix}, \tag{2.21}$$

with σ_{ii} the variance of coordinate i and σ_{ij} the covariance of coordinates i and j. One can notice that $\mathbf{u}^T\mathbf{\Sigma}_u^{-1}\mathbf{u} = 1$ describes an elliptical contour in trace space along which the density is constant, known as the Root Mean Square (RMS) beam ellipse.

All the particles enclosed by the RMS ellipse evolve on individual elliptical trajectories, which remain elliptical and with constant area under linear transformations. As a consequence, these particles will remain within the RMS ellipse, rendering it as a useful description of the collective behaviour of the beam.

The Twiss parametrisation used in equation 2.18 can also be employed for the RMS ellipse equation

$$\mathbf{u}^T \boldsymbol{\Sigma}_u^{-1} \mathbf{u} = \epsilon^{-1}(\gamma u^2 + 2\alpha u u' + \beta u'^2) = 1, \tag{2.22}$$

where α, β, γ and ϵ are now parameters describing the shape, orientation and size of the beam in the 2D trace space. The $\epsilon = \sqrt{|\boldsymbol{\Sigma}_u|}$ is the beam RMS geometric emittance, directly proportional to the area of the ellipse, and the beam Twiss parameters can be expressed in terms of the covariance matrix elements as follows:

$$\begin{aligned} \alpha &= -\frac{\sigma_{uu'}}{\epsilon} \\ \beta &= \frac{\sigma_{uu}}{\epsilon} \\ \gamma &= \frac{\sigma_{u'u'}}{\epsilon} \end{aligned} \quad . \tag{2.23}$$

The covariance matrix can also be represented using the Twiss parameters as

$$\boldsymbol{\Sigma}_u = \epsilon \begin{pmatrix} \beta & -\alpha \\ -\alpha & \gamma \end{pmatrix}. \tag{2.24}$$

The betatron function, β, is a frequently used quantity in accelerator physics as it defines the width of the beam for a given emittance, hence providing information about the focusing state of the beam. α describes the tilt of the beam ellipse, while γ gives a measure of the beam divergence.

In this framework, the beam evolution along the transport line is captured by the evolution of the beam covariance matrix. In the linear optics regime, the covariance matrix transforms as

$$\boldsymbol{\Sigma}_u^{\text{fin}} = \mathbf{M} \boldsymbol{\Sigma}_u^{\text{in}} \mathbf{M}^{\boldsymbol{T}}, \tag{2.25}$$

where $\mathbf{M}$ is the transfer matrix defined by beam line configuration between the initial and final positions considered.

2.4.2 Beam Emittance

The emittance is a measure of the volume occupied by the beam in phase (or trace) space. It is a key quantity in accelerator physics as it provides a measure of both spatial and dynamical extent of the beam and it is a constant of the motion under linear beam optics.

Three two-dimensional emittances are commonly defined, i.e., one for each coordinate. When the coupling between the motion in each plane is very weak, the dynamics can be treated independently. In 2D, the geometric emittance corresponds to the area occupied by the central 39% of the particles in the beam and it is calculated from the determinant of the 2×2 covariance matrix $\mathbf{\Sigma}$,

$$\epsilon = \sqrt{|\mathbf{\Sigma}|}. \tag{2.26}$$

However, if the coupling between the dynamics in different planes becomes significant, as in the case of the solenoid magnetic channel in MICE, it is useful to consider the dynamics in the 4D transverse phase space or the 6D phase space. For this purpose, equation 2.26 can be generalised to multiple dimensions as follows:

$$\epsilon_{nD} = |\mathbf{\Sigma}_{nD}|^{\frac{1}{n}}, \tag{2.27}$$

where n is the number of dimensions and $\mathbf{\Sigma}_{nD}$ is the $n \times n$ covariance matrix. The n-dimensional emittance is directly proportional to the volume of the RMS hyperellipsoid, which is defined as

$$V_{nD} = \frac{\pi^{\frac{n}{2}}}{\Gamma(1+\frac{n}{2})}\sqrt{|\mathbf{\Sigma}_{nD}|}, \tag{2.28}$$

where Γ is the gamma function. Using equation 2.27, the relationship between the two quantities reads

$$V_{nD} = \frac{\pi^{\frac{n}{2}}}{\Gamma(1+\frac{n}{2})}(\epsilon_{nD})^{\frac{n}{2}}. \tag{2.29}$$

So far in the discussion about emittance, the trace space variables (x, x', y, y') were used to describe the motion in the transverse plane. The angles x' and y' are functions of longitudinal momentum and are sensitive to changes in the beam energy, which typically occur via accelerating or dissipative forces. As a result, the

emittance defined on the trace space, commonly referred to as geometric emittance, is not conserved under beam energy changes. To avoid this issue, the normalised RMS emittance is typically used,

$$\epsilon_N = \beta_{\text{rel}}\gamma_{\text{rel}}|\mathbf{\Sigma}_{nD}|^{\frac{1}{n}}, \tag{2.30}$$

where β_{rel}, γ_{rel} are the relativistic factors. The normalised emittance is invariant under beam energy changes.

2.4.3 Transverse Phase Space Dynamics in a Solenoid

Generally, beam transport lines are designed such that there is weak or no coupling in the transverse plane between the x and y dynamics. In such instances, the evolution of the phase space can be modelled and analysed independently in x and y. However, when solenoid magnets are used, a $x-y$ coupling is generated through the axial magnetic field, which causes the particle to evolve in a helical trajectory. Hence, a treatment of the 4-dimensional transverse phase space is required. A further significant coupling to the longitudinal motion would require the consideration of the full 6D phase space.

In MICE, the transverse and longitudinal phase spaces are decoupled to first order, and the corresponding emittances are studied independently. The focus of the work in this thesis is on the beam evolution in the 4D transverse phase space (x, p_x, y, p_y), with emphasis on the normalised RMS emittance. The 4D covariance matrix is defined as

$$\mathbf{\Sigma}_{\perp} = \begin{pmatrix} \sigma_{xx} & \sigma_{xp_x} & \sigma_{xy} & \sigma_{xp_y} \\ \sigma_{p_xx} & \sigma_{p_xp_x} & \sigma_{p_xy} & \sigma_{p_xp_y} \\ \sigma_{yx} & \sigma_{yp_x} & \sigma_{yy} & \sigma_{yp_y} \\ \sigma_{p_yx} & \sigma_{p_yp_x} & \sigma_{p_yy} & \sigma_{p_yp_y} \end{pmatrix}, \tag{2.31}$$

and the transverse normalised RMS beam emittance is calculated from it as

$$\epsilon_{\perp} = \frac{1}{mc}|\mathbf{\Sigma}_{\perp}|^{\frac{1}{4}}. \tag{2.32}$$

If the beam is measured particle-by-particle, the phase space distribution can be reconstructed and the covariance matrix can be computed. Assuming a cylindrically

symmetric Gaussian beam, the transverse covariance matrix can be also expressed as [29][30]

$$\mathbf{\Sigma}_\perp = mc\epsilon_\perp \begin{pmatrix} \beta_\perp/\langle p_z\rangle & -\alpha_\perp & 0 & -(\beta_\perp\kappa - \mathcal{L}) \\ -\alpha_\perp & \gamma_\perp\langle p_z\rangle & (\beta_\perp\kappa - \mathcal{L}) & 0 \\ 0 & (\beta_\perp\kappa - \mathcal{L}) & \beta_\perp/\langle p_z\rangle & -\alpha_\perp \\ -(\beta_\perp\kappa - \mathcal{L}) & 0 & -\alpha_\perp & \gamma_\perp\langle p_z\rangle \end{pmatrix}, \tag{2.33}$$

where $\alpha_\perp$, $\beta_\perp$ and $\gamma_\perp$ are the 4D Twiss parameters, $\mathcal{L} = \langle L_{canon}\rangle/2mc\epsilon_\perp$ is the mean canonical angular momentum normalised to the beam emittance, $\langle p_z\rangle$ is the mean longitudinal momentum, and $\kappa = qB_z/2\langle p_z\rangle$ is a measure of the focusing strength of the solenoid, with q denoting the charge of the particle.

Using equation 2.33 in the definition of emittance as expressed by the equation 2.32, the relationship between the transverse Twiss parameters reads

$$\gamma_\perp = \frac{1 + \alpha_\perp^2 + (\beta_\perp\kappa - \mathcal{L})^2}{\beta_\perp}. \tag{2.34}$$

The evolution of the Twiss parameters is described by

$$\beta_\perp' = -2\alpha_\perp \tag{2.35}$$

and

$$2\beta_\perp\beta_\perp'' - \beta_\perp'^2 + 4(\beta_\perp^2\kappa^2 - 1 - \mathcal{L}^2) = 0, \tag{2.36}$$

with $\epsilon_\perp$ and $\mathcal{L}$ as constants of the motion. The beam focusing can be tuned through changing the solenoid magnetic field. The last term of the equation shows that if the beam has non-zero canonical angular momentum, it becomes more difficult to focus. The parameters can be calculated from the reconstructed second order moments as

$$\begin{aligned} \alpha_\perp &= -\frac{\langle xp_x\rangle + \langle yp_y\rangle}{2mc\epsilon_\perp} \\ \beta_\perp &= \frac{\langle x^2\rangle + \langle y^2\rangle}{2mc\epsilon_\perp}\langle p_z\rangle \\ \gamma_\perp &= \frac{\langle p_x^2\rangle + \langle p_y^2\rangle}{2mc\epsilon_\perp\langle p_z\rangle} \end{aligned} \quad . \tag{2.37}$$

It is instructive to compare the 4D transverse covariance matrix shown in equa-

tion 2.33 with its 2D equivalent defined in equation 2.24. One can observe that there are additional off-diagonal terms, resulting from the mean kinetic angular momentum, $\langle L_{kin} \rangle = \langle xp_y - yp_x \rangle = -2mc\epsilon_\perp(\beta_\perp \kappa - \mathcal{L})$, which reinforces the need to fully analyse the 4D phase space.

2.4.4 Canonical Angular Momentum in a Solenoid

Generally, in a system with cylindrical symmetry, such as in the case of a uniform solenoidal field, the canonical angular momentum, i.e., the generator of rotation about the axis of symmetry, is a constant of the motion. The canonical angular momentum along the z axis is defined as

$$L_{canon} = xp_y^c - yp_x^c, \tag{2.38}$$

where the c superscript denotes the canonical momentum variables. The canonical momenta are related to the kinetic momenta via

$$\mathbf{p}^c = \mathbf{p} + q\mathbf{A}, \tag{2.39}$$

where $\mathbf{A}$ is the magnetic vector potential. Using this relation, one can express equation 2.38 in terms of the kinetic momenta as follows:

$$L_{canon} = xp_y - yp_x + qrA_\phi, \tag{2.40}$$

where A_ϕ is the azimuthal component of the vector potential and $r = \sqrt{x^2 + y^2}$ is the radius of the particle. The vector potential for the solenoid field is given by

$$A_\phi = \frac{r}{2}B_z - \frac{r^3}{16}B_z'' + \mathcal{O}(r^5), \tag{2.41}$$

where $B_z = B_z(r = 0, z)$. Then in the linear approximation, the average canonical angular momentum for an ensemble of particles can be expressed as

$$\langle L_{canon} \rangle \simeq \langle xp_y \rangle - \langle yp_x \rangle + \frac{qB_z}{2}\langle r^2 \rangle, \tag{2.42}$$

where $\langle xp_y \rangle - \langle yp_x \rangle$ is the mean kinetic angular momentum $\langle L_{kin} \rangle$. A beam with no kinetic angular momentum in free space, and hence no canonical angular momentum, gains kinetic angular momentum upon entrance in a solenoidal field. The gain is

equal to $-\frac{qB_z}{2}\langle r^2 \rangle$ to preserve the canonical angular momentum.

In a cooling cell, the beam interaction with an absorber material leads to a net decrease in the mean magnitude of the beam kinetic angular momentum. As a result, the average canonical angular momentum can change, depending on the sign of the magnetic field in the region of the interaction. For a cooling channel composed of a series of cooling cells, the effect described above could result in a build-up of canonical angular momentum, which is detrimental to cooling [29]. For example, the build-up would make the beam increasingly harder to focus. As will be discussed in section 2.7, maximising the cooling performance requires a low betatron function at the absorber, hence strong beam focusing.

Proposed solutions to maintain a relatively constant and close to zero canonical angular momentum throughout the cooling section are based on flipping the solenoid field polarity such that any build-up generated before the the field flip location be cancelled out after it [31][32]. One such solution consists in placing the absorber at the location of the field polarity flip [33]. The MICE cooling cell was designed to operate in such a configuration.

2.5 Beam Matching

In general, beam matching refers to the process whereby the focusing strength of individual magnets in the lattice is tuned such that specific beam optics parameter values are achieved at locations of interest. In the case of injection into a storage ring or circular collider, the beam is required to be matched to the Twiss functions of the periodic lattice at the injection point. For linear accelerators and transfer lines, periodic or symmetric sections within the lattice may also require adequate matching.

This is the case in MICE, where the cooling cell is symmetric about the absorber module and was designed as a periodic component in a Neutrino Factory cooling stage. For this purpose, it is desired that the Twiss parameters have the same values at the beginning and the end of the cell. Optimal transmission and focusing at the absorber require that $\beta'_\perp = 0$ and $\beta''_\perp = 0$ in the region of uniform field within the spectrometers. The MICE transfer line was tasked to deliver beams satisfying the aforementioned matching conditions and having a $\beta_\perp$ value determined by the focusing strength of the upstream solenoid spectrometer (using equation 2.36), at

the entrance to the cooling channel.

An improperly matched beam undergoes oscillations of the betatron function and beam width. In such instances, the tails of the distribution may be subjected to non-linear dynamics, which introduces a correlation between the single particle emittance and the betatron frequency of the particles. As a result, the distribution tails evolve differently from the core in a phenomenon known as beam filamentation [34][35]. While Liouville's theorem still holds during filamentation, the volume of the hyper-ellipsoid enclosing the beam phase space can increase, which is then observed as an emittance growth [36][37].

2.6 Non-linear Emittance Growth

In general, emittance growth via beam filamentation occurs when some of the particles in the beam are exposed to non-linear effects. Apart from being caused by a beam mismatch, filamentation can also occur when the beam has a large initial emittance, or a large momentum spread. An elegant framework that provides insight into the non-linear dynamics in a solenoid has been developed by Dragt [38][39], which is briefly summarised in this section.

The Hamiltonian for the relativistic motion of a particle with mass m, charge q and canonical phase space vector $\mathbf{u}^c = (x, p_x^c, y, p_y^c, t, p_t^c)$ in a solenoidal magnetic field can be expressed as

$$H(\mathbf{u}^c; z) = -\sqrt{(p_t^c/c)^2 - m^2c^2 - (p_x^c - qA_x)^2 - (p_y^c - qA_y)^2}\,, \tag{2.43}$$

where p_t^c is the momentum conjugate to the time, (A_x, A_y) are the transverse components of the vector potential, and z is the independent variable (instead of the time t). The Hamiltonian is then transformed to a set of variables that represent the particle's deviation from the reference trajectory, and the vector potential components are expanded in terms of the on-axis longitudinal magnetic field $B_z(z, r = 0)$ and its derivatives with respect to z. The detailed mathematical procedure is developed in [38]. Finally, the Hamiltonian is expanded as a power series,

$$H = \sum_{n=0}^{\infty} H_n\,, \tag{2.44}$$

where H_n are homogeneous polynomials of order n in the deviation variables.

The terms H_0 and H_1 are constants and do not contribute to the dynamics. The H_2 term recovers the linear dynamics, while all terms with $n \geq 3$ are non-linear. The first non-linear term, H_3, is purely chromatic, i.e., proportional to the deviation from the reference total momentum. Hence, a beam with a significant momentum spread may experience emittance growth predominantly due to chromatic aberrations. Higher order terms become increasingly complex. The terms included in H_4 can be classified into three groups: those that are independent of B_z, those proportional to B_z and those proportional to the field curvature, $\partial^2 B_z/\partial z^2$. Thus, the corresponding non-linear effects may be more prominent in regions where the field gradient changes sharply or swaps sign.

2.7 Ionisation Cooling

Ionisation cooling is a novel technique purposed to reduce the emittance of muon beams. It uses dissipative forces from matter interactions to circumvent Liouville's theorem and compress the muon beam phase space to levels required by the accelerating systems of a Neutrino Factory or Muon Collider, before significant decay occurs. The concept has been proposed by Skrinskii and Parkhomchuk [19] and then developed by Neuffer [20].

In ionisation cooling, a muon beam passes through a volume of material, known as the absorber, and loses both transverse and longitudinal momentum by ionising atoms, releasing electrons. The longitudinal momentum can be restored using RF cavities. Simultaneously, multiple Coulomb scattering in the atomic nuclei increases the angular spread of the beam, thus inflicting the opposite effect of heating the beam. This process is schematically described in figure 2.2. The overall effect of the two competing processes is captured by the "cooling equation", which describes the rate of change of beam transverse normalised RMS emittance upon passage through an absorber.

In this section, the 4D transverse geometric emittance is denoted by ϵ, while $\epsilon_\perp$ is used for the 4D transverse normalised emittance. Starting from the general definition of geometric emittance in equation 2.27, the transverse geometric emittance of a cylindrically symmetric beam in a solenoidal channel can be expressed as

$$\epsilon^2 = \langle x^2 \rangle \langle \theta_x^2 \rangle - \langle x\theta_x \rangle^2 - \langle x\theta_y \rangle^2, \tag{2.45}$$

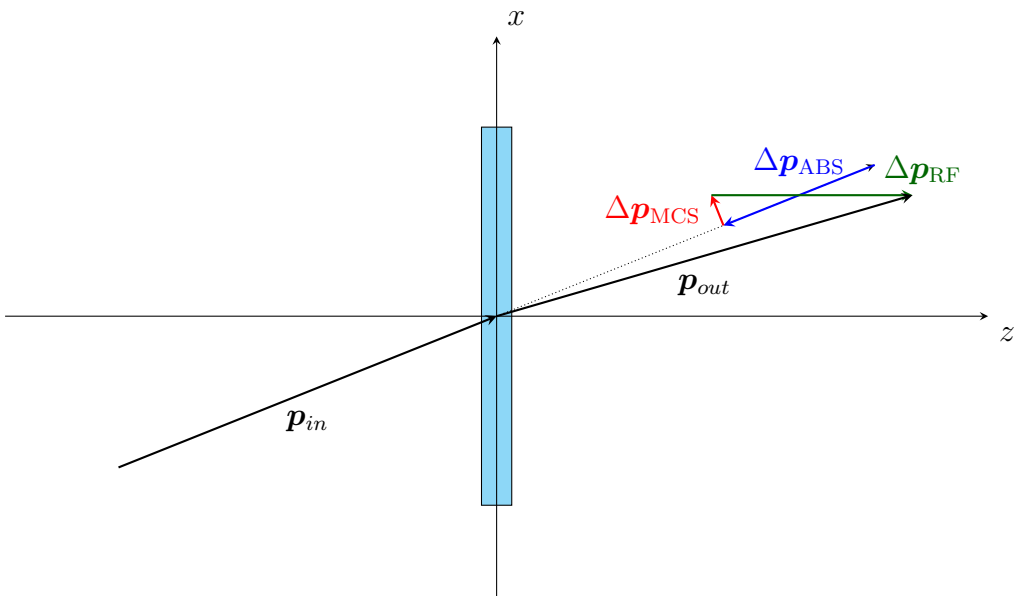

Figure 2.2: Schematic depiction of the ionisation cooling process. The incident momentum is $\mathbf{p}_{\mathrm{in}}$. At the absorber, $\mathbf{p}_{\mathbf{ABS}}$ is the momentum lost via ionisation and $\mathbf{p}_{\mathrm{MCS}}$ the increase in angular divergence due to multiple Coulomb scattering. $\mathbf{p}_{\mathrm{RF}}$ is the longitudinal momentum gain induced by an RF cavity, and $\mathbf{p}_{\mathrm{out}}$ is the resulting outgoing momentum.

where $\theta_x = x' = dx/dz$ is the angular divergence of a particle from the z axis in the x direction, and θ_y is the equivalent in y. However, the normalised transverse emittance is the quantity of interest, as it remains invariant under energy changes. Rewritting equation 2.30 in a simpler form, its relation to the geometric emittance is given by

$$\epsilon_{\perp} = \beta_{\mathrm{rel}}\gamma_{\mathrm{rel}}\epsilon, \tag{2.46}$$

where β_{rel} and γ_{rel} are the relativistic factors.

By taking the derivative with respect to z, a first expression for the rate of change of normalised transverse emittance as the beam passes through material is obtained, i.e.,

$$\frac{d\epsilon_{\perp}}{dz} = \frac{d(\beta\gamma)}{dz}\epsilon + \beta\gamma\frac{d\epsilon}{dz}. \tag{2.47}$$

The first term describes the effect due to the energy loss via ionisation, which is the generator of cooling, i.e.,

$$\left.\frac{d\epsilon_\perp}{dz}\right|_{\text{cooling}} = -\frac{\epsilon_\perp}{\beta\gamma}\frac{d(\beta\gamma)}{dE}\left|\frac{dE}{dz}\right| = -\frac{\epsilon_\perp}{\beta^2 E}\left|\frac{dE}{dz}\right|, \tag{2.48}$$

where $-|dE/dz|$ is the mean rate of beam energy loss per unit length of absorber. The negative sign implies emittance is being reduced, reaffirming that this term is responsible for cooling.

The second term of equation 2.47 describes the heating effect caused by multiple Coulomb scattering. It can be expanded by differentiating equation 2.45 with respect to z as

$$\begin{aligned}\left.\frac{d\epsilon_\perp}{dz}\right|_{\text{heating}} = \frac{\beta\gamma}{2\epsilon}\Bigg(&\langle\theta_x^2\rangle\frac{d\langle x^2\rangle}{dz} + \langle x^2\rangle\frac{d\langle\theta_x^2\rangle}{dz} \\ &-2\langle x\theta_x\rangle\frac{d\langle x\theta_x\rangle}{dz} - 2\langle x\theta_y\rangle\frac{d\langle x\theta_y\rangle}{dz}\Bigg).\end{aligned} \tag{2.49}$$

If the absorber is situated at a beam waist, i.e., $\alpha_\perp = 0$, the correlation term $\langle x\theta_x\rangle$ becomes negligible. Furthermore, it is argued that in the presence of a strong magnetic field in the absorber region the correlations between the transverse position and the angular divergence remain constant, hence the last two terms are approximately zero [40][41]. The same strong magnetic field prevents the beam from expanding, rendering the first term insignificant. Taking these approximations into account, equation 2.49 is reduced to

$$\left.\frac{d\epsilon_\perp}{dz}\right|_{\text{heating}} \simeq \frac{\beta\gamma}{2\epsilon}\langle x^2\rangle\frac{d\langle\theta_x^2\rangle}{dz} = \frac{\beta\gamma\beta_\perp}{2}\frac{d\langle\theta_x^2\rangle}{dz}, \tag{2.50}$$

where $\beta_\perp = \langle x^2\rangle/\epsilon$ is the betatron function at the absorber. The width of the scattering distribution is approximated by applying a Gaussian fit to the model developed by Molière [42][43]. In this approximation, the rate of change of the mean square scattering angle is given by

$$\frac{d\langle\theta_x^2\rangle}{dz} \simeq \frac{1}{X_0}\left(\frac{13.6\,\text{MeV/c}}{p\beta}\right)^2, \tag{2.51}$$

with X_0 the radiation length of the absorber material and p the total momentum of the beam.

Combining the cooling and heating terms yields the rate of change of normalised

transverse RMS emittance as

$$\frac{d\epsilon_\perp}{dz} \simeq -\frac{\epsilon_\perp}{\beta^2 E}\left|\frac{dE}{dz}\right| + \frac{\beta_\perp (13.6\,\mathrm{MeV/c})^2}{2\beta^3 E m X_0}, \tag{2.52}$$

also known as the cooling equation.

By examining the equation, it is observed that the process is influenced by properties that pertain to the beam and the absorber material. The cooling effect is stronger for slower beams with large emittance. Furthermore, the heating due to multiple Coulomb scattering is weaker for beams with low betatron function at the absorber. This feature can be achieved by using superconducting solenoids that provide strong symmetrical focusing in the transverse plane. The absorber material affects both terms in the equation, i.e., cooling through the rate of energy loss and heating through the radiation length. Optimal overall cooling is achieved by using low-Z materials for which the $X_0 \left|\frac{dE}{dz}\right|$ product is maximised. Liquid hydrogen and lithium hydride were the materials of choice in MICE.

When the two antagonist terms in the equation cancel out and the rate is zero, equilibrium emittance is reached, i.e.,

$$\epsilon_\perp^{eqm} = \frac{\beta_\perp (13.6\,\mathrm{MeV/c})^2}{2\beta m X_0}\left|\frac{dE}{dz}\right|^{-1}. \tag{2.53}$$

Beams with emittances lower than the equilibrium emittance experience heating.

Chapter 3

The Muon Ionisation Cooling Experiment

High brightness muon beams are required for the development of a Muon Collider [44] and can significantly enhance the performance of a Neutrino Factory [8]. In the proton driver scheme, muons are produced through the decay of pions from the interaction of protons with a target. The resulting muon beam has a large phase space volume (emittance), which makes it challenging to accelerate and store. Thus, maximising the muon yield while maintaining a suitably small aperture in the accelerator system requires that the emittance of the muon beam be reduced (cooled). The short muon lifetime ($\tau_\mu \sim 2.2\,\mu s$) renders conventional cooling techniques unsuitable, leaving ionisation cooling as the technique proposed for future muon facilities [19][20].

The Muon Ionisation Cooling Experiment (MICE) was designed to demonstrate the feasibility of ionisation cooling and to provide the first measurement of normalised transverse emittance reduction in a muon beam. MICE has reported on the first realisation of muon cooling by observing an increase in the number of low-amplitude muons after passage of the beam through an absorber material, as well as an increase in phase space density [22].

3.1 Introduction

The MICE collaboration is an international enterprise with the core aims to design, build and operate a cooling channel able to achieve the desired performance for a Neutrino Factory, and to further test its performance by exposing it to a multitude of beam conditions and modes of operation [45]. The cooling channel section was designed to produce a reduction in transverse emittance of up to 10%, with a resolution of 0.1% on the measurement of absolute emittance, while maintaining the flexibility to investigate a variety of input beam momenta (140 - 240 MeV/c), optics and absorber materials.

Since its proposal, MICE has been subject to a number of comprehensively considered re-designs [46]. This work is based on the final configuration in which the experiment operated, known as MICE Step IV. The data collection concluded in December 2017 and the experimental apparatus was decommissioned in 2018.

The performance of an ionisation cooling cell depends on the properties of the incoming beam, as well as the properties of the absorber material. The Step IV cooling channel was set up to perform detailed studies on material physics and the reduction of normalized transverse emittance using lithium hydride and liquid hydrogen absorbers, without re-acceleration of the beam [47]. Achieving the proposed measurement precision required a broad and robust detector system, designed to perform single-particle detection. In MICE, each muon trajectory and momentum were individually measured before and after passing through the absorber material by scintillating fibre trackers. Particle identification (PID) detectors were used upstream and downstream of the cooling cell to identify impurities within the beam and perform event selection. The components of the MICE experiment in the Step IV configuration are described in detail in this chapter.

3.2 Muon Beam Line

MICE operated as a parasitic experiment on the ISIS proton synchrotron at the Rutherford Appleton Laboratory (RAL), in the United Kingdom. The MICE muon beam line was designed to produce and transport muons with momenta in the 140 - 240 MeV/c range to the MICE cooling channel. The detailed structure and components of the beam line can be seen in figure 3.1.

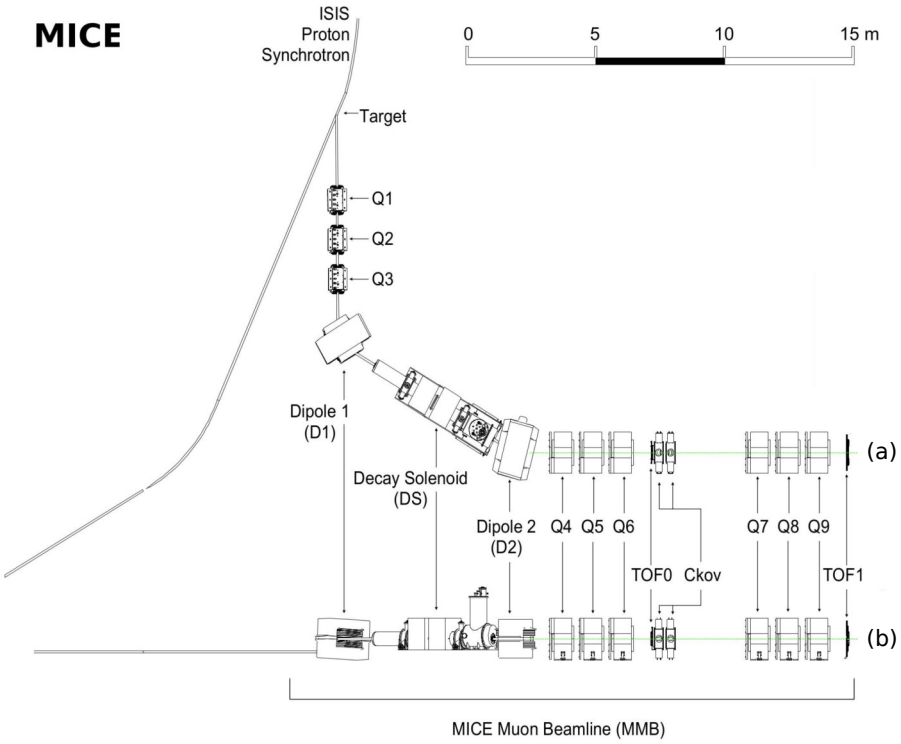

Figure 3.1: (a) Top and (b) side views of the MICE beam line with its instrumentation. The quadrupole magnets are denoted by Q1-9. The two Ckovs are Cherenkov detectors and the TOFs are time-of-flight hodoscopes.

The ISIS synchrotron accelerates proton bunches to 800 MeV over a period of 10 ms, at a rate of 50 Hz [48]. The MICE target – a titanium hollow cylinder – was dipped into the halo of the ISIS proton beam in the last 1-2 ms of the acceleration phase when protons were near the maximum energy, at a rate of $\sim$ 1 Hz [49]. To meet the muon flux demands and cause minimal disruption to the ISIS beam, precise position and timing control of the target was achieved through the use of a linear electromagnetic drive able to provide an acceleration of up to 780 ms^{-2}. During data collection, the low rate of muons delivered to the cooling channel ($\sim$ 50 μ/s) ensured the particle identification and reconstruction procedures could be applied individually.

The resulting pions were captured by a triplet of conventional quadrupoles (Q1-3) and transported to the dipole D1, which steered pions of specific momenta into the decay solenoid (DS). The strong solenoid focusing provided by a 5 T field, combined with the extended path length of the spiralling pions increased the number of muons

captured within the decay solenoid. The proton contamination left in the beam at the exit from the DS was removed by using a polyethylene absorber of variable thickness [50]. The resulting beam was subjected to another momentum selection and pointed towards the cooling channel by a second dipole magnet D2. The D1 and D2 dipoles were set up to select positively charged pions, as these were produced at a rate approximately three times larger than that of negatively charged pions. A further pair of quadrupole triplets (Q4-6 and Q7-9) delivered the beam that had emerged from D2 to the cooling channel.

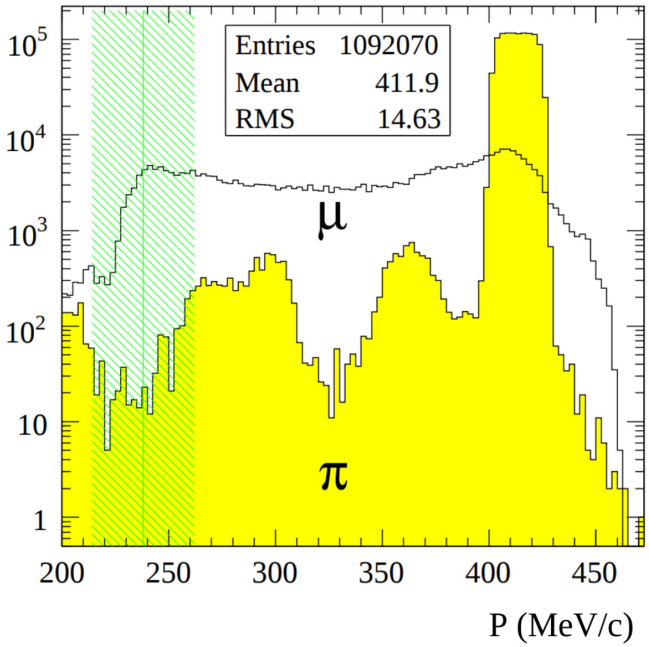

Figure 3.2: Simulation of (yellow fill) pion and (black line) muon total momentum distributions at the exit of decay solenoid for a 400 MeV/c pion selection at D1. The green band shows the momentum window selected at D2, in the 'muonic' mode configuration [51].

Owing to the pion decay kinematics within the DS, the two bending magnets D1 and D2 were employed to determine the momentum spectrum and particle species content of the beam delivered to the experiment. Two working modes were established, known as the 'muonic' and 'calibration' modes. In the 'muonic' mode, D2 was set to select a momentum bite centred at a value approximately half of the D1 momentum. In this setting, the backward-going muons in the pion rest frame were selected and most of the pions were removed, leading to a high purity muon beam

[51]. This can be seen in figure 3.2, which shows a simulation of total momentum distributions of muons and pions in the beam at the exit of the decay solenoid, for a D1 pion selection momentum of 400 MeV/c. The region close to the backward-going muon peak is heavily depleted of pions. A dedicated study measured the pion contamination in the 'muonic' beam to be less than 1.4% [52].

In the 'calibration' mode, the selection momenta at D1 and D2 were the same. This allowed the majority of the pions that had not decayed in the DS to be transported downstream towards the cooling channel. This configuration delivered beams composed of electrons, muons and pions at higher rates than the 'muonic' mode, and was used for calibration of detectors.

3.3 Cooling Channel

The MICE cooling channel was the main component of the experiment. A diagram of the channel layout in the Step IV configuration can be seen in figure 3.3. It was composed of the cooling cell, an Absorber Focus Coil module (AFC), flanked by an Upstream Spectrometer Solenoid and a Downstream Spectrometer Solenoid[1]. Twelve superconducting solenoid magnets – five in each spectrometer and two in the AFC – were used to contain and focus the beam throughout the channel. Each spectrometer solenoid accommodated a scintillating fibre tracker, used to measure the muon beam phase space before and after it passed through the cooling cell.

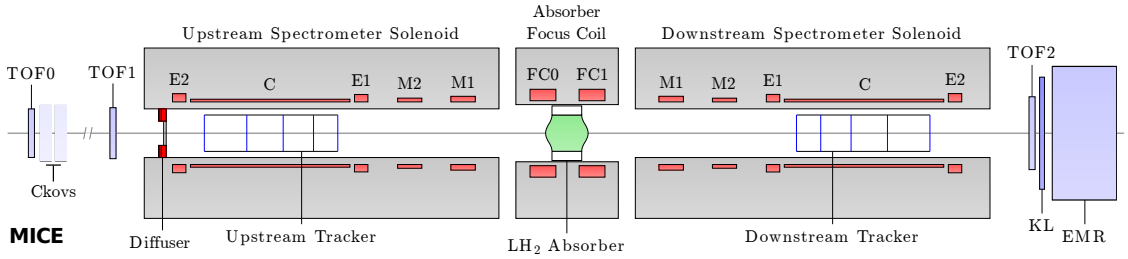

Figure 3.3: Schematic diagram of the MICE Step IV cooling channel. The upstream and downstream PID detector systems are also shown. Figure adapted from [22].

[1]In more accurate terms, the cooling channel was composed of the AFC only. It is the structure designed to be repeated, including accelerating RF cavities, in the cooling stage of a future muon facility. In this thesis, the AFC will be referred to by 'cooling cell' at times, while the term 'cooling channel' will refer to the assembly formed by the AFC and the two spectrometers, which was purposed to cool the muon beam and measure the effect.

The overarching aim of Step IV was to test the performance of the cooling cell for beams with central momentum in the 140-240 MeV/c range and with input normalized transverse emittance in the 3-10 mm range. To cover the emittance range, a diffuser of variable thickness was mounted at the entrance of the upstream spectrometer solenoid. It was composed of two brass and two tungsten irises remotely operated by an air-driven actuator [53]. The use of materials with short radiation length inflated the beam emittance via multiple Coulomb scattering.

3.3.1 Magnetic Lattice

The spectrometer solenoids (SS) were designed to provide a uniform axial magnetic field for the scintillating fibre trackers installed within their warm bore. Each SS consisted of five superconducting coils. The Centre (C), End 1 (E1) and End 2 (E2) coils produced a uniform field up to 4 T across the fiducial volume of the trackers [54]. Two match coils, M1 and M2, were used to transfer and match the beam in and out of the AFC. Due to a failure during quench training in September 2015, the M1 coil downstream was rendered unavailable for data collection in Step IV [55].

During the commissioning phase, it became apparent that the stray fields from the superconducting coils could damage the electronics of devices inside and outside of the MICE Hall. To mitigate for this, a partial return yoke (PRY) was built and installed around the cooling channel [56]. A picture of the cooling channel prior to the PRY installation can be seen in figure 3.4.

Initial and revised plans [45][46] set out to demonstrate "sustainable" ionisation cooling, by using multiple absorbers within a cooling cell and by restoring the longitudinal momentum via RF cavities placed between the absorbers. However, the Step IV configuration presented less complexity, with only one Absorber Focus Coil module used to induce a cooling effect and no longitudinal acceleration. The module was constructed to house the absorber material and to provide strong focusing at the absorber position, to reduce heating due to multiple Coulomb scattering, and thus enhance cooling [57]. Strong focusing was achieved by using two superconducting solenoids, and the module's flexible design allowed using a host of absorber types: a 22 l liquid hydrogen vessel [58], a 65 mm thick lithium hydride disk [59] and a polyethylene wedge [60].

The cooling channel could be operated in two modes. In the "solenoid mode", all the coils were set to the same polarity, while in the "flip mode" the six coils

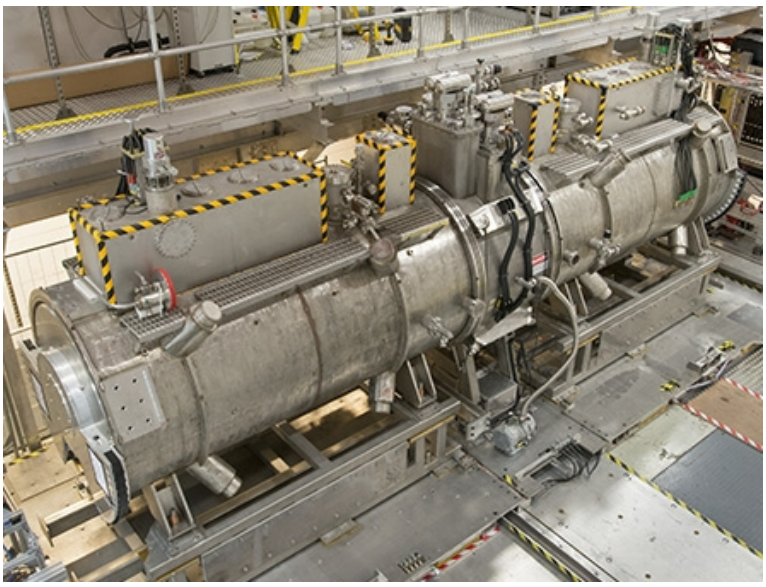

Figure 3.4: The cooling channel in the MICE hall, prior to the installation of the PRY. The Absorber Focus Coil module is placed between the two spectrometer solenoids [21].

downstream of the absorber were operated in a polarity opposite to the other coils. The flipped field polarity configuration is of high importance for a realistic cooling section within a future muon facility, as it prevents the build-up of canonical angular momentum, which is detrimental to the cooling performance [29][33].

3.3.2 Scintillating Fibre Trackers

MICE was a single particle experiment, a feature attributed to the two identical scintillating fibre trackers [61]. Immersed in uniform solenoid fields, the trackers reconstructed the trajectory and momentum of each muon upstream and downstream of the cooling cell. Each tracker (labelled TKU and TKD, for upstream and downstream, respectively) consisted of five detector stations (labelled 1 to 5, with station 1 being closest to the absorber) with an active circular area of 150 mm radius. The distances between adjacent stations were all different to ensure that each azimuthal rotation of track position from one station to the next was unique - this feature was used to resolve ambiguities during track reconstruction [62].

Each station was composed of three planes of 350 μm diameter scintillating fibres, rotated 120° with respect to their neighbour, as can be seen in figure 3.5.

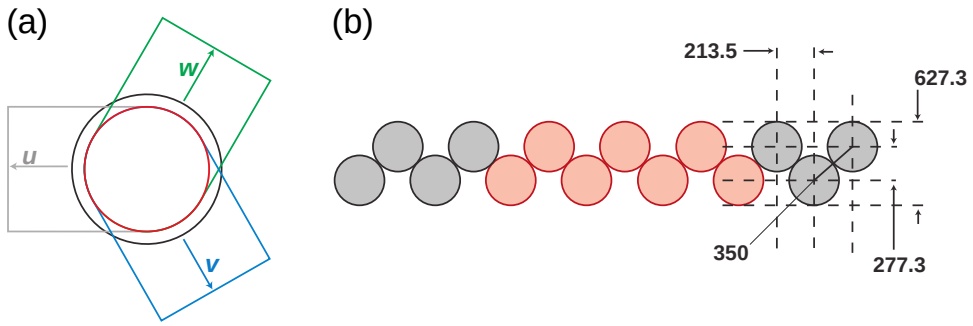

Figure 3.5: (a) Schematic diagram of the scintillating fibre plane arrangement in the tracker stations. The (black) outer circle represents the bore of the solenoid magnet, while the area within the (red) inner circle represents the active area of the tracker. The green, blue and grey regions and arrows illustrate the direction the individual 350 μm fibres run. (b) Layout of the scintillating fibres arrangement within each plane. The seven fibres depicted in red form a channel. Measurements are provided in microns [61].

As two planes were sufficient to infer an (x, y) position, a third plane was used to discriminate against noise by requiring a coincidence hit across all three planes. The scintillating fibres were bundled in groups of seven to form a channel, and the signal from each channel was transported outside of the magnet bore to a Visual Light Photon Counter (VLPC) via a clear-fibre light guide. The VLPCs were cooled to 9 K using four liquid helium cryostats to minimise thermal noise. The devices and their readout electronics were inherited from the D0 detector [63]. The performance of the tracker stations was assessed using cosmic rays and a 661 $\pm$ 2 μm position resolution was measured [61]. An assembled tracker can be seen in figure 3.6.

3.4 Particle Identification Detectors

A comprehensive set of particle detectors was used for particle identification (PID). Upstream of the cooling channel, a time-of-flight (TOF) system and a pair of Cherenkov threshold counters served for electron and pion rejection, while downstream a further time-of-flight station and two calorimeters were employed to identify muons that have decayed within the channel. The relative placement of the PID detectors with respect to the cooling channel is shown in figure 3.3. In this section, an overview of the PID detector system is presented. A detailed analysis of the performance of the MICE diagnostics is published in [64].

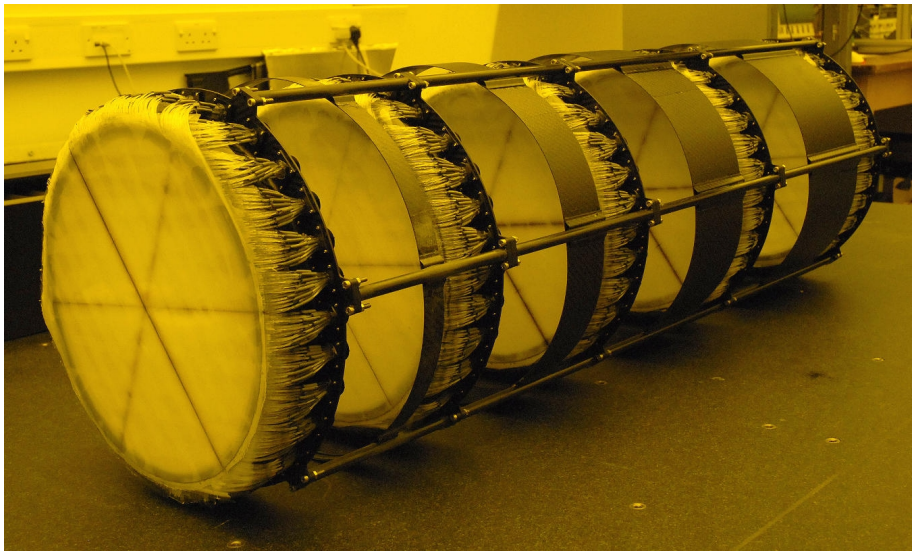

Figure 3.6: Photograph of one of the MICE trackers, showing the five stations. The black lines on each station indicate the direction of the double layers of fibres [21].

3.4.1 Time-of-Flight Detectors

The main PID detectors were three TOF scintillator hodoscopes, which provided highly efficient upstream particle discrimination and were used as the trigger for the experiment. Additionally, the longitudinal momentum of particles could be inferred from the TOF measurements by assuming a mass hypothesis. TOF0 and TOF1 [65, 66, 67] were positioned upstream of the cooling channel, with TOF1 placed at its entrance, and TOF2 [68] placed at the exit of the channel, in front of the calorimetry system.

All three TOF stations were made of two layers (one horizontal and one vertical) of 1 inch thick scintillator bars, as shown in figure 3.7. This arrangement allowed the TOFs to perform coarse position measurements, acting as low-resolution beam profile monitors. Owing to the high precision of the individual stations ($\sim$ 50 ps), a resolution of 100 ps was achieved for the TOF01 system. This converted into a pion contamination rejection efficiency of $\sim$ 99% for beams with momentum up to $\sim$ 210 MeV/c [52]. The time-of-flight distribution for a beam with nominal input momentum of 140 MeV/c is shown in figure 3.8, with a clear separation between the muon and pion peaks.

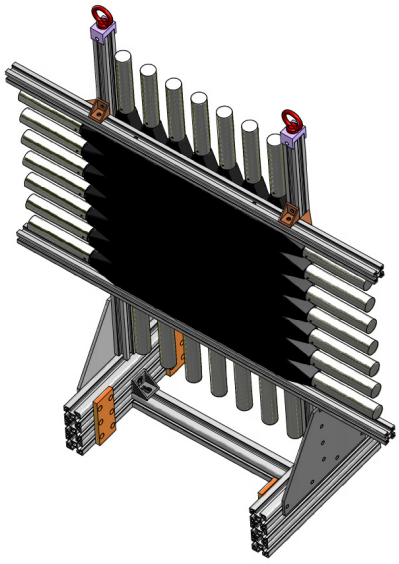

Figure 3.7: Three-dimensional CAD design of the TOF1 detector and its support structure [69].

3.4.2 Cherenkov Detectors

At momenta higher than 210 MeV/c, the precision of the TOF01 system was not sufficient to meet the upstream PID efficiency requirements. Two Cherenkov threshold counters were designed and used to aid with the muon/pion separation for beams with momenta in the 210-360 MeV/c regime [70]. An exploded view of the detectors is shown in figure 3.9. Cherenkov radiation emitted by high density silica aerogels with refractive indices of 1.07 (CkovA) and 1.12 (CkovB) was collected by four photomultipliers (PMTs) in each counter. The choice of refractive indices provided thresholds for muon detection at 278 MeV/c (CkovA) and 210 MeV/c (CkovB), while for pions the thresholds were at 367 MeV/c (CkovA) and 276 MeV/c (CkovB).

3.4.3 KLOE-Light Calorimeter

Downstream of the cooling channel, the electron/muon separation was performed by the Electron Muon calorimeter (EMCAL) assembly and TOF2. The first element of the EMCAL, placed just downstream of the TOF2, was the KLOE-Light (KL) pre-shower sampling calorimeter. It was designed to initiate electron showers, while letting muons through, and to provide energy deposition and timing information.

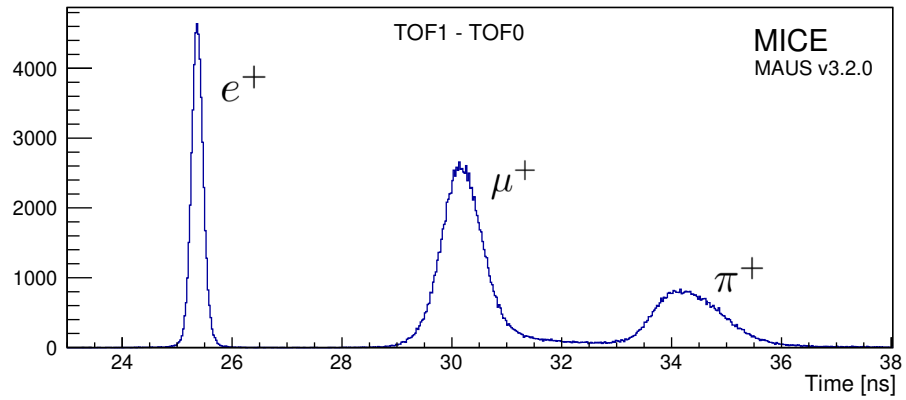

Figure 3.8: The time-of-flight for a 140 MeV/c nominal momentum 'calibration' beam between the first two TOFs [64].

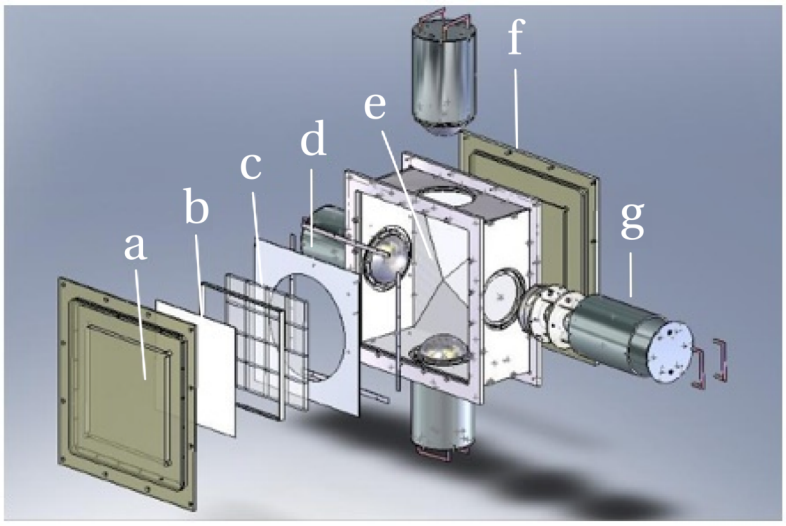

Figure 3.9: MICE aerogel Cherenkov detector: a) entrance window, b) mirror, c) aerogel mosaic, d) acetate window, e) reflector panel, f) exit window and g) eight inch PMT in iron shield. Figure adapted from [51].

Sharing a similar design concept with the KLOE experiment calorimeter [71], the KL was formed of 21 cells of 1 mm diameter scintillating fibres within extruded lead foils, in a 2:1 volume ratio of scintillator:Pb. Its 4 cm thickness was equivalent to 2.5 radiation lengths. The light from the fibres was collected by Winston cone light guides and delivered to two PMTs, one at each end of the cell. Figure 3.10 depicts a schematic diagram of a slab formed of three cells, as well as the substructure of each cell. It achieved an energy resolution of $\sigma_E/E \approx 7\,\%/\sqrt{E(\mathrm{GeV})}$ and a time

resolution of $\sigma_t = 70\,\mathrm{ps}/\sqrt{E(\mathrm{GeV})}$ [72].

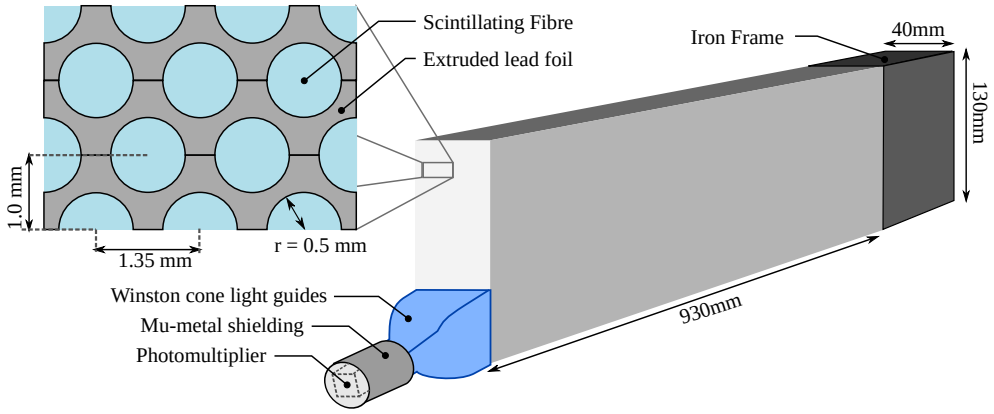

Figure 3.10: (Right) Diagram of a MICE KL calorimeter slab, as well as (left) a magnified schematic of its substructure. Figure adapted from [73].

3.4.4 Electron Muon Ranger

The pre-showers caused by the KL, as well as muons, impinged on the Electron Muon Ranger (EMR), the second element of the EMCAL and the most downstream detector of the experiment. The EMR was a fully active tracking calorimeter, designed primarily to distinguish between muons and decay electrons [74]. It was also used to reconstruct the muon momenta in the 100-280 MeV/c range.

The calorimeter was composed of triangular scintillator bars that were tessellated together to form planes. Each plane consisted of 59 bars, and a total of 48 planes formed the active volume of the detector. Consecutive planes were placed perpendicularly to provide position information. The cross section of the bars and their arrangement in a plane can be seen in figure 3.11, as well as a CAD drawing of the whole detector. Each bar contained a wavelength shifting (WLS) fibre, which was used to collect and transport the light PMTs placed at each end of the bar. At one end of the plane, all the WLS fibres were read out together to measure the energy deposited in the entire plane, while at the opposite end, individual read out of the WLS fibres allowed for the measurement of energy deposition in each bar.

The particle species were identified by the corresponding unique behaviour within the detector. Muons produced a single track before either stopping, decaying or

exiting the active volume. Owing to the KL, the electrons would shower and produce a cascade of secondary particles, which generated a substantially different pattern. The EMR was measured to identify electrons with an efficiency of 98.6% [74].

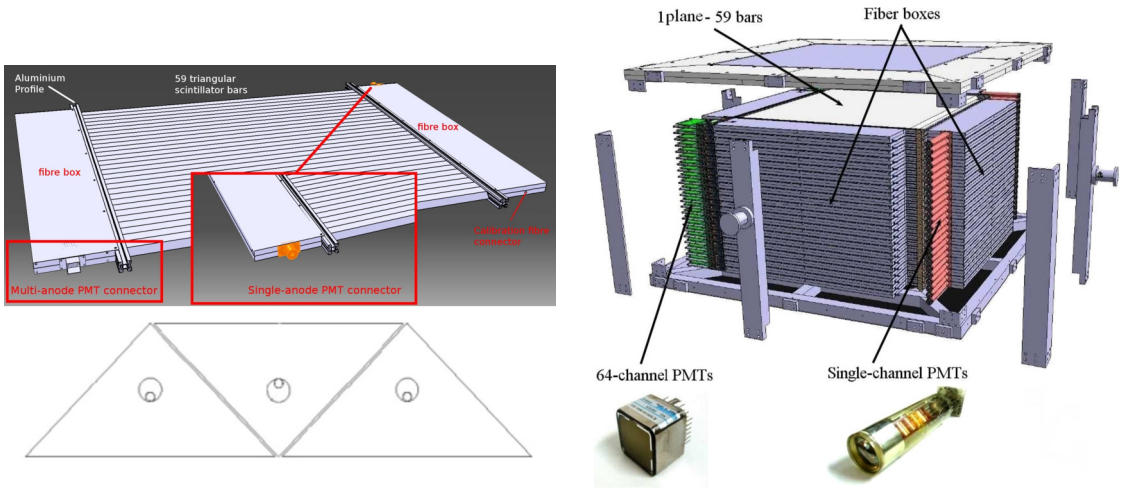

Figure 3.11: (Left, bottom) Cross section of the scintillating bar arrangement in an EMR plane. (Left, top) CAD drawing of an EMR plane [74]. (Right) CAD drawing of the detector made from a stack of 48 planes [75].

3.5 Analysis Software

The reconstruction, simulation and analysis tools are provided by the MICE Analysis User Software (MAUS) [76], which is written in C++ and Python. The simulation of the MICE experiment is handled by multiple packages.

Simulated particles produced by using a representative model of the pion yield at the target are transported to 1 m downstream of the second dipole magnet, D2, using G4Beamline [77]. At this location, the simulation is handed over to the MAUS software, which relies on the Geant4 package for particle tracking through matter and simulation of physics processes [78]. The beam is then propagated through the entire MICE channel and the virtual hits in the detectors are digitized by detector-specific response and readout electronics models.

MAUS also provides reconstruction capabilities. Both the simulation-based digitized hits and the real data DAQ digits are fed into the detector reconstruction algorithms, which, by design, work in same fashion for simulation and real data.

The reconstructed outputs of individual detectors are combined to form a global track. The information contained by each track (event) is saved into a ROOT [79] file, readily accessible for higher level analysis.

Chapter 4

Normalised Transverse Emittance Reduction in MICE 'Flip Mode'

The Muon Ionisation Cooling Experiment (MICE) was designed to conduct the first measurement of normalised transverse RMS emittance reduction in a muon beam. A first MICE analysis on muon cooling was focused on the core of the beam, where an increase in the number of low-amplitude muons and in phase space density has been observed upon beam passage through an absorber material [22].

The analysis presented in this chapter is devised to quantify the muon cooling performance through the change in transverse emittance, which is a key figure of merit for ionisation cooling and accelerator design. Improper beam matching into the upstream spectrometer solenoid resulted in a suboptimal beam betatron function at the absorber. A novel beam selection routine based on rejection sampling and kernel density estimation is developed to obtain properly matched beam subsamples. The emittance reduction in a lithium hydride and a liquid hydrogen absorber is studied for an array of input beam emittances. The data sets in this analysis were collected using a MICE cooling channel configuration that produced a magnetic field with flipped polarity at the absorber.

4.1 Equipment Settings

The data analysed in this chapter were collected in the MICE Step IV configuration. The focus of the study is on transverse emittance reduction in a 22 l vessel filled with liquid hydrogen or a 65 mm thick lithium hydride disk, both housed in the AFC module. The configurations with the empty vessel or no absorber mounted are also analysed. For each absorber setting, three beam line configurations were used to deliver muon beams with nominal emittances of 4, 6 and 10 mm and a central momentum of approximately 140 MeV/c in the upstream tracker. These configurations are referred to in this thesis as '4-140', '6-140' and '10-140'.

For the data presented here, the magnetic channel coils were operated only in one configuration, labelled as '2017-2.7'. It was the result of an optimisation study performed after the M1D coil became unusable during the commissioning of the SSD. The study aimed to maximise the cooling performance by maintaining the transverse $\beta_\perp$ function at the absorber as low as possibile while limiting the particle loss by scraping in the downstream half of the channel [80]. The individual coil currents for this setting are presented in table 4.1. The corresponding modelled on-axis longitudinal magnetic field is shown in figure 4.1. The field flips polarity at the absorber. Referred to as 'flip mode', this configuration was implemented to prevent an increase in canonical angular momentum at the absorber.

	SSU			AFC		SSD			
Setting	ECE	M2	M1	FC0	FC1	M1	M2	ECE	Mode
2017.02-7	205.7	168.3	191.0	129.2	129.2	0	195.7	144.0	Flip

Table 4.1: Cooling channel coil currents in the 2017-2.7 setting. ECE stands for the group of E1, C and E2 coils, as shown in figure 3.3. The channel was powered in flip mode, hence all SSU coils and FC0 had positive polarity, while FC1 and all working SSD coils had negative polarity. The current values are quoted in amperes.

4.2 Trackers

The main detectors in MICE are the two trackers immersed in the uniform fields of the upstream and downstream spectrometer solenoids, referred to in this thesis as TKU and TKD. A description of the trackers is given in section 3.3.2. Particles entering the tracking region evolve in a helical trajectory, with radius and wavelength

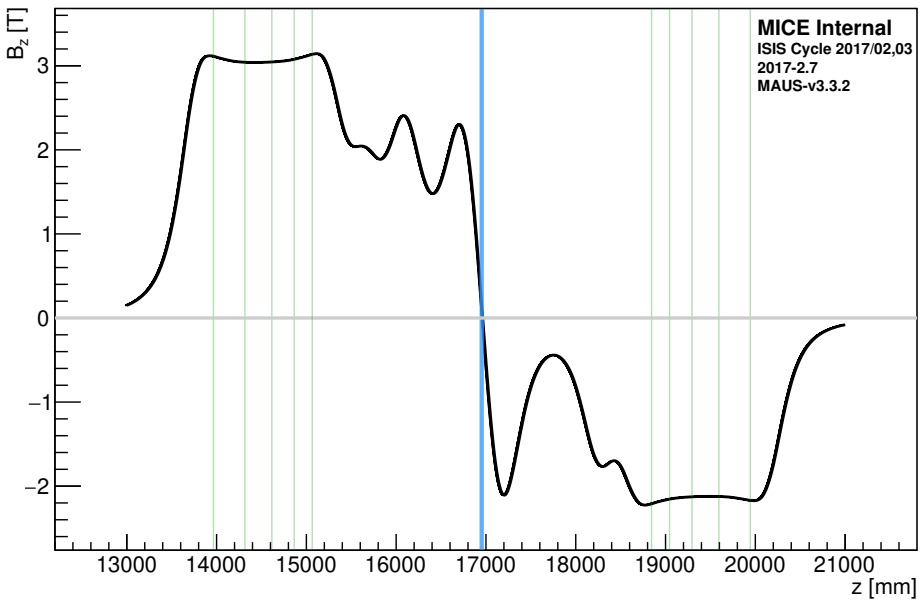

Figure 4.1: On-axis longitudinal magnetic field in the 2017-2.7 magnetic channel setting of MICE Step IV. The vertical blue line indicates the position of the absorber centre and the vertical green lines show the locations of the tracker stations. The position along the cooling channel is reported in the global coordinate system of the experiment, where $z = 0$ at the D2 dipole.

depending on the transverse and longitudinal momenta, respectively, as follows:

$$R = \frac{p_\perp}{qB_z}, \tag{4.1}$$

$$\lambda = \frac{2\pi p_z}{qB_z}. \tag{4.2}$$

The ratio between the transverse and longitudinal momenta influences the rate of change of the track arc length, s, with respect to the longitudinal coordinate, z, via

$$\frac{ds}{dz} = \frac{p_\perp}{p_z}. \tag{4.3}$$

The track reconstruction process is executed in stages. A brief summary of the process is given here, while the reconstruction algorithms and their performance are described in more detail in [62][81][82]. Electronics signals from neighbouring fibres are grouped into clusters. In each station, clusters from two or three of its

constituent planes are used to form a space point, which gives the position of the hit in the $x - y$ plane. A pattern recognition routine attempts an ideal helix fit to the space points. In its first stage, a circle fit is performed in the $x - y$ plane, to determine the helix radius, and through equation 4.1, the transverse momentum. If successful, a linear fit in the $s - z$ plane is used to estimate the longitudinal momentum via equation 4.3.

For tracks with low $p_\perp$, the vanishingly small value of ds/dz leads to a diverging uncertainty on the p_z estimate. A selection based on the longitudinal or total momentum would exclude a larger proportion of the low $p_\perp$ events due to the corresponding unstable p_z estimate. This built-in limitation of the trackers can be alleviated with the help of another detector system. A procedure using the estimate of the muon momentum at the upstream side of the TOF1 to improve the p_z reconstruction has been implemented in MAUS and is described in detail in [83]. The momentum estimated from the time-of-flight between TOF0 and TOF1, p_{TOF01}, is calculated as

$$p_{\mathrm{TOF01}} = \frac{m_\mu c}{\sqrt{(t_\mu/t_e)^2 - 1}}, \tag{4.4}$$

where t_μ is the muon time-of-flight and t_e is the mean positron time-of-flight.

4.2.1 Magnetic Field

Equation 4.1 shows that once the radius of the helix is determined, the accuracy of momentum reconstruction depends directly on the knowledge of the magnetic field within the tracking region. The field map used for reconstruction (and simulation) is generated in MAUS by using coil models provided with the dimensions and positions of the actual MICE superconducting coils [84].

A set of Hall probes was used to monitor the field in the tracking region during data gathering. All probes were placed at 160 mm radius from the beam axis. Their longitudinal and azimuthal coordinates are listed in table 4.2. The distributions of readings for the 2017/02 and 2017/03 user cycles are shown in figures 4.2 and 4.3, respectively. The Hall probes demonstrate a resolution of about 10^{-4} T. Hence, the model currents of the SSU and SSD coils have been scaled such that the field model matched the Hall probe measurements.

Prior to the decommissioning of the MICE cooling channel, the field within SSU

Hall Probe	Position [mm]	ϕ [°]
SSU-65	14429	30
SSU-77	14104	30
SSU-79	14429	270
SSD-72	19482	330

Table 4.2: Longitudinal and azimuthal positions of the Hall probes.

and SSD was measured with a CERN custom built field mapper [85]. The aim was to gain a better understanding of the effects of the partial return yoke and magnet re-training on the field. A comprehensive study based on this measurement has been published in [86], but due to lack of resources the knowledge gain has not been implemented in the MAUS field model. The new measurement was found to agree with Hall probe readings. By fitting the data to a field model, a $\sim 1\%$ variance was found in the distribution of residuals calculated in the tracking region. This will be treated as a systematic uncertainty on the field.

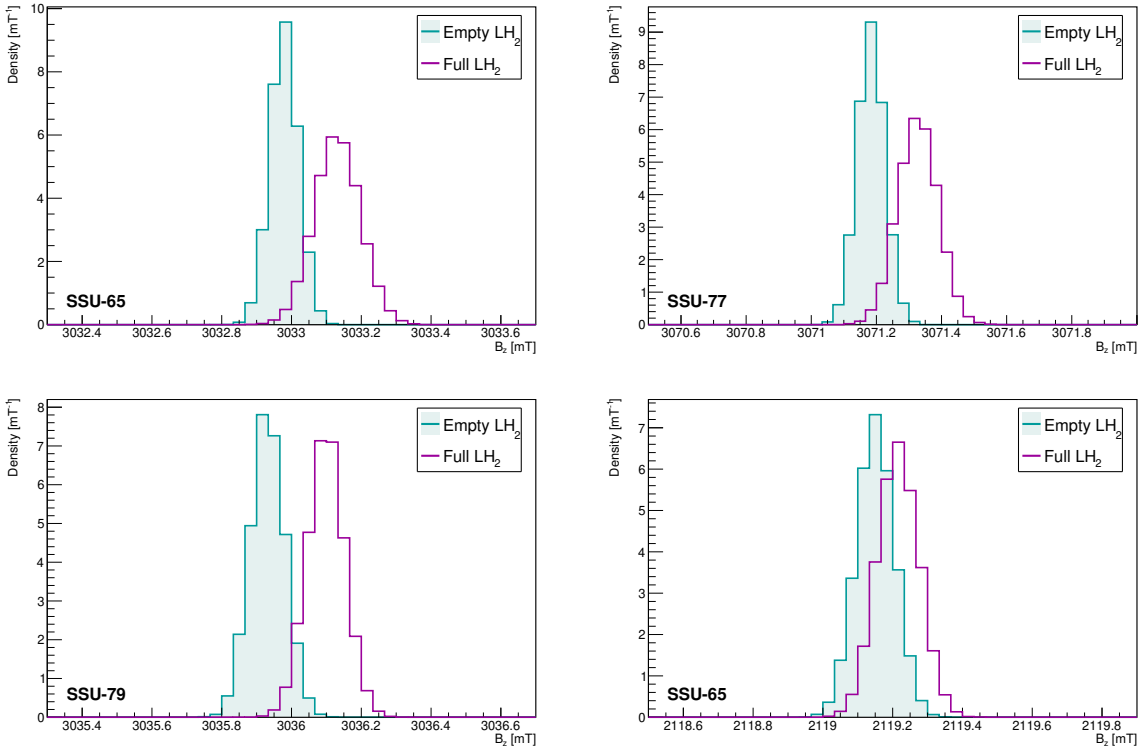

Figure 4.2: Hall probe readings distributions during the 2017/02 data collection cycle for runs with both full and empty LH_2 vessel.

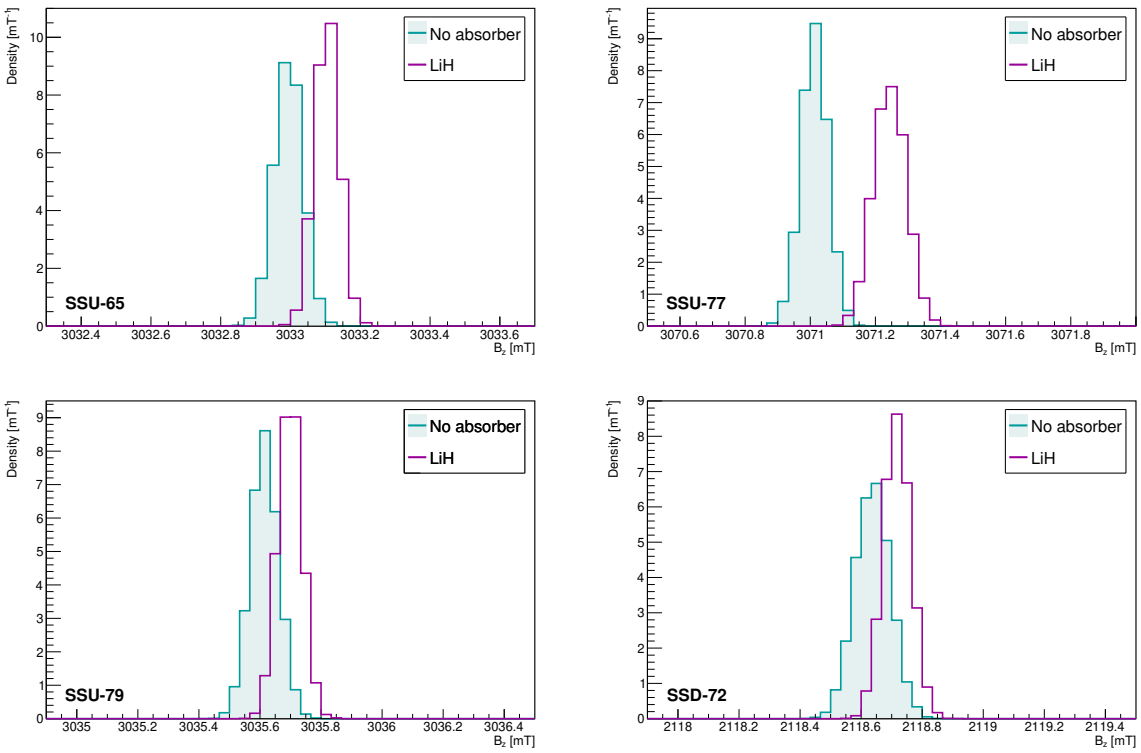

Figure 4.3: Hall probe readings distributions during the 2017/03 data collection cycle for runs with and without the LiH absorber in place.

4.2.2 Resolution and Efficiency

The full simulation of the MICE experiment is used to evaluate the resolution and efficiency of the two trackers. In each tracker, true muons that evolve within the fiducial radius of 150 mm and reach the most downstream station are recorded with their true phase space coordinates at the reference plane, i.e., the plane closest to the absorber module. For each true muon in the sample, if a reconstructed track is found, it is recorded in identical fashion.

The simulated resolutions for both trackers are shown in figure 4.4. The momentum reconstruction shows a small bias, which may be generated by a simulated misalignment between the tracker and the field or by the $x - y$ coupling generated by the angular momentum. Larger tails are observed for the p_z reconstruction due to the challenges encountered in the low $p_\perp$ regime. The resolution in TKD is worse than in TKU, as the magnitude of the field in which it is placed is 2 T rather than 3 T.

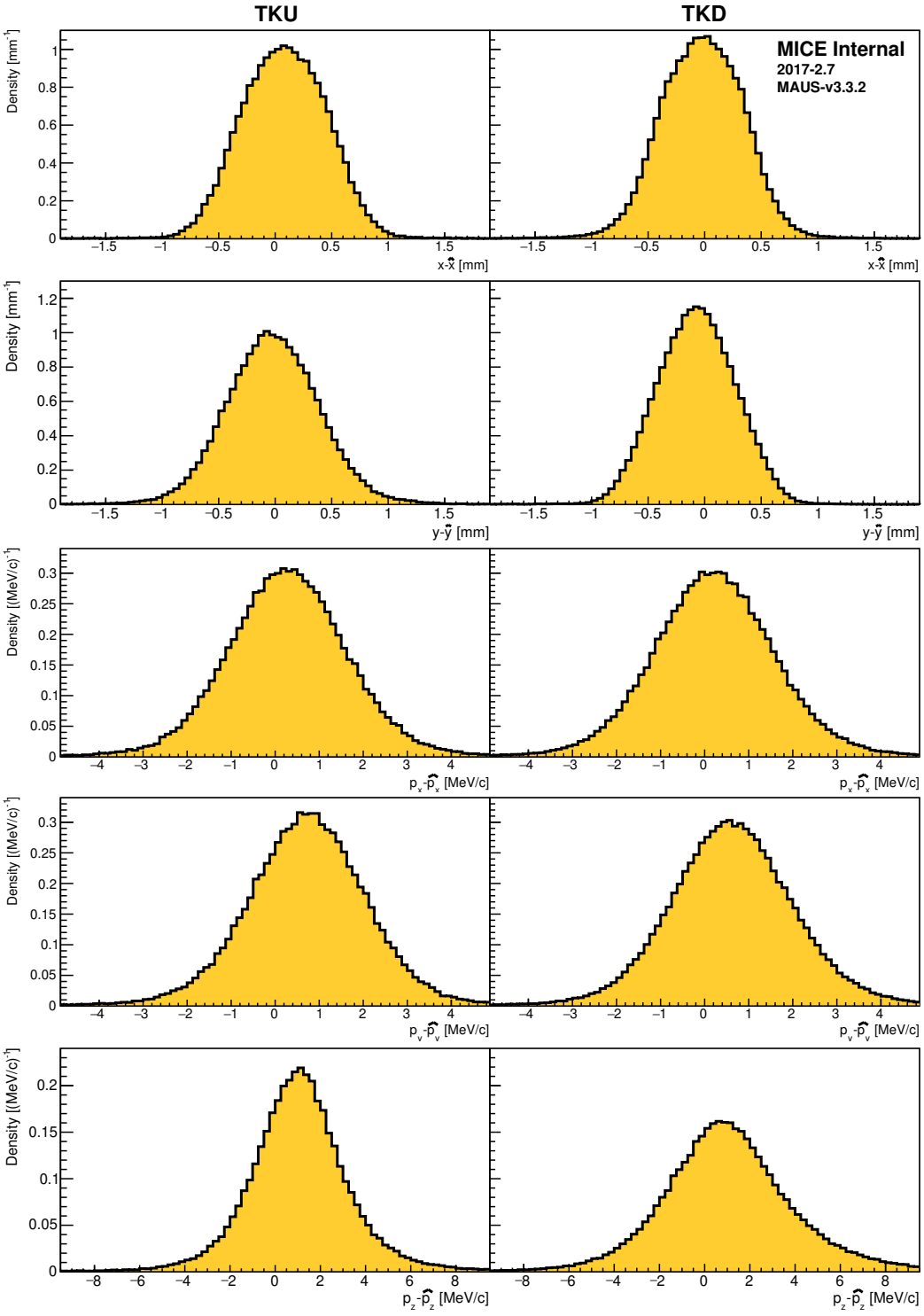

Figure 4.4: Simulated residual distributions for the (x, y, p_x, p_y, p_z) phase space variables reconstructed in the two trackers.

The simulated efficiencies of the two trackers are shown as a function of transverse momentum in figure 4.5. For both trackers, a slight decline in efficiency is observed towards high $p_\perp$. This effect is likely caused by the simulated dead channels in the scintillating fibre planes that coincidentally affect this region of the phase space [82]. It may also occur as the helical trajectory of high amplitude muons is deformed in the non-uniform fields close to the end coils and becomes more difficult to reconstruct. Additionally, the downstream tracker presents a small inefficiency at low $p_\perp$. The helix radius of low $p_\perp$ muons becomes comparable to the trajectory deviations induced by scattering in the tracker stations, making the track reconstruction more prone to failure. The simulated efficiencies have not been compared with the measurement efficiencies.

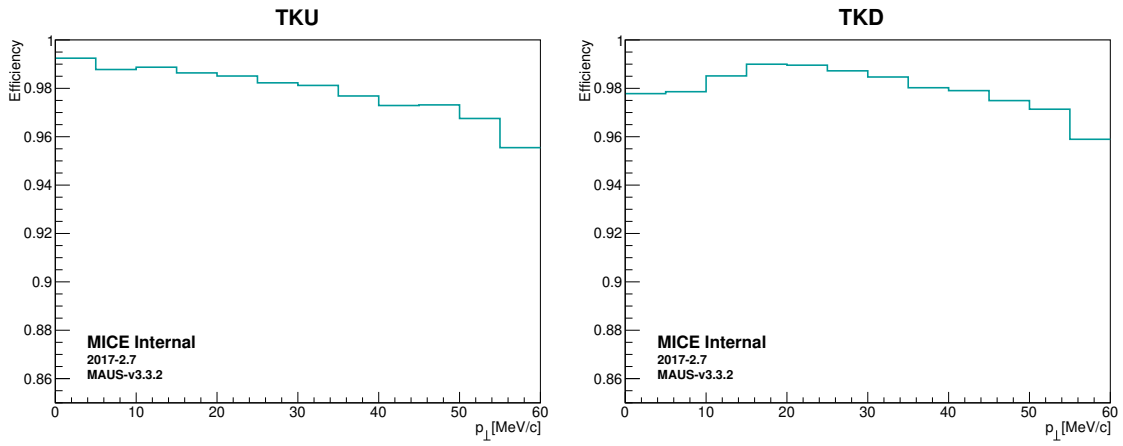

Figure 4.5: Track reconstruction efficiency for the (left) upstream and (right) downstream trackers as a function of transverse momentum.

4.3 Event Selection

The MICE data acquisition system was set up to trigger if the TOF1 detector recorded a coincidence of signals in the two PMTs of a single slab. All the data collected by the detector system during the trigger window was aggregated and formed a particle event.

The particle events are subjected to a host of criteria, referred to as cuts, and only events that meet all the criteria are integrated into the analysis. The series of cuts ensure that a pure muon beam with a small momentum spread and which is fully transmitted through the cooling channel is selected for analysis.

4.3.1 Particle Identification

The time-of-flight system situated upstream of the cooling channel, known as TOF01, is used for muon tagging. The cuts applied on TOF-related measurements are described below:

- *Time-of-flight between TOF0 and TOF1*: The three particle species that traverse the TOF01 system - muons, pions and electrons - have distinguishable transit times and exhibit a three-peak distribution, as shown in figure 4.6. Only events with a TOF01 time consistent with that of a muon are selected. Beams with higher input emittance traverse more material in the diffuser, losing more energy. To compensate for this loss and deliver a beam peaked at 140 MeV/c in TKU, the momentum upstream of the diffuser selected by the D2 dipole is larger. As such, different TOF01 cuts are applied for the 10-140 beam line setting, as shown in table 4.3.

- *One reconstructed space point in TOF0 and TOF1*: A space point is formed by a coincidence of hits in a pair of scintillator slabs arranged perpendicular to each other. Only events with a single space point in both TOF0 and TOF1 are selected.

- *Particle consistent with a muon in TKU*: The energy lost between TOF1 and TKU can be estimated using the time-of-flight momentum reconstruction given by equation 4.4. Only events that are within 5 σ of the expected energy loss for a muon are selected. This cut removes particles that either scrape apertures, are poorly reconstructed, or are pions that have passed the time-of-flight cut.

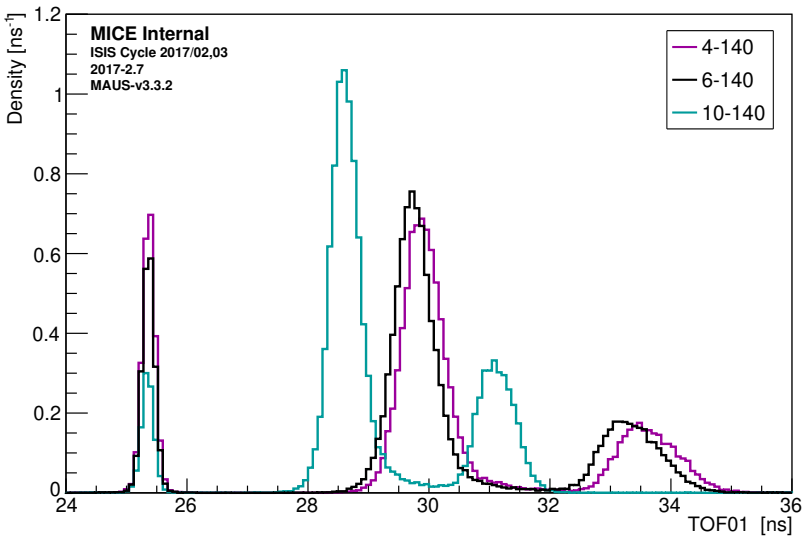

Figure 4.6: Distribution of time-of-flight between TOF0 and TOF1 for beams with nominal input emittance of 4, 6 and 10 mm and central momentum of 140 MeV/c at the cooling channel entrance.

Beam line setting	Lower cut [ns]	Upper cut [ns]
4-140	28.0	31.5
6-140	28.0	31.5
10-140	27.5	30.0

Table 4.3: TOF01 time cut bounds for the three beam line settings.

4.3.2 Track Reconstruction

The cuts applied on quantities derived from track reconstruction are listed below:

- *One reconstructed track in each tracker*: Only events that are fully transmitted through the cooling channel are analysed. If events with a track in TKU and no track in TKD were considered, the emittance measurement in TKD would be biased by the loss of particles and the cooling signal would be artificially enhanced.

- *Fiducial cut*: In each tracker, the helix fit must be contained within the cylindrical fiducial volume of the detector defined by a radius of 150 mm. This requirement removes tracks that scrape the tracker apertures and reenter the fiducial volume.

- χ^2 *per number of degrees of freedom*: In each tracker, the helix fit is required to have a χ^2/D.o.F. less than or equal to 8. This cut removes poorly reconstructed tracks from the sample.

- *TKU momentum*: Events reconstructed in the upstream tracker are required to have total momentum in the 135-145 MeV/c range.

- *TKD momentum*: Events reconstructed in the downstream tracker are required to have total momentum between 90 and 170 MeV/c for data collected when the absorbers were in place, and between 120 and 170 MeV/c for data collected with no absorber in place or with an empty liquid hydrogen vessel.

- *Diffuser aperture cut*: Tracks are back-extrapolated to the entrance of the diffuser and their radial excursion from the axis at that position must be less than or equal to 90 mm. Muons that pass through the annulus or the support material of the diffuser and lose a considerable amount of energy are excluded.

4.3.3 Final Samples

The effect of the cuts on the reconstructed data and reconstructed Monte Carlo simulations (MC) is shown in figures 4.7-4.13. The 1D or 2D distributions are grouped into 4×3 panels – one column for each of the 4-140, 6-140 and 10-140 beam line settings, and one row for each absorber setting, i.e., an empty liquid hydrogen vessel ('Empty LH_2'), a filled liquid hydrogen vessel ('Full LH_2'), no absorber ('No absorber') and a lithium hydride absorber ('LiH'). For 1D distributions, the data are represented in black filled circles, while the MC is shown in yellow fill. In the 2D case, the simulation distributions are shown in a separate panel in the same figure. Each histogram contains events that are accepted by all cuts other than the cut under examination. The bounds of the cuts are indicated by the red dashed lines. Very good agreement between the data and the simulation is observed, confirming the comprehensive understanding of the experimental hardware and the event reconstruction procedure.

The numbers of events surviving each selection criterion are shown in table 4.4. The figure associated with each cut indicates the number of events that pass that cut only. The numbers in bold at the bottom of each column represent the size of each final sample that is considered for analysis.

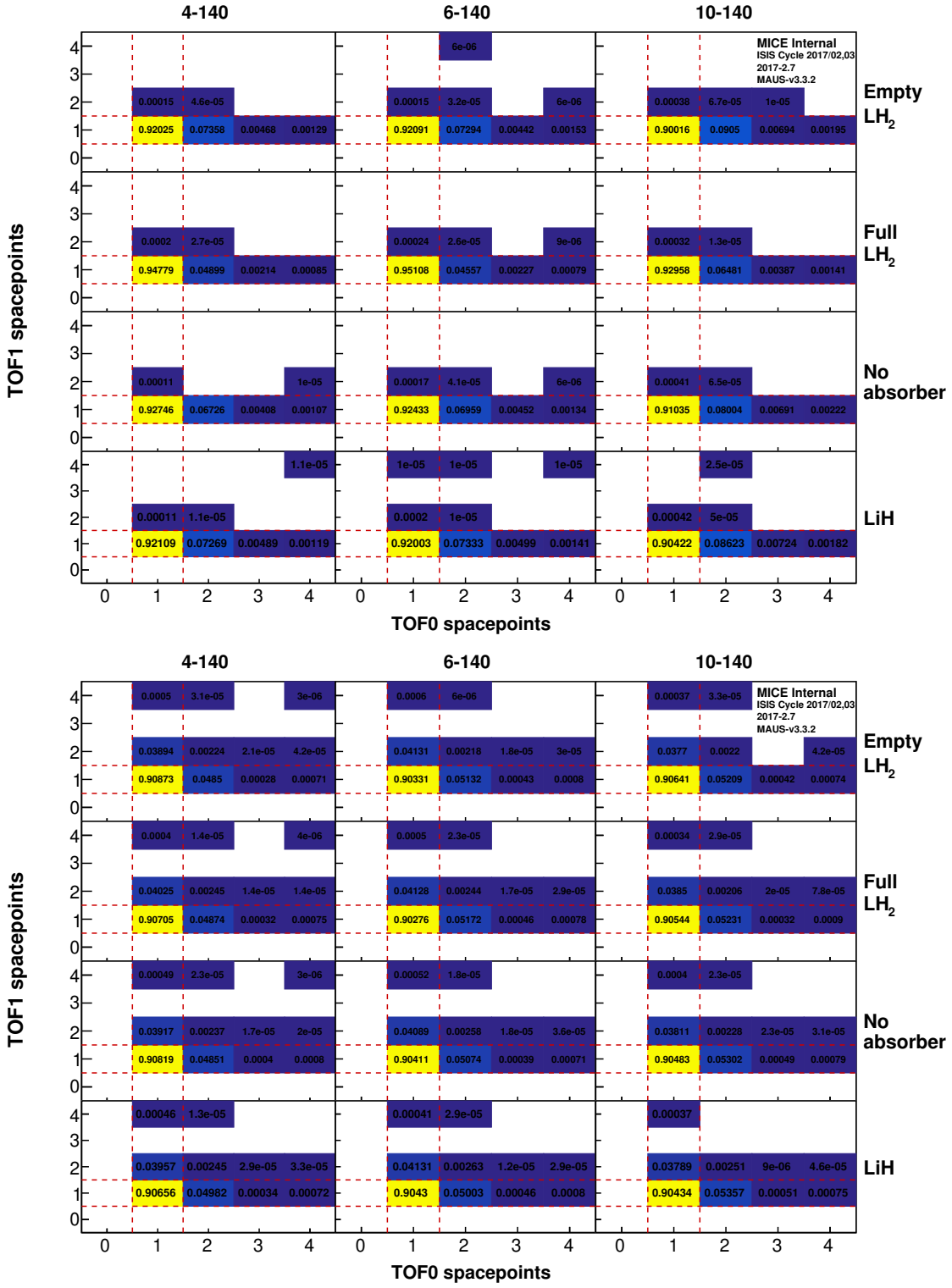

Figure 4.7: The number of TOF0 and TOF1 space points for the (top) reconstructed data and (bottom) reconstructed simulation samples. The histograms contain events that are accepted by all cuts other than the cut under examination. The number in each bin represents the sample fraction contained by that bin.

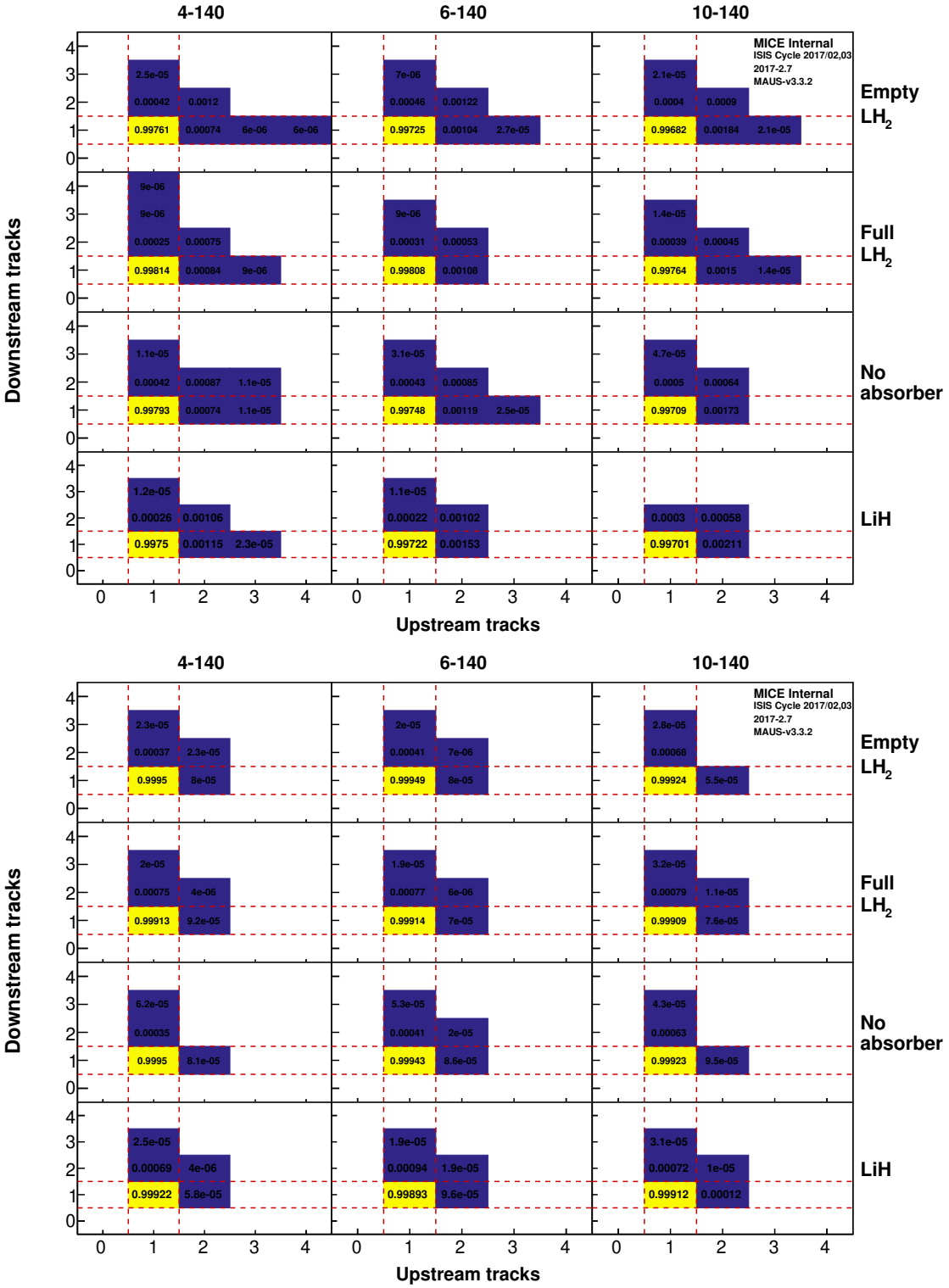

Figure 4.8: The number of TKU and TKD tracks for the (top) reconstructed data and (bottom) reconstructed simulation samples. The histograms contain events that are accepted by all cuts other than the cut under examination. The number in each bin represents the sample fraction contained by that bin.

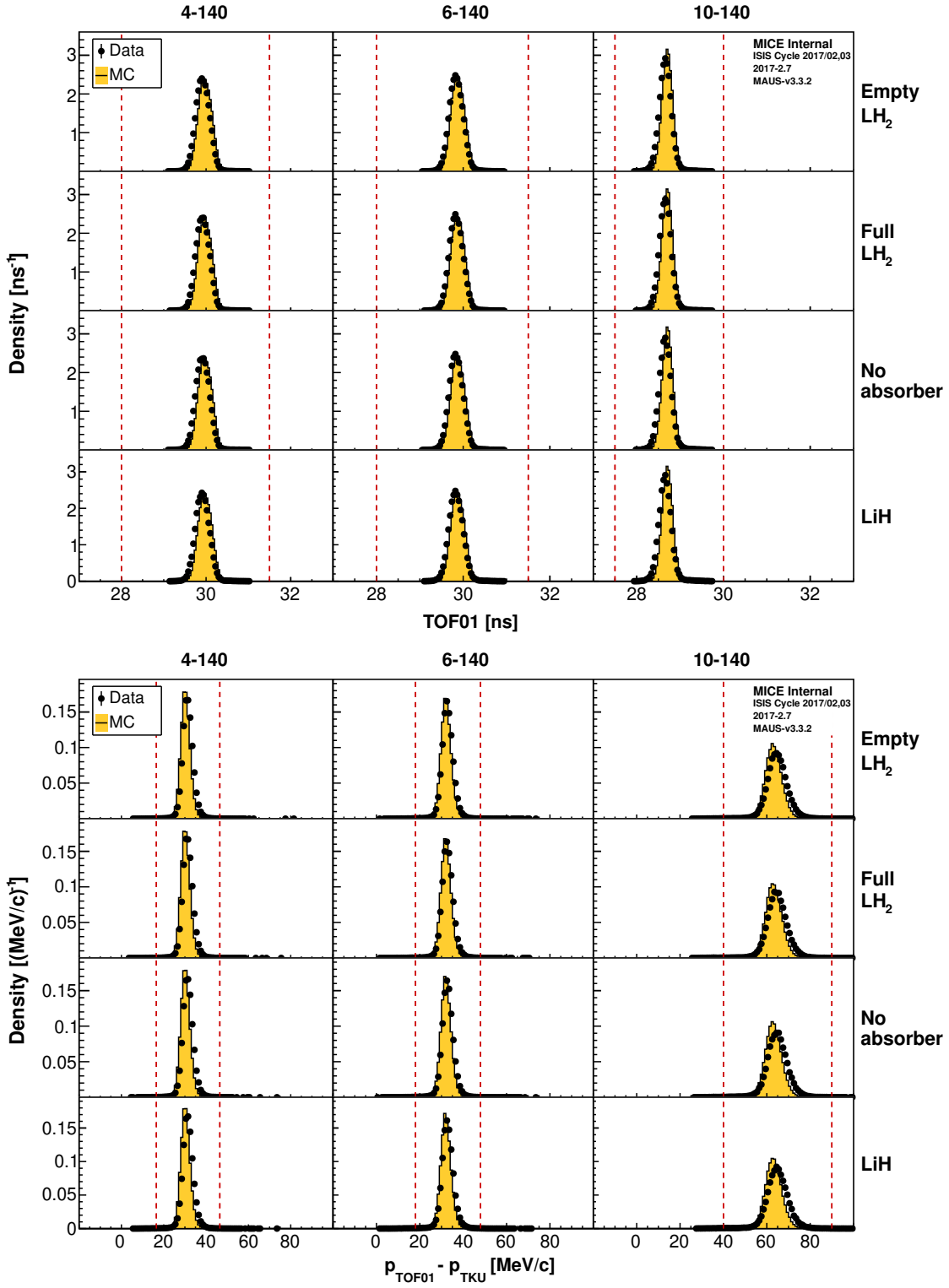

Figure 4.9: (top) Time-of-flight measured between TOF0 and TOF1. (bottom) Momentum lost between TOF1 and the TKU reference plane. The histograms contain events that are accepted by all cuts other than the cut under examination.

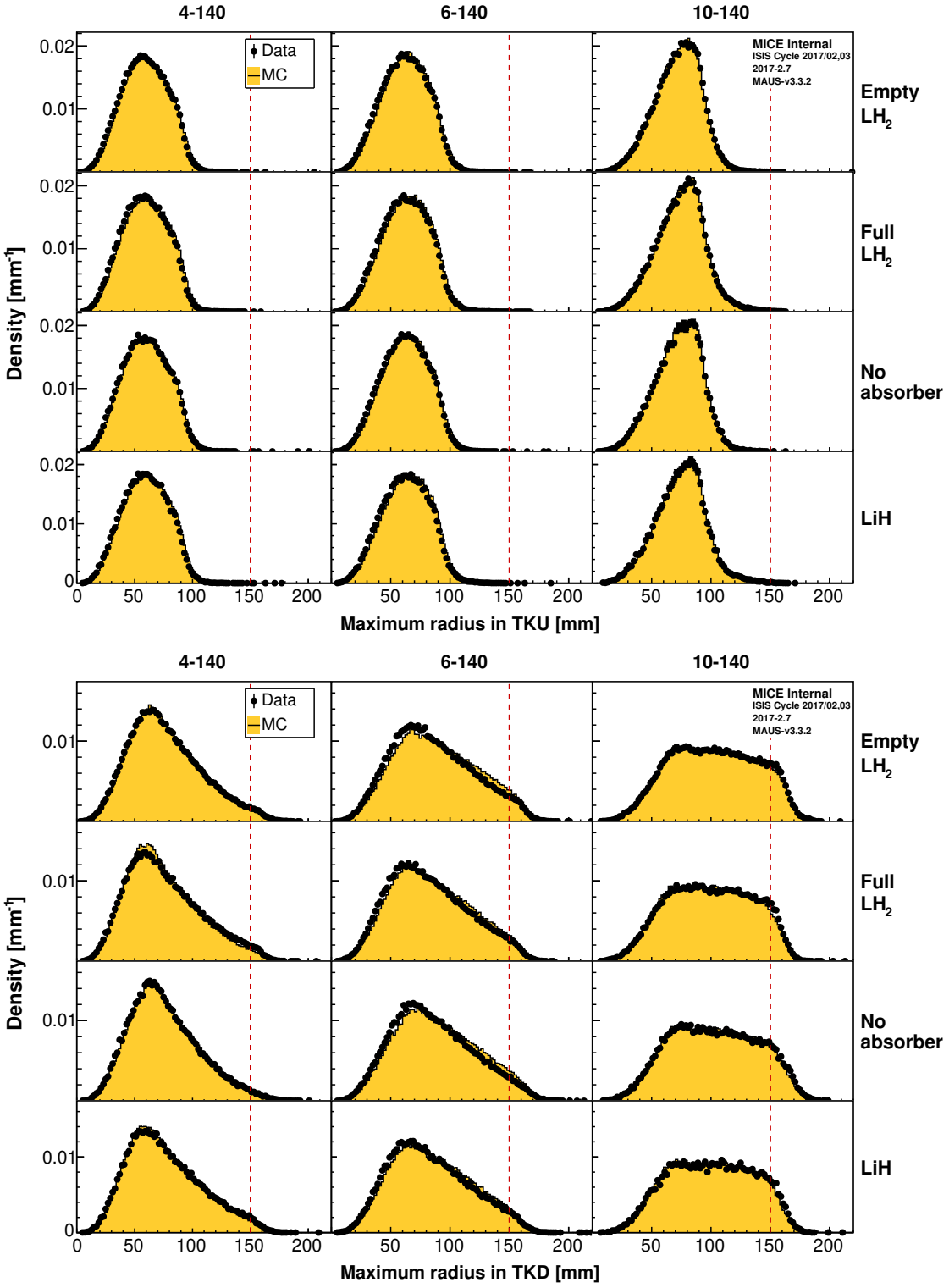

Figure 4.10: Maximum track radius in (top) TKU and (bottom) TKD. The histograms contain events that are accepted by all cuts other than the cut under examination.

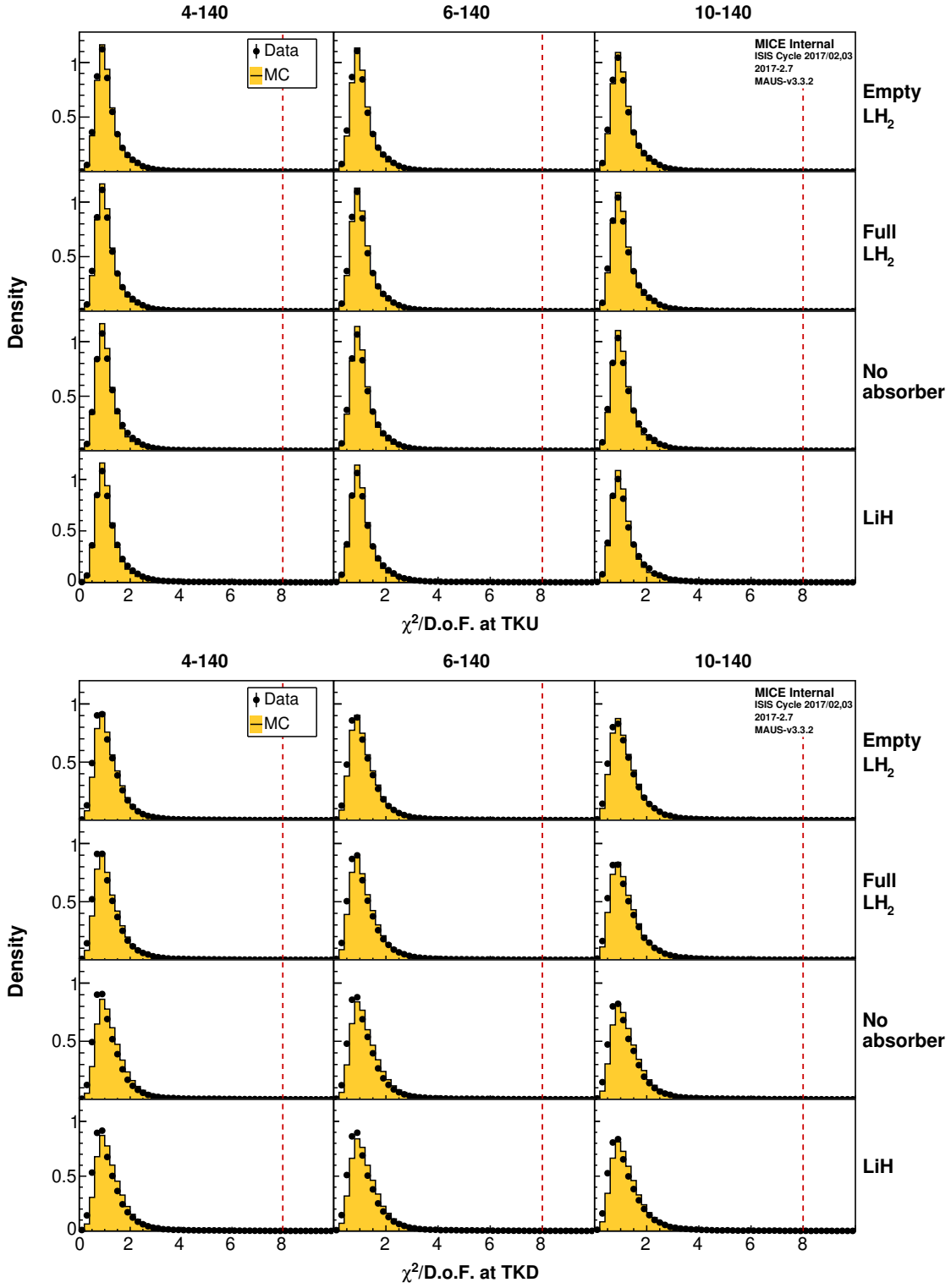

Figure 4.11: χ^2 per degree of freedom distribution for (top) TKU and (bottom) TKD track reconstruction. The histograms contain events that are accepted by all cuts other than the cut under examination.

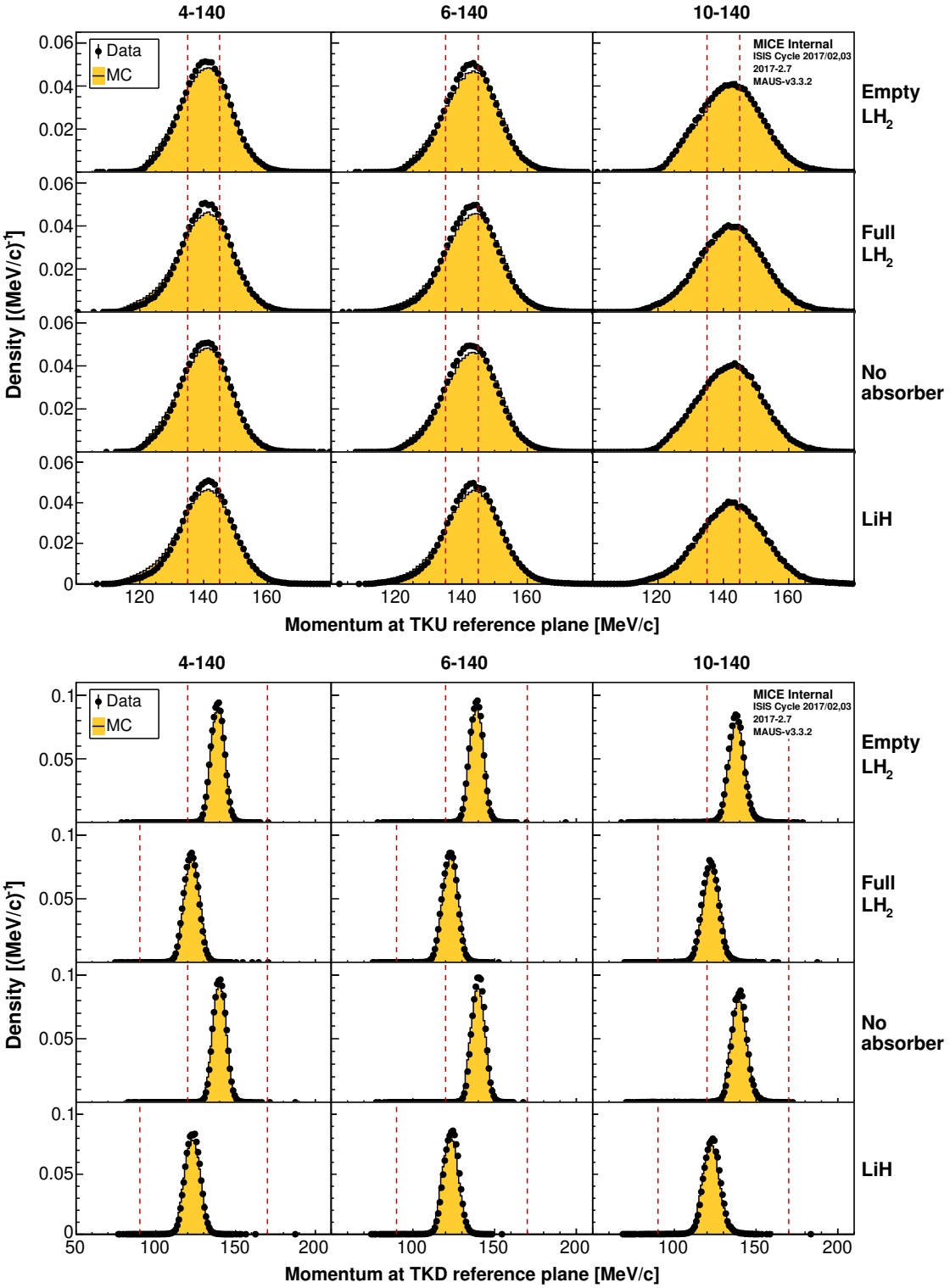

Figure 4.12: Reconstructed total momentum at (top) TKU and (bottom) TKD reference plane. The histograms contain events that are accepted by all cuts other than the cut under examination.

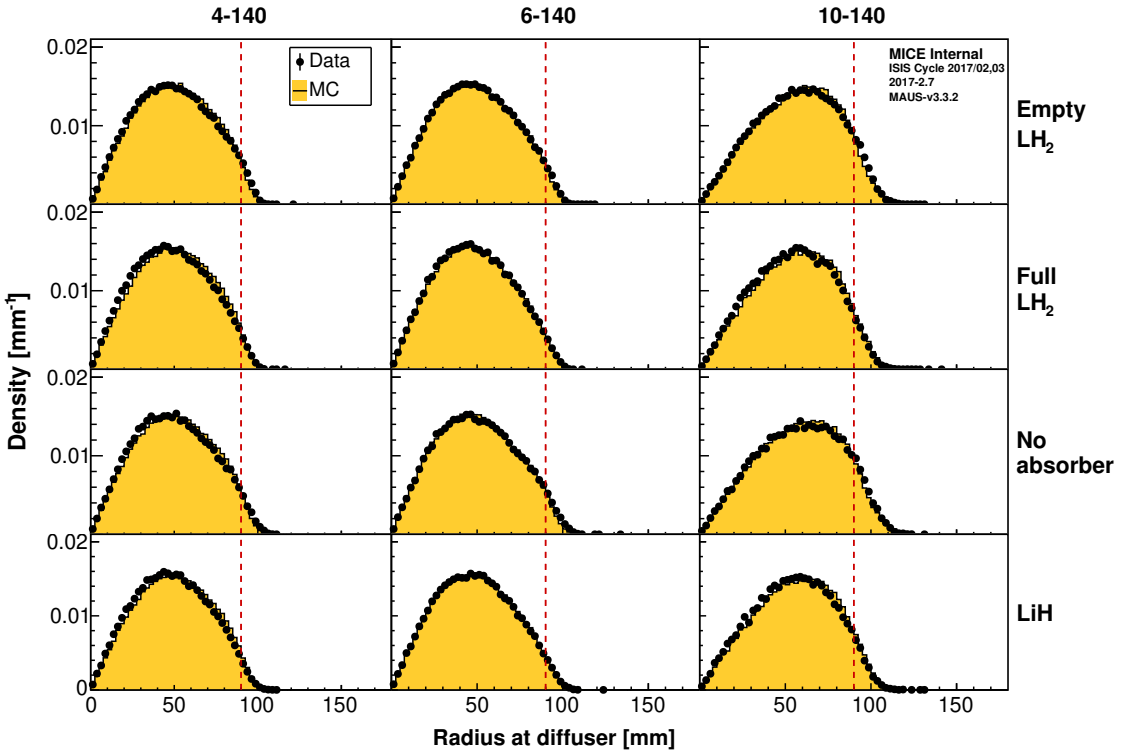

Figure 4.13: Extrapolated track radius at the upstream face of the diffuser. The histograms contain events that are accepted by all cuts other than the cut under examination.

	Empty LH_2			Full LH_2		
Beam line / Cuts	4-140	6-140	10-140	4-140	6-140	10-140
None	1558389	1580647	3273185	1002948	1122415	2029117
TOF0 & TOF1 SP	1058307	1083705	2062957	726251	825903	1394541
Time-of-Flight	545216	574011	1058926	355856	416693	699664
Diffuser aperture	926279	944755	1062145	593473	667541	662982
$p_{TOF01} - p_{TKU}$	565089	577557	886331	356850	404227	326204
TKU & TKD one track	793687	750459	717045	443344	465365	385109
TKU χ^2/ndf	959200	958138	1547262	599638	655098	934034
TKU fiducial	1070879	1092214	1645045	680768	765578	1009982
TKU momentum	281792	265235	337560	174972	180689	206094
TKD χ^2/ndf	812195	767092	731624	455325	476996	391233
TKD fiducial	799959	741056	650646	456747	473961	360078
TKD momentum	609238	587928	560762	419572	440997	376530
Final sample	**158541**	**145253**	**94664**	**105649**	**110069**	**69394**
	No absorber			LiH		
Beam line / Cuts	4-140	6-140	10-140	4-140	6-140	10-140
None	849513	1706276	1416978	823307	1003485	1196506
TOF0 & TOF1 SP	588963	1180301	918762	561422	687235	762295
Time-of-Flight	305541	629680	466127	292913	368007	387005
Diffuser aperture	502624	1009810	458408	489796	596886	385558
$p_{TOF01} - p_{TKU}$	317935	637094	393954	301475	367630	326204
TKU & TKD one track	440824	831763	323332	377188	437833	232318
TKU χ^2/ndf	520220	1035012	668173	507827	611884	566353
TKU fiducial	579524	1173327	707571	564313	692848	598516
TKU momentum	153619	288325	145704	149752	167840	122513
TKD χ^2/ndf	451130	850824	330684	382776	443743	234735
TKD fiducial	443887	817316	291095	382680	436876	214129
TKD momentum	341707	654308	254644	353671	411374	224698
Final sample	**89781**	**158786**	**42173**	**84971**	**92431**	**36346**

Table 4.4: The event selection summary for the four absorber configurations and three beam line settings in the 2017-02.7 cooling channel setting. The leftmost column contains the cuts applied to the data and the numbers corresponding to each cut represent the number of events that survive only that cut. The size of the final samples is represented in bold.

4.3.4 Beam Phase Space

The distributions of x, y, p_x, p_y and p_z reconstructed at the upstream and downstream tracker reference planes are shown in figures 4.14-4.18. In identical fashion to the figures showing the effect of the cuts, histograms are shown for each beam line setting and the corresponding four absorber configurations. The data are represented by the black solid circles, while the MC simulation is shown in yellow fill. The comparison reveals good agreement, as the simulation provides an accurate description of the beam spatial extent and momentum. The data-simulation agreement on the reconstructed longitudinal momentum in the downstream tracker indicates the energy loss at the absorber is well understood. Small discrepancies observed for some beams may occur due to simulated misalignments of the magnets. Nonetheless, these discrepancies are not expected to affect the emittance measurement comparison, as the underlying beam covariance matrix is computed with respect to the distribution mean.

The 2-dimensional projections on the transverse position (x, y) and transverse momentum (p_x, p_y) subspaces are shown in figures 4.19-4.22. The beams are well centred in both subspaces.

4.3.5 Beam Optics

Once the beam covariance matrix is computed, the bulk properties of the beam can be estimated. The evolution of the transverse Twiss parameters $\alpha_\perp$ and $\beta_\perp$ through the cooling channel is shown in figure 4.23. The reconstructed data, shown in magenta solid circles, are well reproduced by both the reconstructed simulation (cyan solid squares) and truth (dark cyan rhombi and line) at the tracker stations. The truth simulation is further evaluated at virtual planes coarsely distributed in the region between the two trackers, with the values joined by straight lines to provide an insight into the evolution near and at the absorber. The location of the absorber is indicated by the vertical blue line and each tracker station position is shown by a vertical green line. The horizontal axis indicates the position along the beam line, in the global coordinates of the experiment.

The parameter $\alpha_\perp$, defined in equation 2.37, gives the average correlation in the (x, p_x) and (y, p_y) subspaces, and is proportional to the rate of change of the betatron function with respect to z. Hence, its evolution along the channel gives a preview

for the observed oscillatory behaviour of $\beta_\perp$. While a constant betatron function in TKU was desired to reduce its value at the absorber and to avoid emittance growth due to non-linear effects, it is oscillating significantly. The effect is stronger with decreasing input emittance. It occurs as the triplet of quadrupole magnets Q7-9 did not provide adequate focusing to produce a beam with ($\alpha_\perp$, $\beta_\perp$) values matching the requirements of the upstream solenoid spectrometer.

The oscillation in TKU leads to a larger, suboptimal, $\beta_\perp$ value at the absorber, hindering the measured cooling performance proportionately, as seen in equations 2.52 and 2.53. The solution proposed to mitigate this effect and maximize cooling is discussed in section 4.4. Downstream of the absorber module, $\beta_\perp$ is larger due to the absence of the M1D coil, which makes the beam susceptible to optical emittance growth. Momentum loss at the absorber enhances the focusing strength downstream of it, which results in a slightly lower beta function with a more prominent waist, by comparison with the no absorber cases.

4.3.6 Emittance

The evolution of the normalized transverse emittance $\epsilon_\perp$ through the cooling channel is shown in figure 4.24. The reconstructed data are well reproduced by the simulation, both truth and reconstructed. The truth simulation is further evaluated at virtual planes coarsely distributed in the region between the two trackers, with the values joined by straight lines to gain an insight into the evolution near and at the absorber. For the 6-140 beam line configuration, there is an apparent discrepancy in input emittance in TKU that carries throughout the channel, indicating the evolution is still well understood. This may occur due to a mismodelling of the beam line components or the diffuser. It must be noted that at this stage, no corrections for systematic biases and no systematic uncertainties are included in the figures.

In the scenarios with an absorber in the path of the beam, a reduction in emittance, i.e., cooling, is observed for the 6-140 and 10-140 beams. This is in contrast with the control cases where no reduction occurs. The effect is larger with increasing input emittance, as expected from equation 2.52. The reduction is more abrupt for the lithium hydride absorber than the liquid hydrogen due to its larger stopping power. Mild optical emittance growth is observed in the region between the absorber module and TKD for some of the beams. The effect is predominantly caused by chromatic aberrations and it is enhanced at locations where the beam has a higher

beta function. For the 4-140 beams, even though the truth simulation indicates a small cooling signal at the absorber, the reconstructed emittance change (data and simulation) is compatible with zero. The apparent loss of cooling signal recorded by the trackers is caused by emittance growth before and after the absorber, which is due to by the large $\beta_\perp$ oscillations. Furthermore, the cooling effect at the absorber is hindered by the large $\beta_\perp$ value at the absorber, which increases the heating due to multiple scattering.

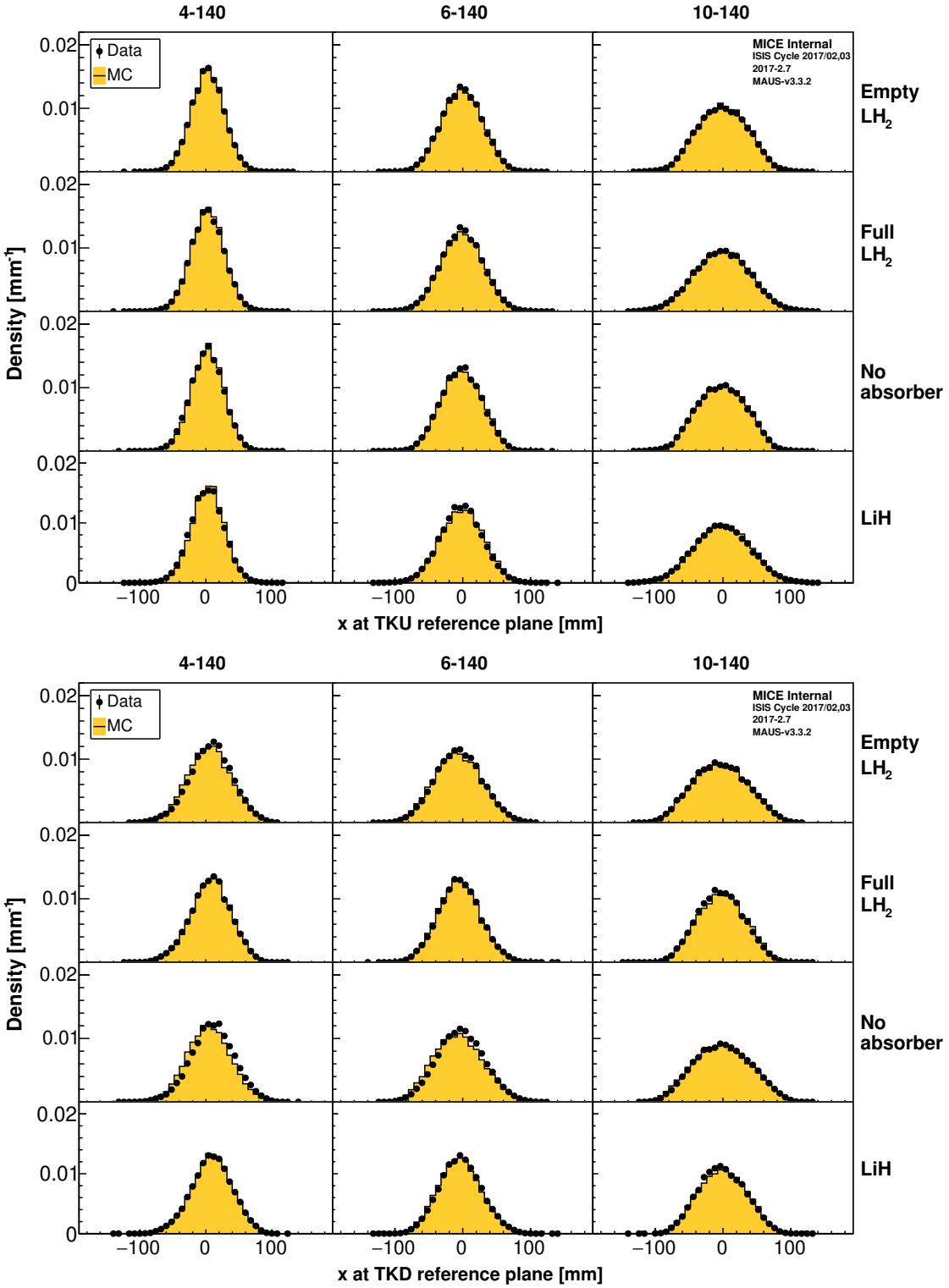

Figure 4.14: Horizontal position distribution at (top) TKU and (bottom) TKD reference planes of the events in the final sample.

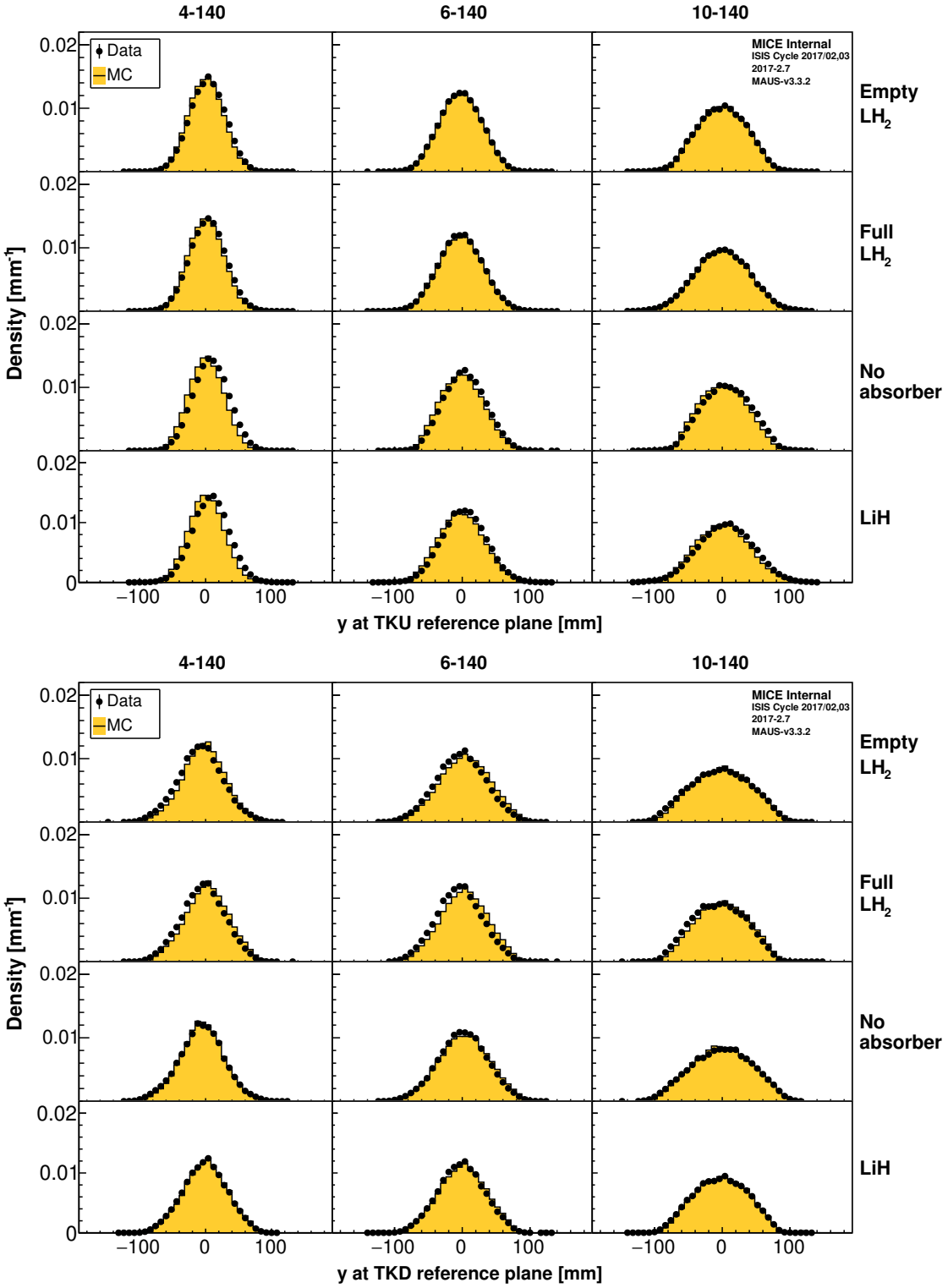

Figure 4.15: Vertical position distribution at (top) TKU and (bottom) TKD reference planes of the events in the final sample.

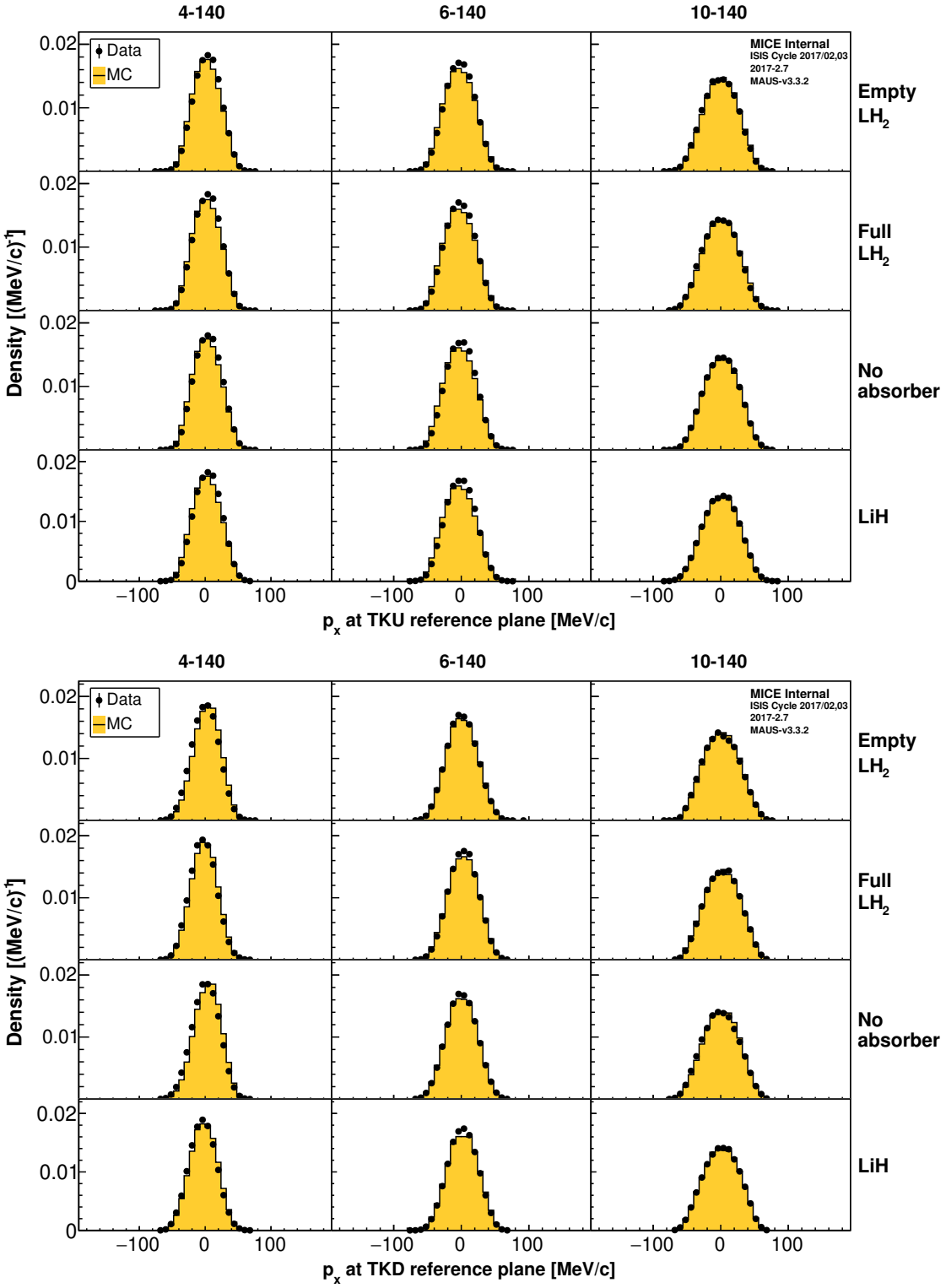

Figure 4.16: Horizontal momentum distribution at (top) TKU and (bottom) TKD reference planes of the events in the final sample.

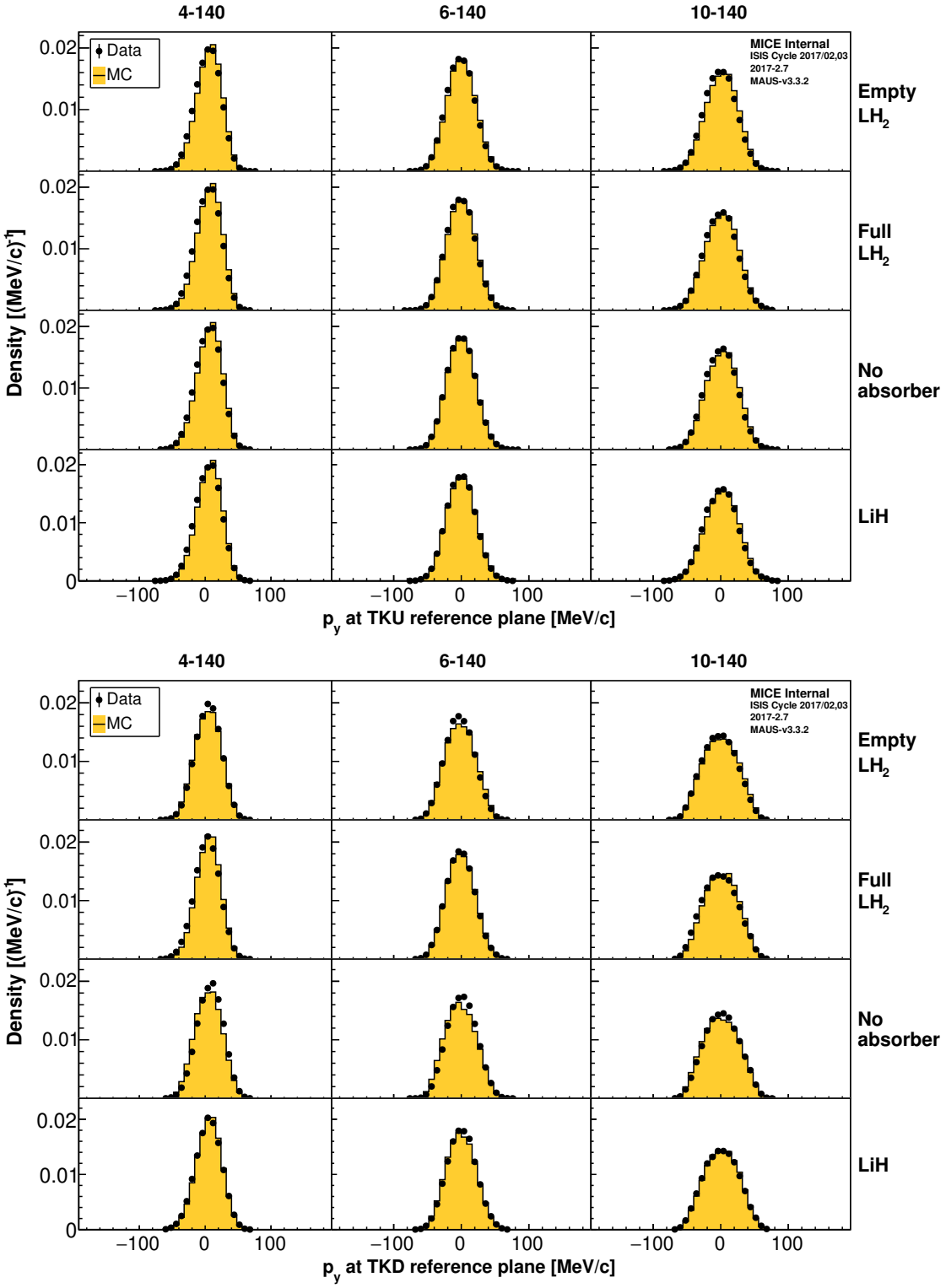

Figure 4.17: Vertical momentum distribution at (top) TKU and (bottom) TKD reference planes of the events in the final sample.

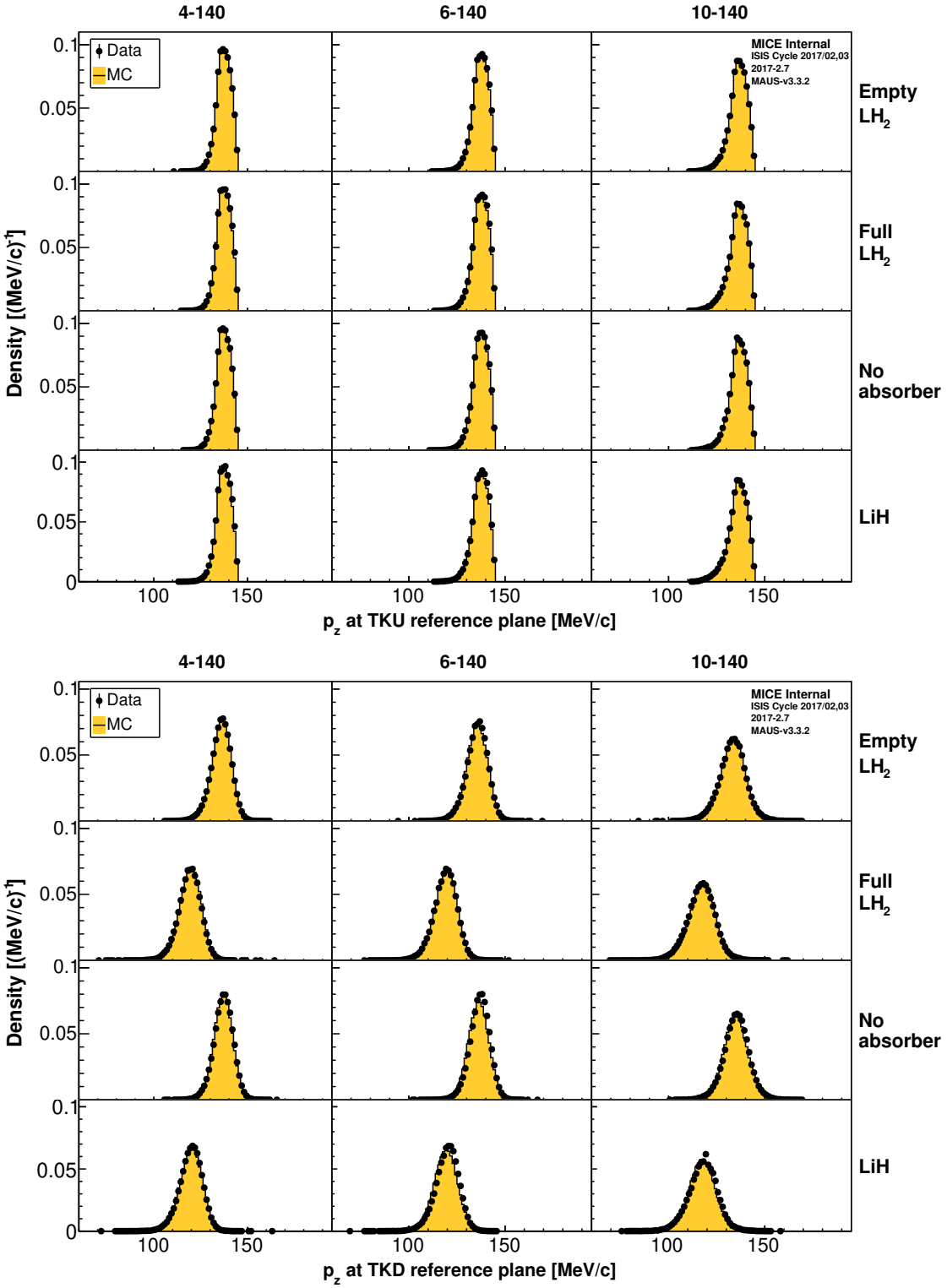

Figure 4.18: Longitudinal momentum distribution at (top) TKU and (bottom) TKD reference planes of the events in the final sample.

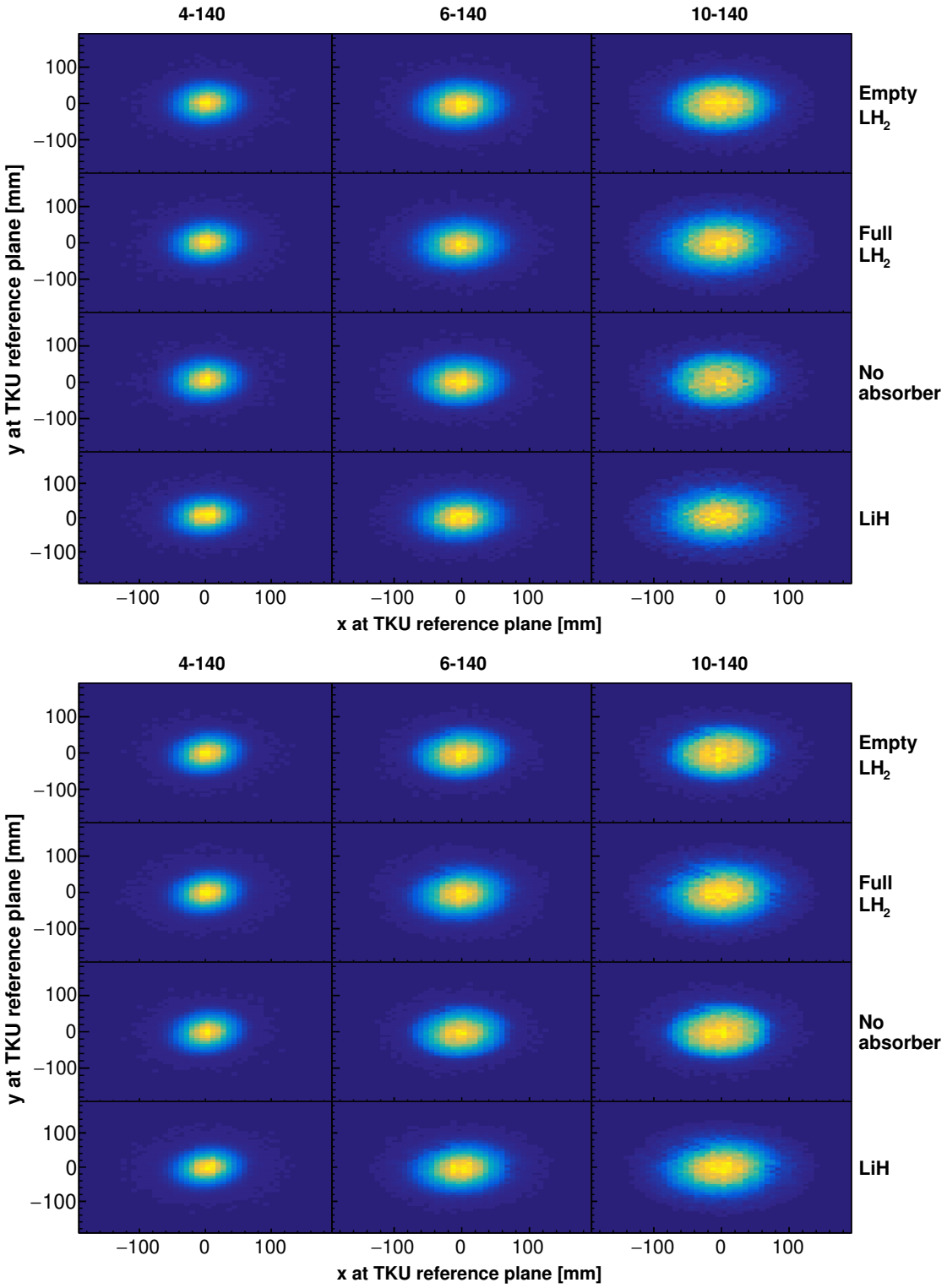

Figure 4.19: Distribution of the events in (x, y) at the TKU reference plane for (top) reconstructed data and (bottom) reconstructed simulation.

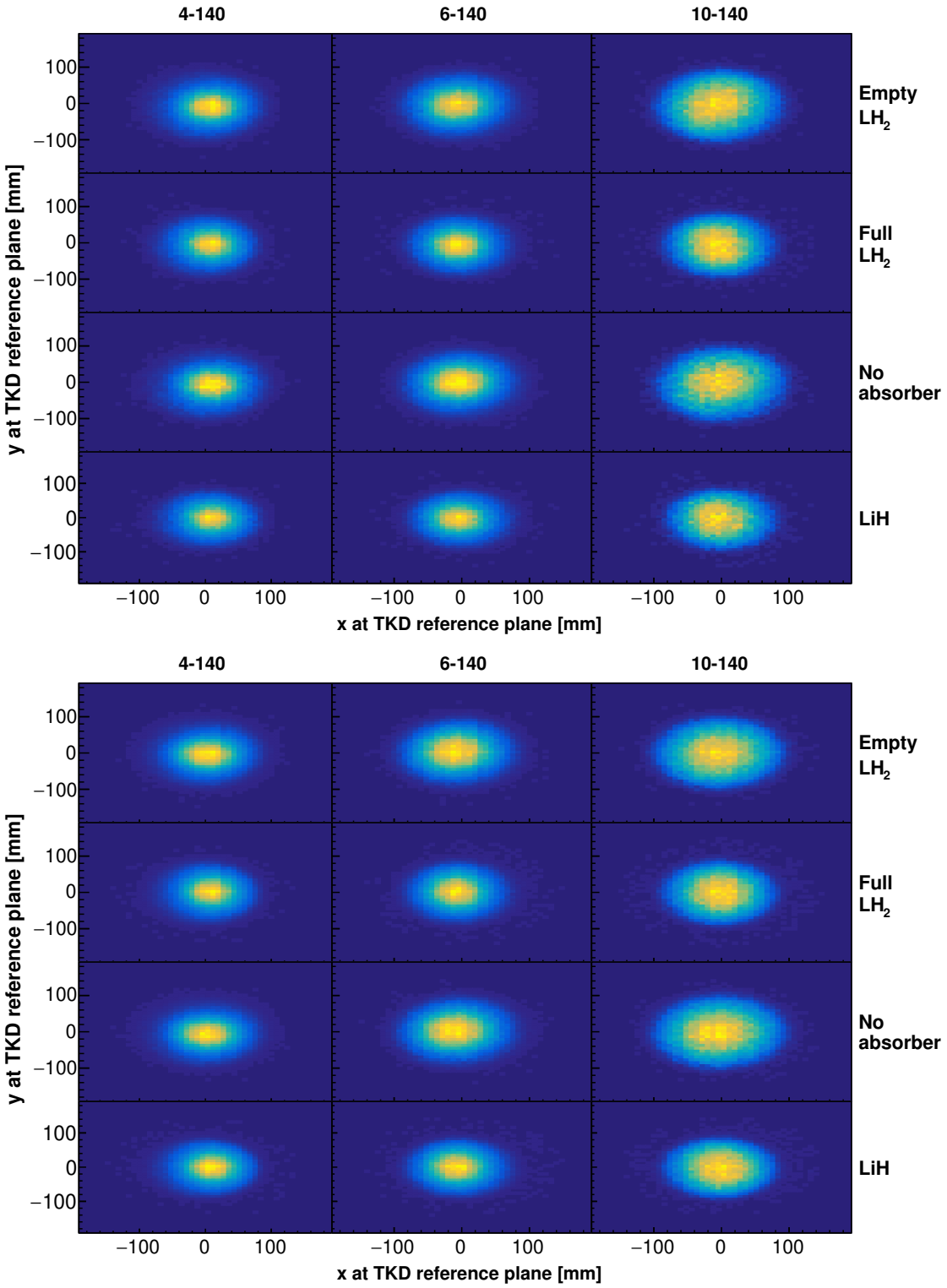

Figure 4.20: Distribution of the events in (x, y) at the TKD reference plane for (top) reconstructed data and (bottom) reconstructed simulation.

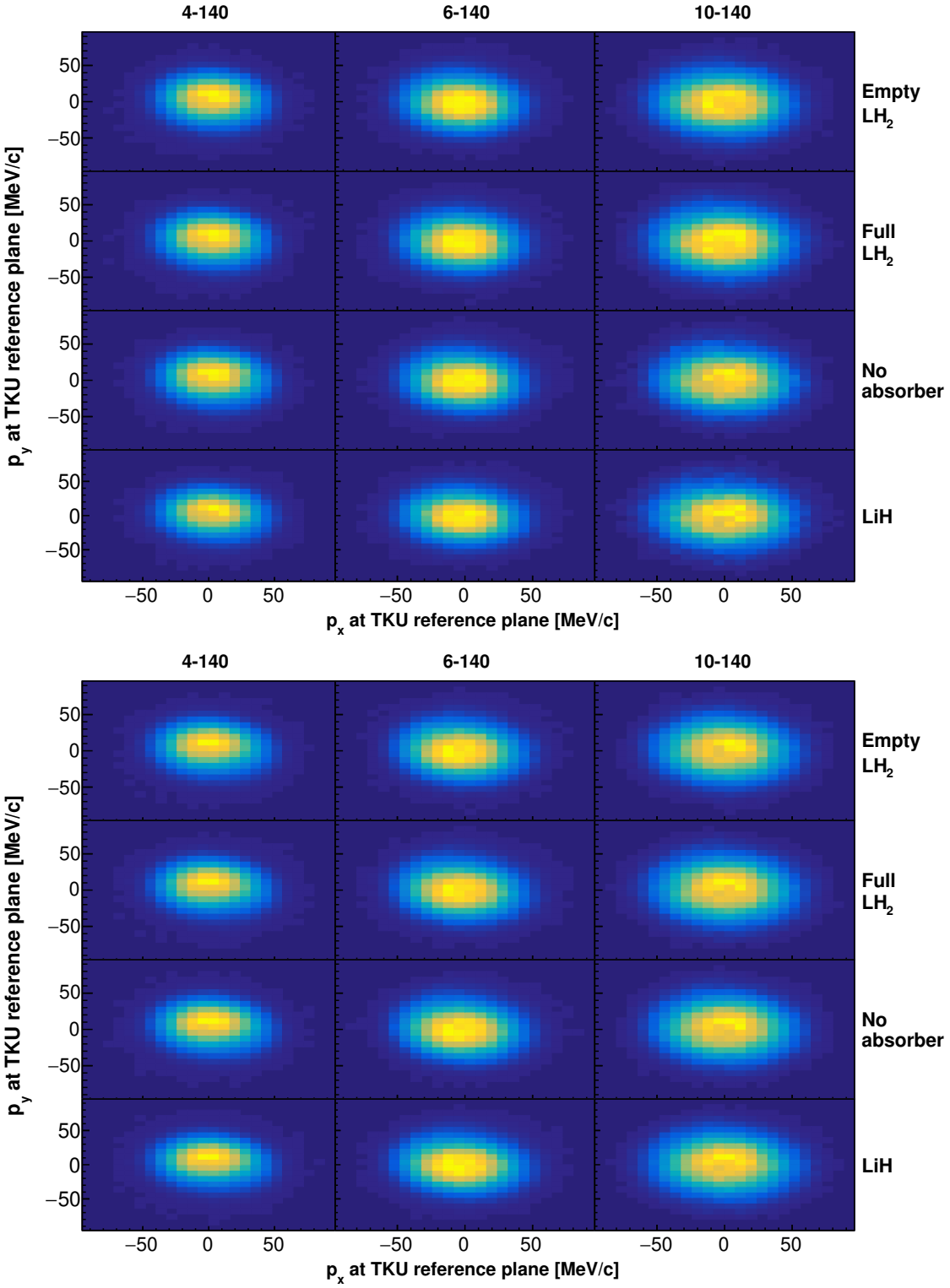

Figure 4.21: Distribution of the events in (p_x, p_y) at the TKU reference plane for (top) reconstructed data and (bottom) reconstructed simulation.

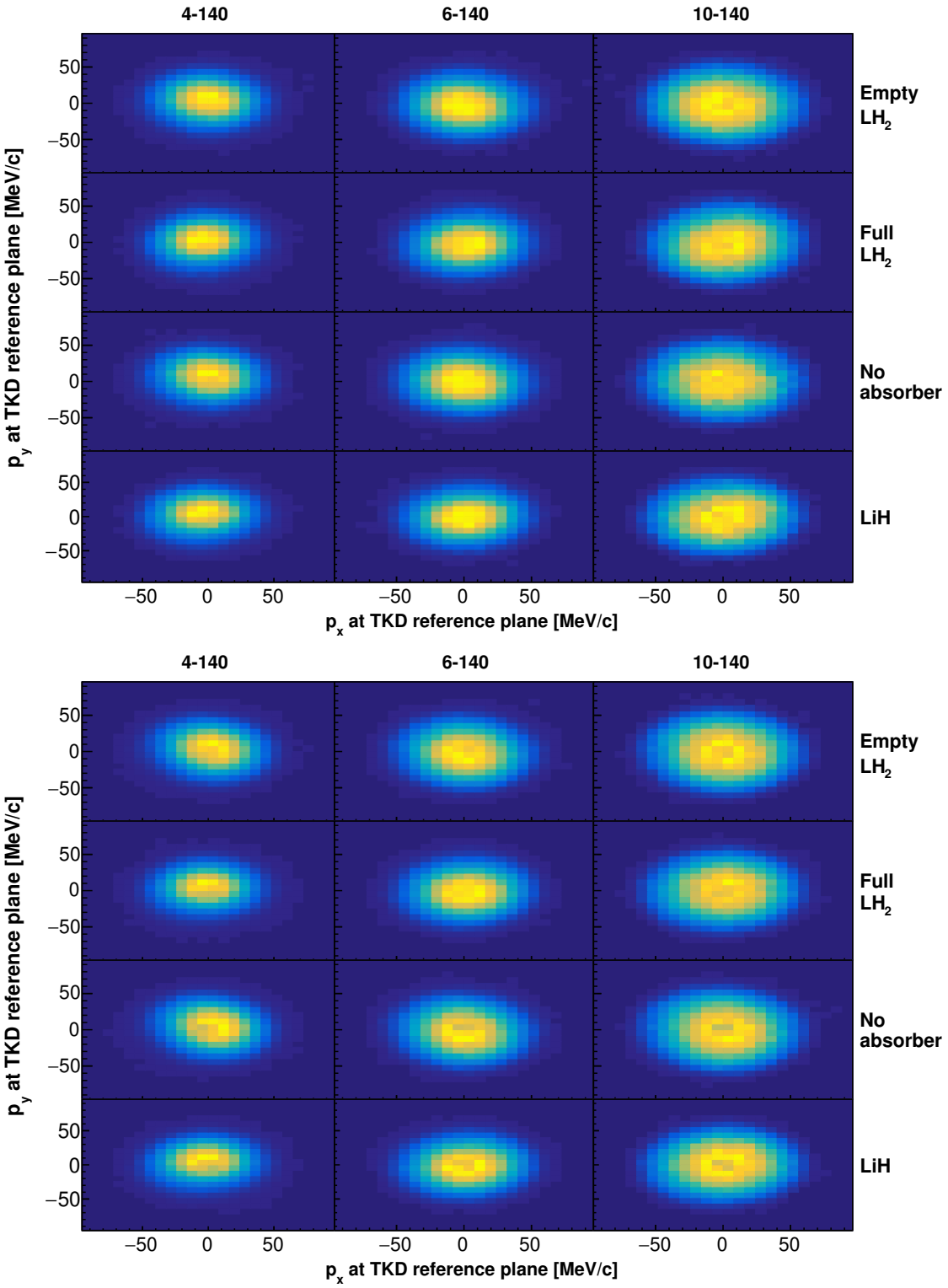

Figure 4.22: Distribution of the events in (p_x, p_y) at the TKU reference plane for (top) reconstructed data and (bottom) reconstructed simulation.

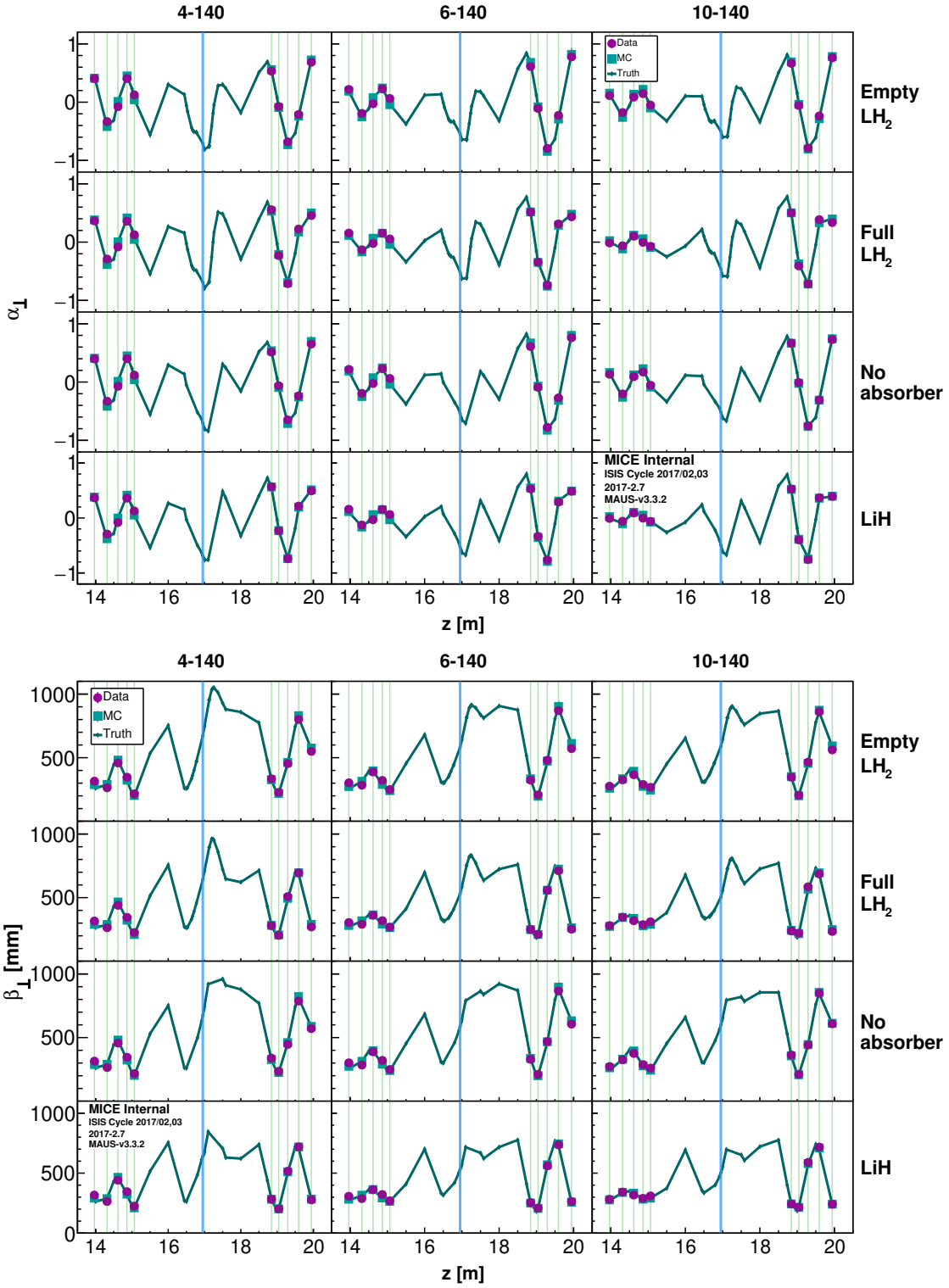

Figure 4.23: Evolution of the transverse Twiss parameters (top) $\alpha_\perp$ and (bottom) $\beta_\perp$ through the cooling channel. The vertical blue line represents the central position of the absorber, while the vertical green lines indicate the position of the five stations in each tracker.

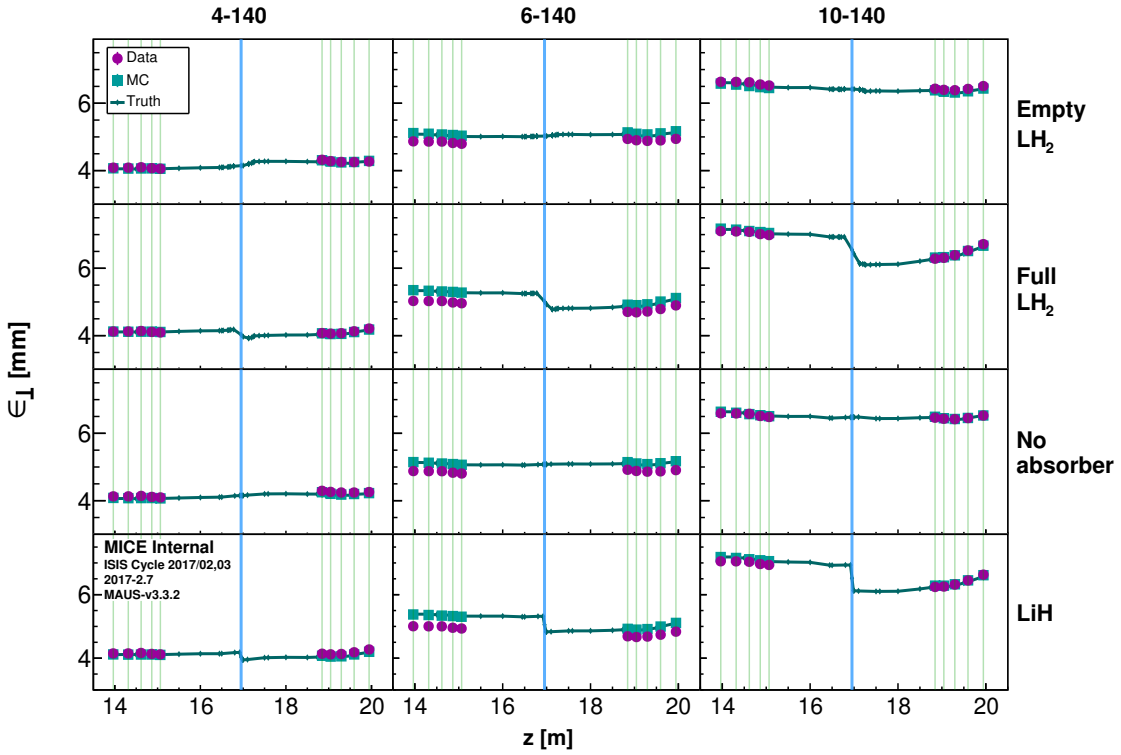

Figure 4.24: Evolution of the transverse emittance $\epsilon_\perp$ through the cooling channel. The vertical blue line represents the central position of the absorber, while the vertical green lines indicate the position of the five stations in each tracker.

4.4 Beam Matching

The beam optics studies conducted after the failure of the M1D coil sought to minimise $\beta_\perp$ at the absorber while achieving a reasonable transmission to the downstream tracker. The final solution proposed a matched betatron function in the upstream tracker region, i.e., $\beta_\perp = \text{const.}$ and $\alpha_\perp = 0$ throughout. For the solution to work, the incoming beams were required to fulfill the following matching conditions at the tracker entrance: $\beta'_\perp = 0$, $\beta''_\perp = 0$ and, by substituting these two conditions into the envelope equation 2.36 and assuming zero mean canonical angular momentum, $\beta_\perp = 1/\kappa$. For 140 MeV/c beams in a 3 T field, $\beta_\perp \approx 311$ mm.

Nonetheless, the beta function is not properly matched into TKU due to inadequate focusing by the Q7-9 triplet of quadrupole magnets, as seen in figure 4.23. The oscillations in TKU translate into a $\beta_\perp$ value at the absorber larger than initially designed. As discussed in section 2.7, for a given beam momentum and absorber material choice, the measured cooling performance can be improved only by reducing $\beta_\perp$ at the absorber. For the data sets presented here, the beta function, and hence the measured cooling performance, are sub-optimal, and present an opportunity for improvement.

MICE possesses the novel capability to measure muon beams particle-by-particle. This feature makes it possible to select beam subsamples with specific bulk properties, such as emittance or Twiss parameters. A beam selection algorithm based on rejection sampling is developed to sample beams with a range of input emittances and constant betatron function in the upstream tracker, improving the beam optics properties, and thus the cooling performance measurement.

4.4.1 Sampling Procedure

The selection procedure developed to obtain beams matched to the upstream tracker is based on a rejection sampling algorithm [87][88]. Rejection sampling is generally used to generate samples of a random variable from a complicated target probability density function that makes direct sampling impossible or impractical. Samples are drawn from a well-defined distribution, such as the normal distribution, and are subjected to a rejection criterion such that the accepted samples seem to follow the target distribution.

The task of the custom algorithm in this analysis is to carve out a subsample

that follows a 4D Gaussian distribution described by a specific (target) covariance matrix from an input beam ensemble. To this end, the probability density function underlying the beam ensemble must also be known. Since the beam is only approximately Gaussian, the kernel density estimation (KDE) technique is used to evaluate its density in a non-parametric fashion [89][90].

In KDE, each data point is assigned a smooth weight function, also known as kernel, and the contributions from all data points in the data set are summed. The multivariate kernel density estimator at an arbitrary point $\mathbf{u}$ in the d-dimensional space is given by

$$\hat{f}(\mathbf{u}) = \frac{1}{nh^d} \sum_{i=1}^{n} K\left(\frac{\mathbf{u} - \mathbf{U_i}}{h}\right), \tag{4.5}$$

where K is the kernel, n is the sample size, h is the width of the kernel, also referred to as bandwidth, and $\mathbf{U_i}$ represents the coordinate of the i-th data point in the sample. In this analysis, Gaussian kernels of the following form are used

$$K\left(\frac{\mathbf{u} - \mathbf{U_i}}{h}\right) = \frac{1}{\sqrt{(2\pi)^d |\mathbf{\Sigma}|}} \exp\left[-\frac{1}{2}\frac{(\mathbf{u} - \mathbf{U_i})^T \mathbf{\Sigma}^{-1} (\mathbf{u} - \mathbf{U_i})}{h^2}\right], \tag{4.6}$$

where $\mathbf{\Sigma}$ is the covariance matrix of the data set. The width of the kernel is chosen to minimise the mean squared integrated error (MISE), which gives a measure of the accuracy of the estimator [91]. Scott's rule of thumb is followed in this work, wherein the bandwidth is determined from the sample size n and number of dimensions d through $h = n^{-1/(d+4)}$ [90].

The KDE form described in equations 4.5 and 4.6 is used to estimate the 4D transverse phase space density of the initial, unmatched beams presented in section 4.3.3. As these are the beams we are sampling from, they are also referred to as parent beams (distributions), with the estimated underlying density denoted by $Parent(\mathbf{u})$. The target distribution, $Target(\mathbf{u})$, is a 4D Gaussian defined through the covariance matrix presented in equation 2.33. The matrix is parameterised through the transverse emittance ($\epsilon_\perp$), the Twiss functions ($\alpha_\perp$, $\beta_\perp$), the longitudinal momentum (p_z), and the kinetic angular momentum term ($\beta_\perp \kappa - \mathcal{L}) \approx -\langle L_{kin} \rangle / 2$.

The sampling is performed at the upstream tracker reference plane. For each particle in the parent beam, with 4D phase space vector $\mathbf{u_i}$, the selection algorithm works as follows:

1. Compute the selection probability as

$$P_{select}(\mathbf{u}_\mathrm{i}) = \mathcal{C} \times Target(\mathbf{u}_\mathrm{i})/Parent(\mathbf{u}_\mathrm{i}), \tag{4.7}$$

   where the normalisation constant $\mathcal{C}$ ensures that $P_{select}(\mathbf{u}_\mathrm{i}) \leq 1$.

2. Generate ξ_i from the uniform distribution $\mathcal{U}([0, 1])$.

3. If $P_{select}(\mathbf{u}_\mathrm{i}) > \xi_i$, then accept the particle. Otherwise, reject it.

The normalisation constant $\mathcal{C}$ is calculated prior to the selection iteration presented in the steps 1-3. It requires an iteration through the parent ensemble (of size n) and it is calculated as

$$\mathcal{C} = \min_{i \in \{1,\ldots,n\}} \frac{Parent(\mathbf{u}_\mathrm{i})}{Target(\mathbf{u}_\mathrm{i})}, \tag{4.8}$$

Figure 4.25 shows the algorithm at work by comparing the betatron function of a simulated 4 mm parent beam with the one of a subsample with matched optics in the upstream tracker. Both simulation truth and reconstructed simulation are shown. The truth is calculated on a fine grid in between the trackers for a detailed observation of the $\beta_\perp$ evolution. The parent beam reconstructed Twiss parameters ($\alpha_\perp$, $\beta_\perp$) at the TKU reference plane are (0.12, 222 mm), and the corresponding sampling target values are (0, 311 mm). The remaining parameters required to define the target distribution are set with the corresponding values of the parent beam. The sampling routine performs well, as $\beta_\perp$ of the subsample is approximately constant in the upstream tracker, which results in a $\beta_\perp$ reduction at the position of the absorber centre of $\sim 28\%$. Additionally, changes further downstream occur. The double peak between the absorber and the downstream tracker changes shape and amplitude and the oscillation amplitude in TKD is slightly increased.

4.4.2 Matched Samples

In order to study the linear dependence of the cooling effect on input emittance, including the effective equilibrium emittance, six beams with ($\alpha_\perp$, $\beta_\perp$) = (0, 311 mm) and emittances of 1.5, 2.5, 3.5, 4.5, 5.5 and 6.5 mm at the TKU reference plane are sampled for each absorber setting. To achieve this, each parent ensemble is split

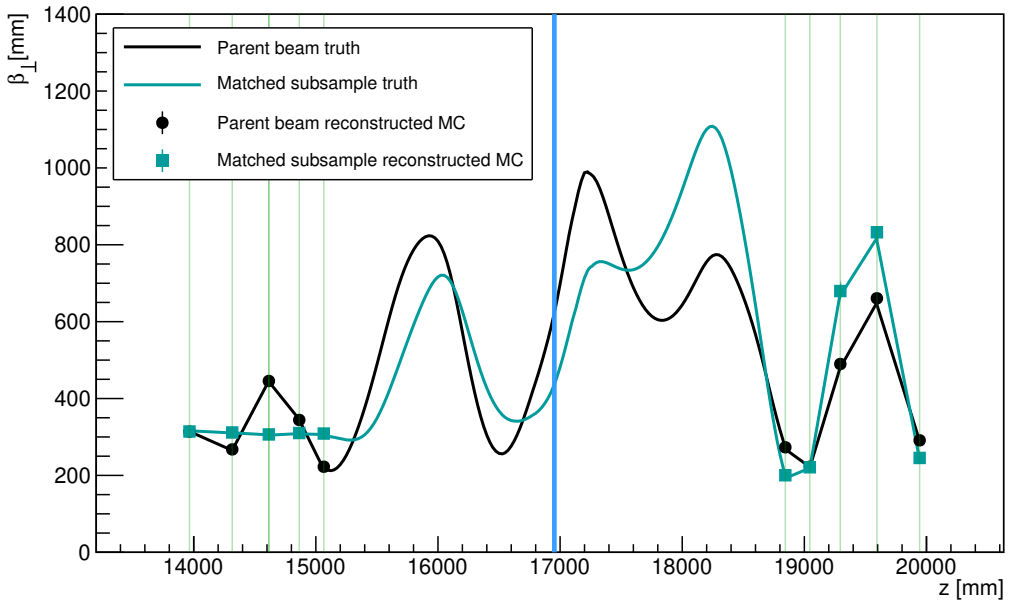

Figure 4.25: Evolution of the transverse betatron function, $\beta_\perp$, through the cooling channel containing the full liquid hydrogen vessel for the (black) parent beam and the (dark cyan) matched subsample. The corresponding lines represent the simulation truth, while the circles and squares at the (green vertical lines) tracker stations represent the reconstructed simulation. The vertical blue line marks the central position of the absorber.

into two ensembles that are subsequently subjected to the sampling procedure, as follows:

- Two beams with target emittances of 1.5 and 2.5 mm are sampled from the 4-140 parent beam.
- Two beams with target emittances of 3.5 and 4.5 mm are sampled from the 6-140 parent beam.
- Two beams with target emittances of 5.5 and 6.5 mm are sampled from the 10-140 parent beam.

The sample sizes of the selected beams are shown in table 4.5. The relatively lower sample sizes for the 1.5 and 2.5 mm beams are caused by lower sampling efficiency, which mainly arises from the volume ratio between the 4D hyperellipsoids of the parent and target distributions. From equation 2.29, the ratio can be calculated

as

$$\frac{V_{\perp}^{T}}{V_{\perp}^{P}} = \left(\frac{\epsilon_{\perp}^{T}}{\epsilon_{\perp}^{P}}\right)^{2}, \tag{4.9}$$

where the P and T superscripts stand for the parent and target, respectively. The target-to-parent emittance ratio is lower for the 1.5 and 2.5 mm beams. Another factor that contributes to the variation in the sample sizes is the variation in the sample sizes of the parent beams. This is most notable for the 'LiH' and 'No absorber' 5.5 and 6.5 mm beams, as the corresponding 10-140 parent data sets have relatively low sample sizes (see table 4.4).

Absorber \ Input $\epsilon_{\perp}$ [mm]	1.5	2.5	3.5	4.5	5.5	6.5
Empty LH_2	8141	10162	19525	29896	13196	22080
Full LH_2	5199	8541	16757	20836	9063	15326
No absorber	4496	4792	32836	17659	5324	8573
LiH	4549	4372	9150	21071	3927	7618

Table 4.5: The size of the sampled matched beams.

Upstream Tracker Phase Space

The 1D phase space projections at the TKU reference plane are shown in figures 4.26-4.30. The individual beam distributions are grouped in two 4×3 panels. Each panel column corresponds to a target emittance and each row to an absorber setting. Excellent data-simulation agreement is observed. The discrepancies noted in the parent beam profiles (see figures 4.14-4.17) are reduced as the selection procedure is tasked to output identical, centred beams both in data and simulations. The RMS of the four transverse variables increases with the emittance, as expected. The 2D projections on (x, y) and (p_x, p_y) are presented in figures B.1-B.4.

Downstream Tracker Phase Space

The 1D phase space projections at the TKD reference plane are shown in figures 4.31-4.35. The data are well reproduced by simulation. The small discrepancies observed predominantly in the x and y projections occur due to simulated misalignments of the magnets situated in between the two trackers. The 2D projections on (x, y) and (p_x, p_y) are presented in figures B.5-B.8.

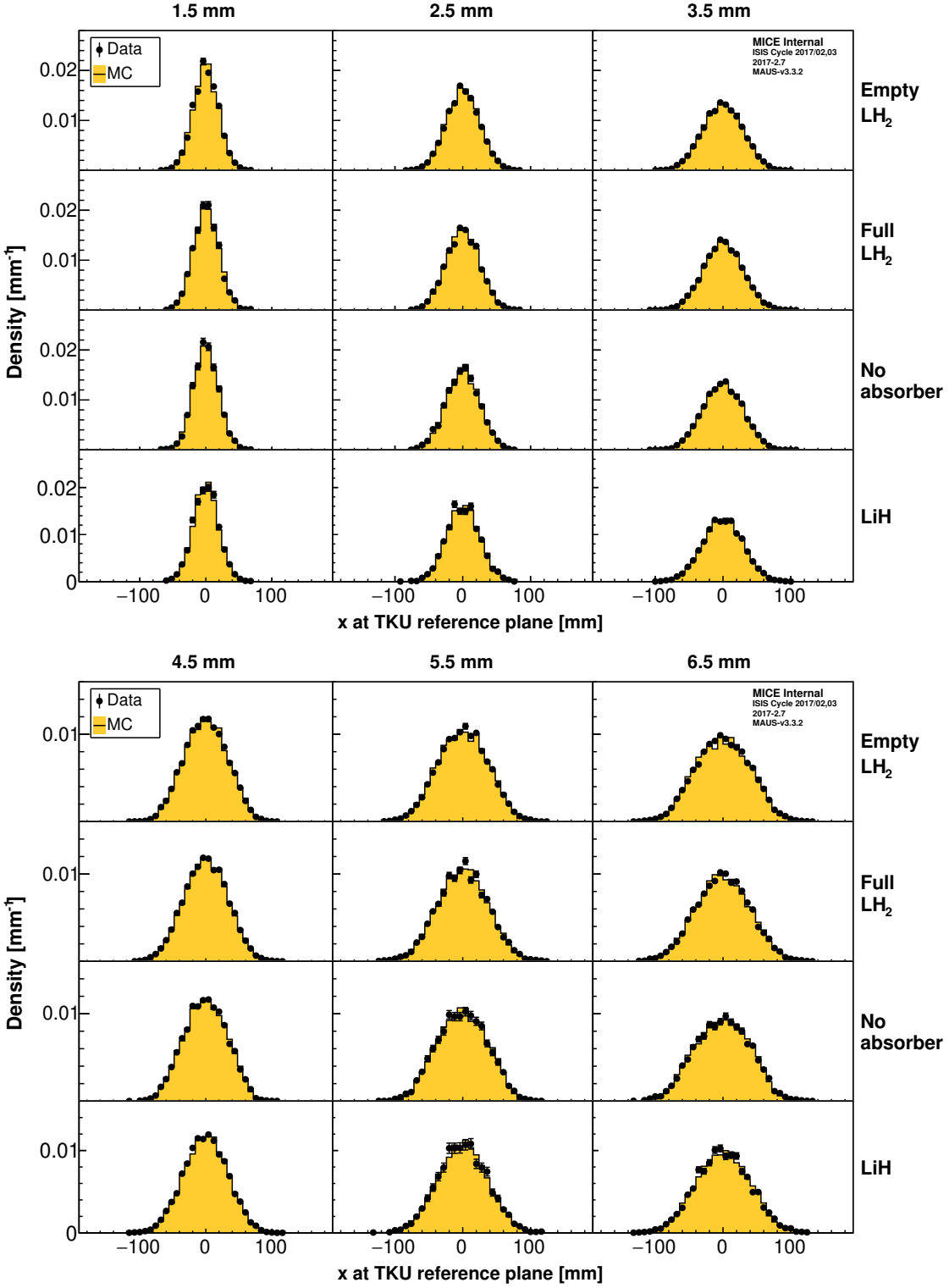

Figure 4.26: Horizontal position distribution at TKU reference plane for the six matched beams.

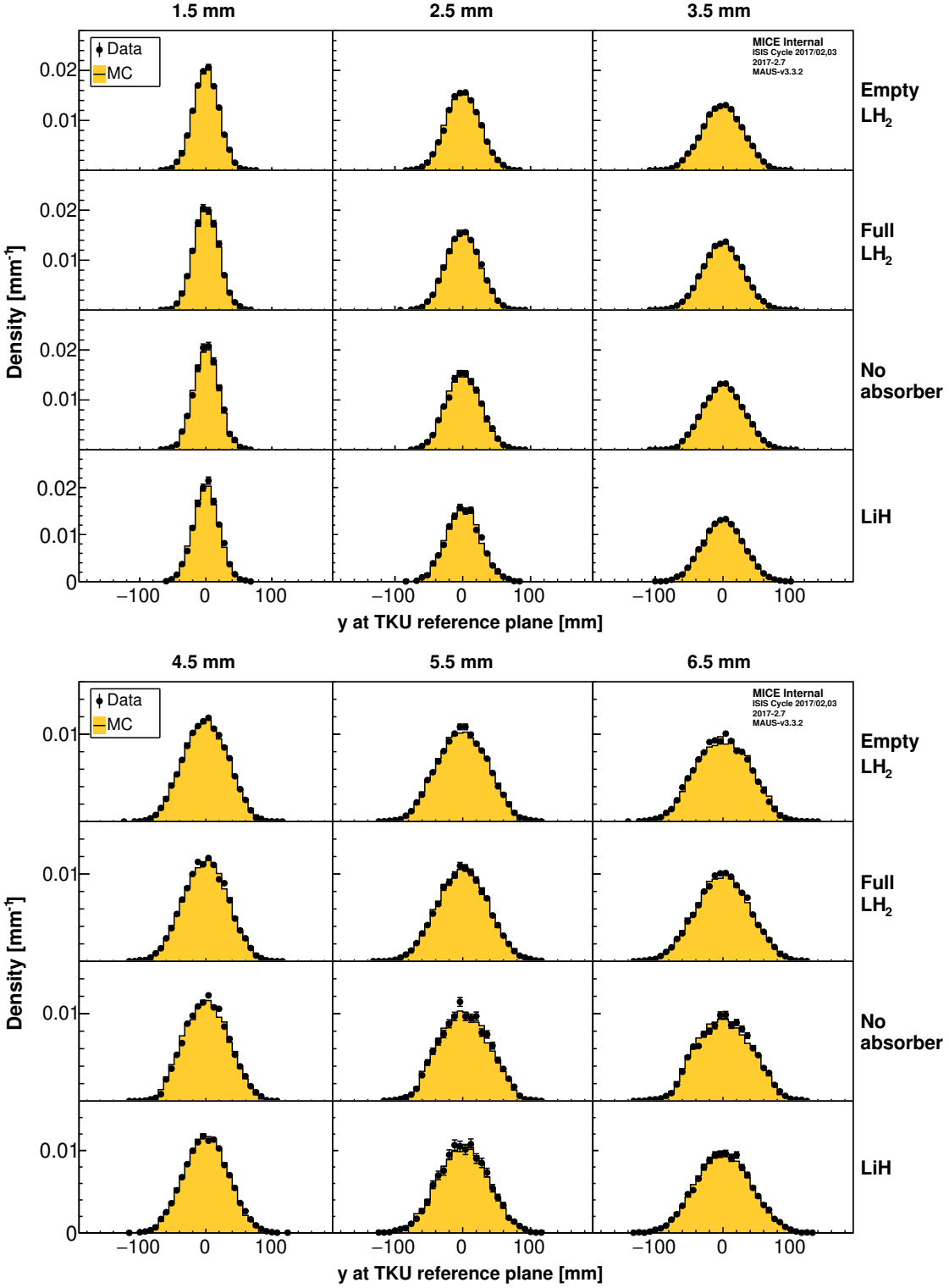

Figure 4.27: Vertical position distribution at TKU reference plane for the six matched beams.

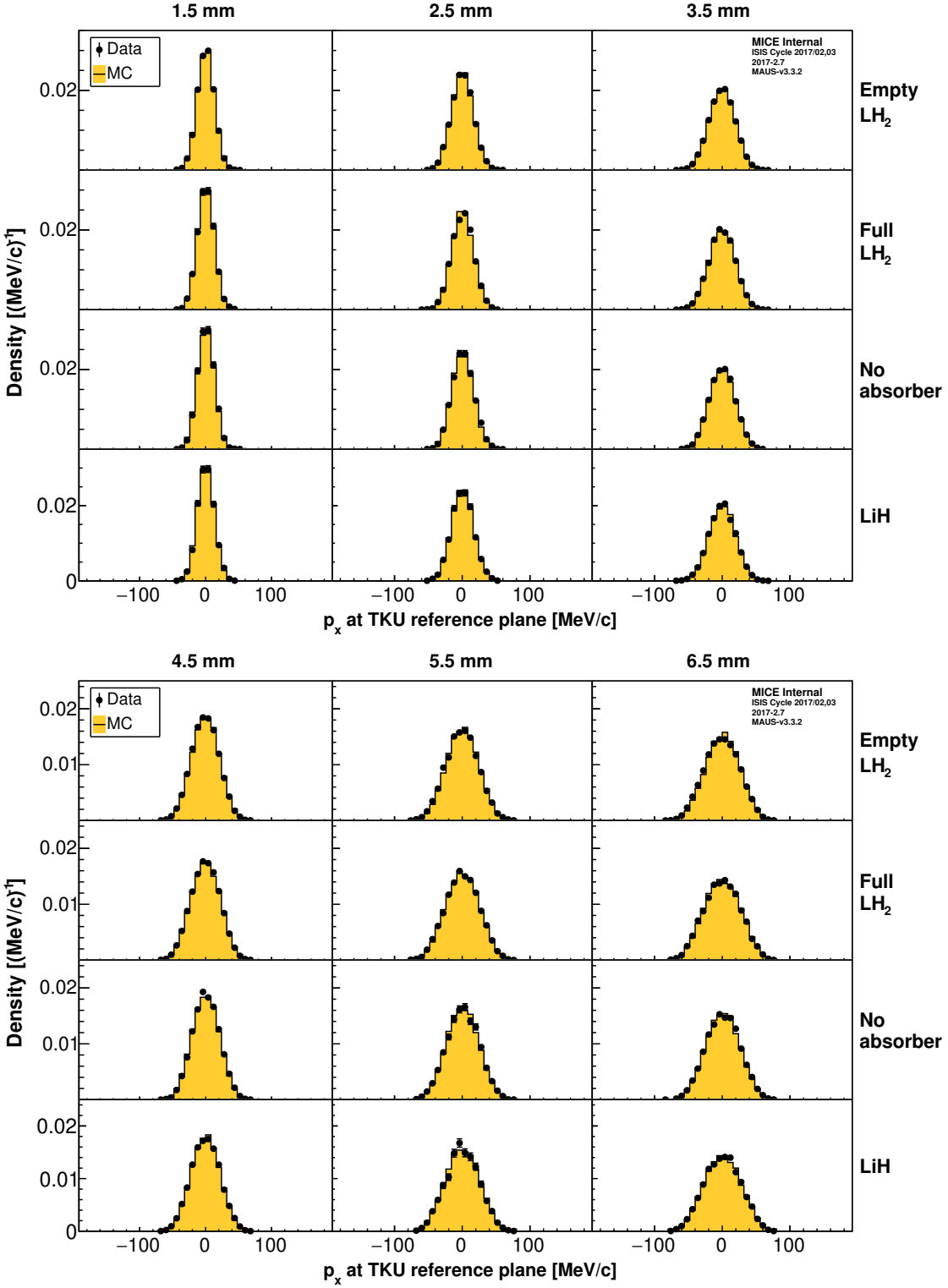

Figure 4.28: Horizontal momentum distribution at TKU reference plane for the six matched beams.

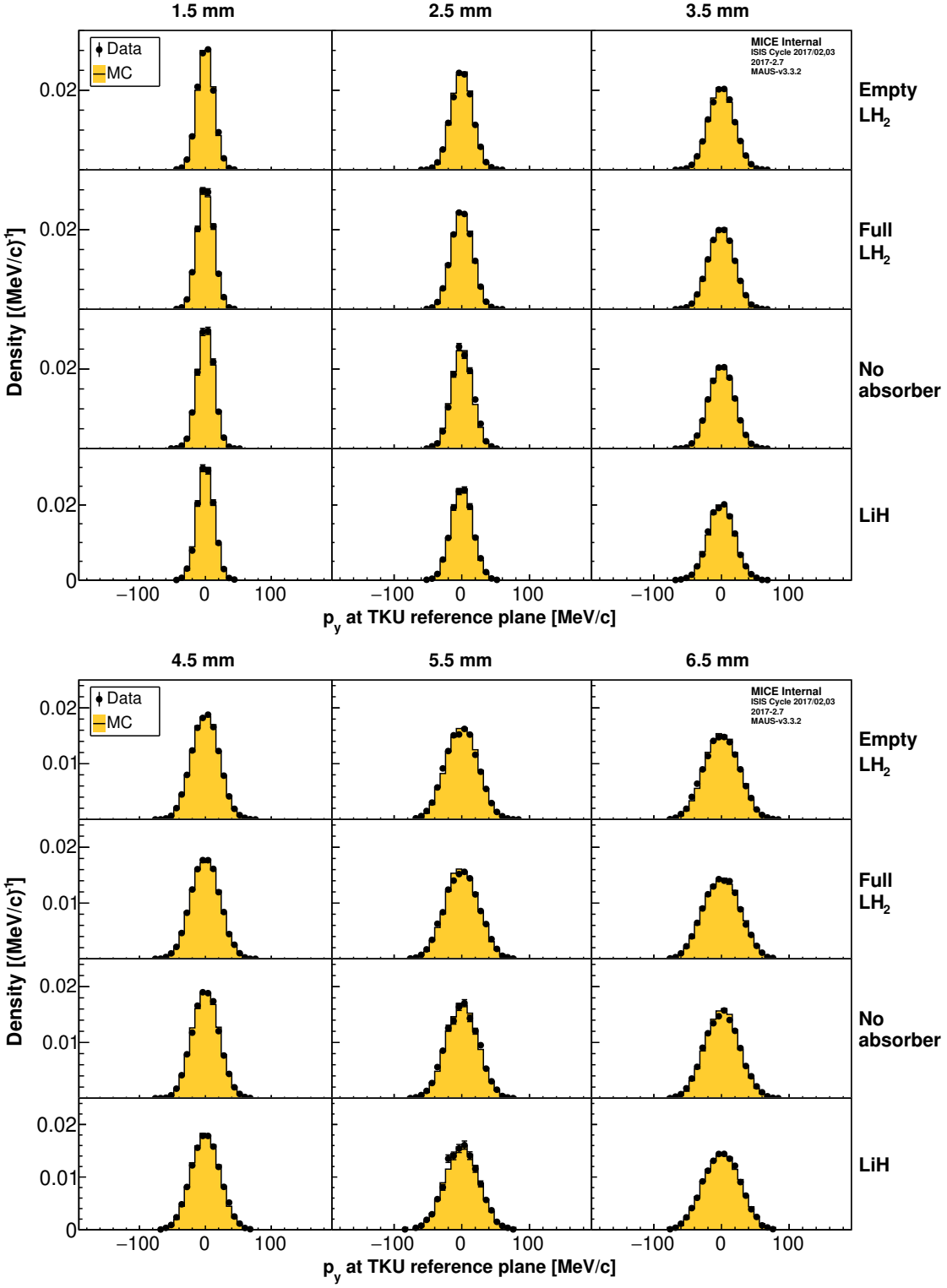

Figure 4.29: Vertical momentum distribution at TKU reference plane for the six matched beams.

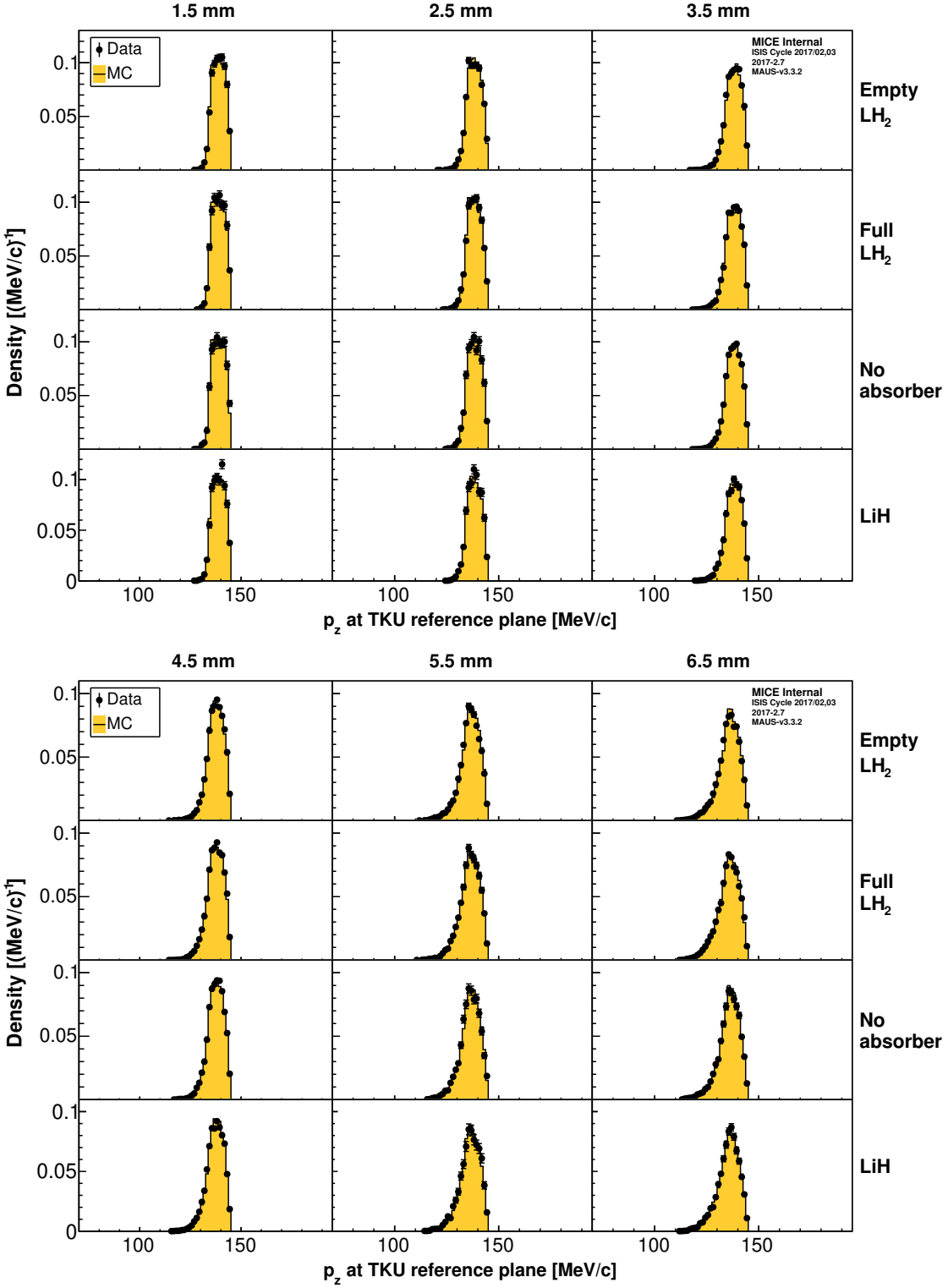

Figure 4.30: Longitudinal momentum distribution at TKU reference plane for the six matched beams.

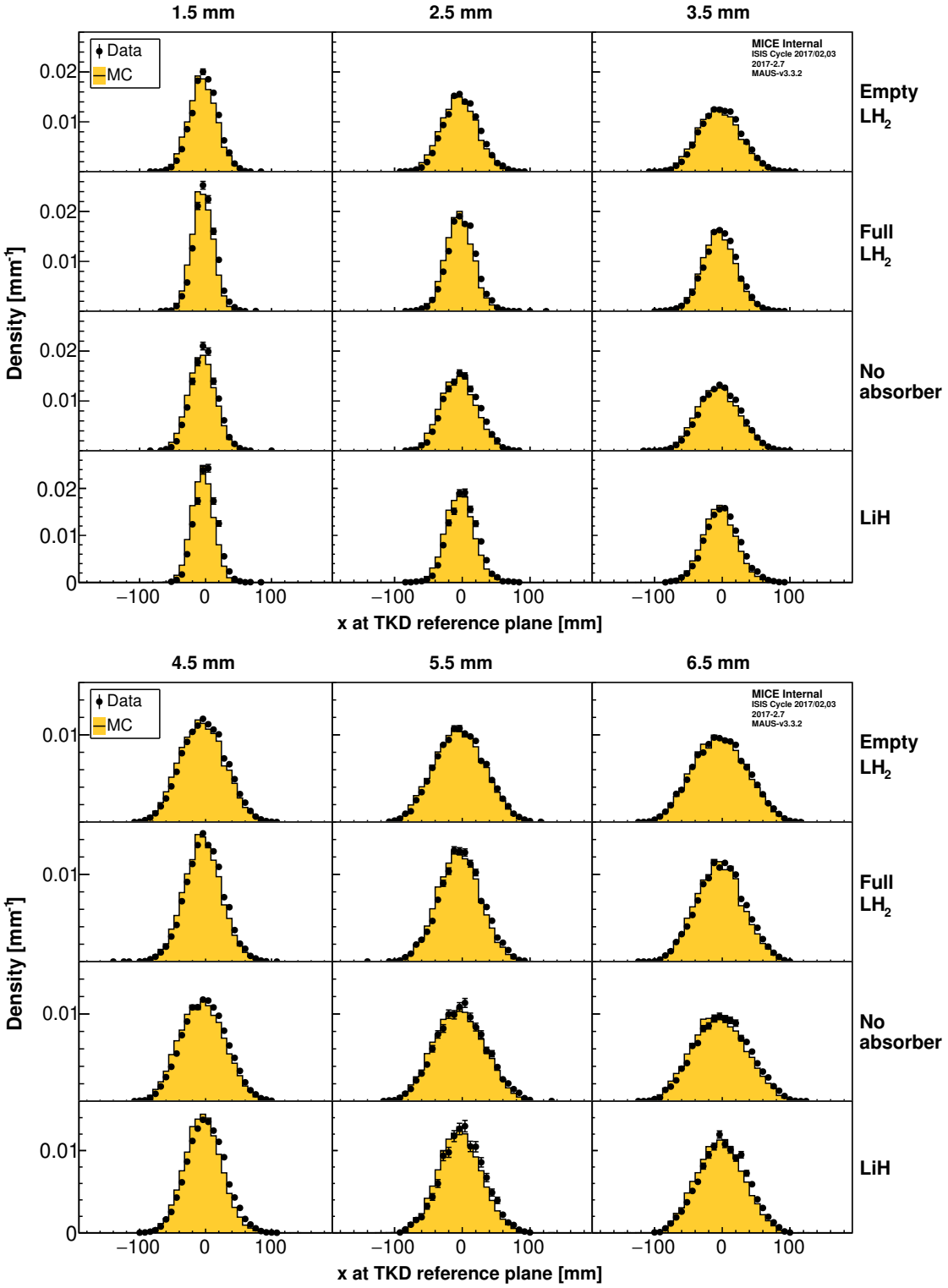

Figure 4.31: Horizontal position distribution at TKU reference plane for the six matched beams.

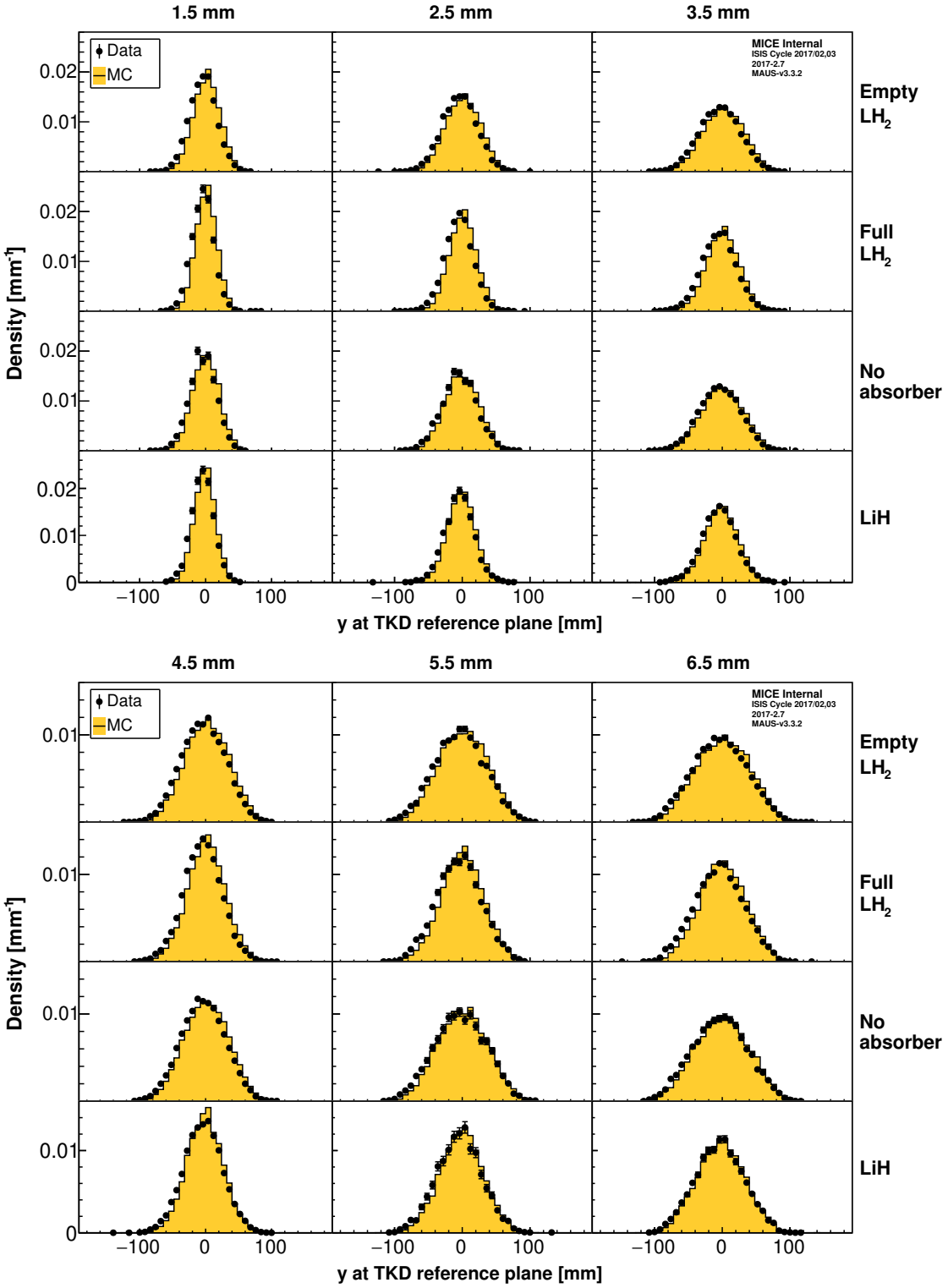

Figure 4.32: Vertical position distribution at TKU reference plane for the six matched beams.

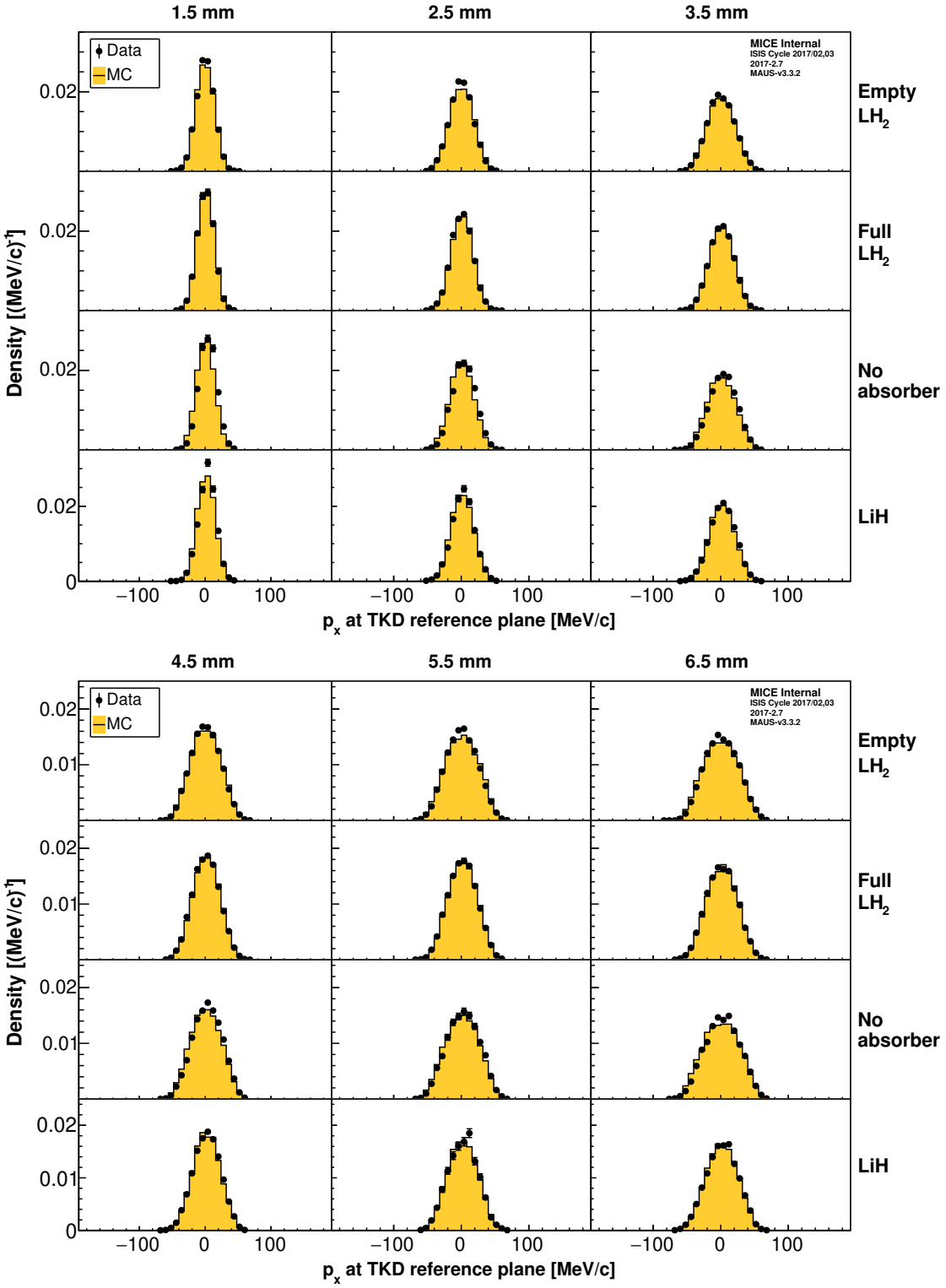

Figure 4.33: Horizontal momentum distribution at TKU reference plane for the six matched beams.

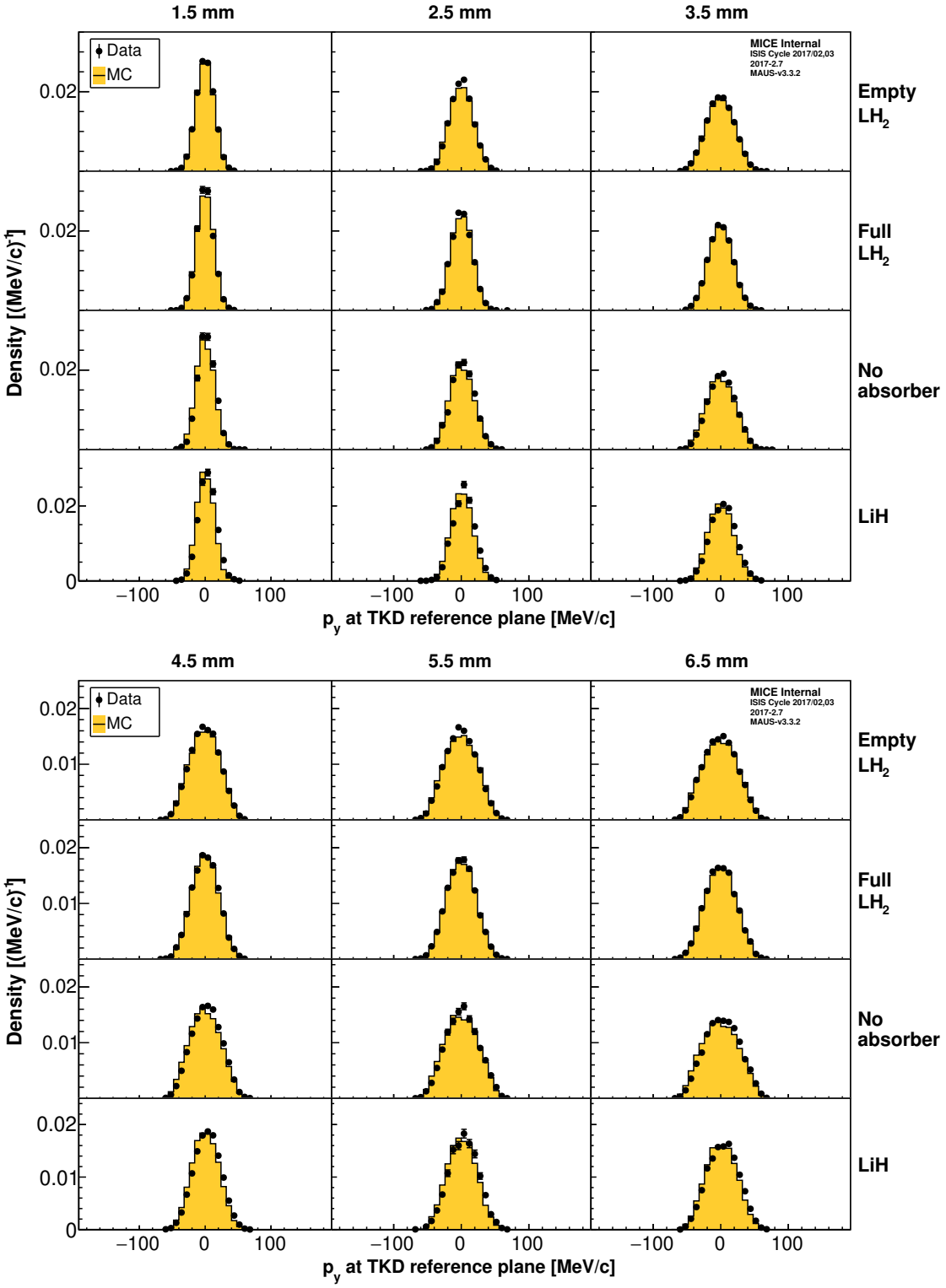

Figure 4.34: Vertical momentum distribution at TKU reference plane for the six matched beams.

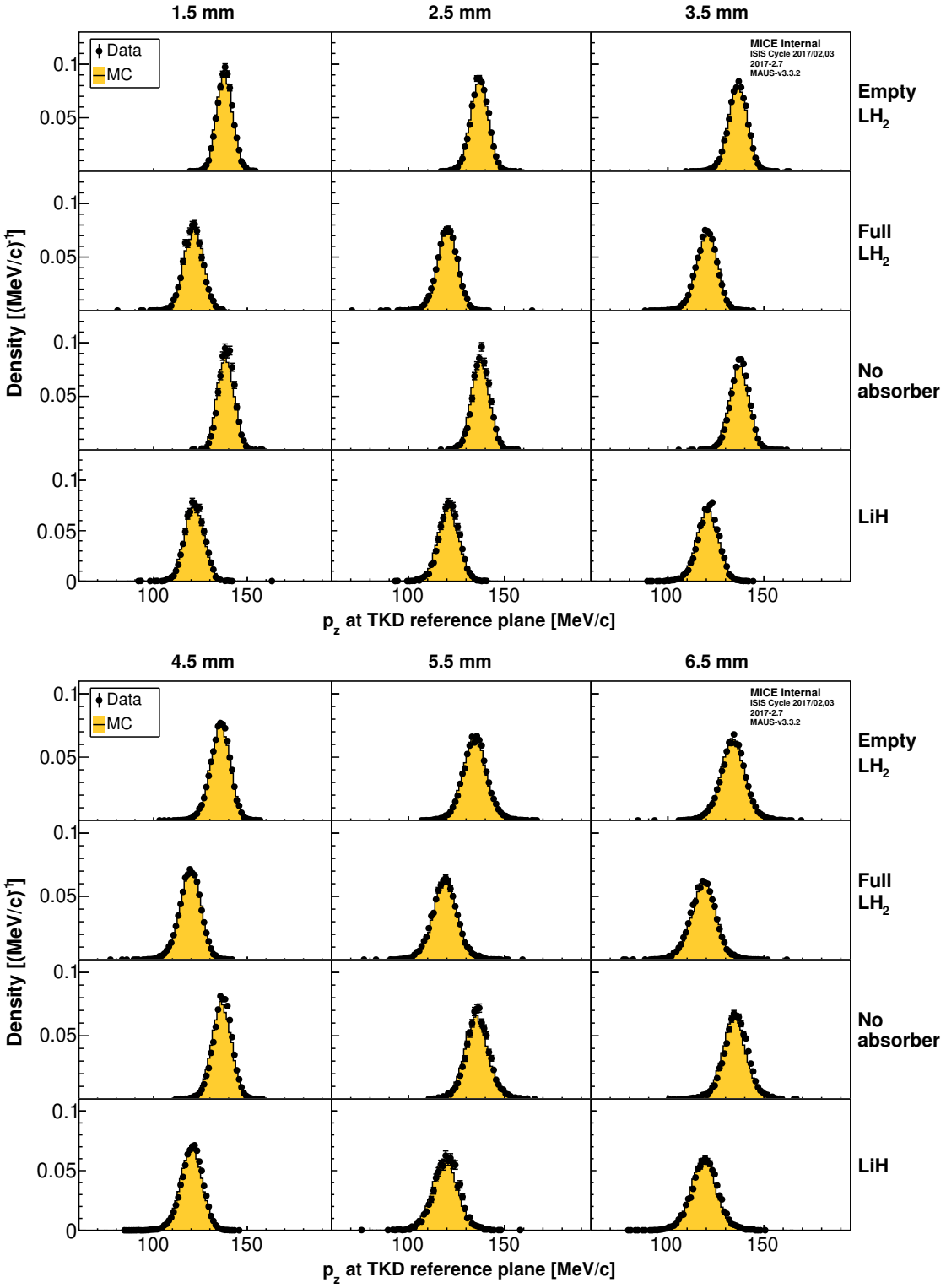

Figure 4.35: Longitudinal momentum distribution at TKU reference plane for the six matched beams.

Beam Optics

The evolution of the transverse Twiss parameters, $\alpha_\perp$ and $\beta_\perp$, of the sampled beams through the cooling channel is presented in figures 4.36 and 4.37. The reconstructed data are in very good agreement with the truth and reconstructed simulation. Both parameters are constant throughout TKU, which demonstrates that the sampled beams are properly matched. As a result, $\beta_\perp$ at the absorber is reduced by comparison with the parent beam (see figure 4.23). The reduction is most significant (up to $\sim 35\%$) for the beams sampled from the 4-140 data sets.

Emittance

The evolution of the normalized transverse emittance, $\epsilon_\perp$, through the cooling channel is shown in figure 4.38. The reconstructed data are well reproduced by the simulation, both truth and reconstructed. Any reconstructed data-simulation discrepancies observed in TKU are related to the accuracy of the sampling procedure. These do not pose any concern as the ultimate goal is to compare the emittance change trends as function of input emittance, which is determined by all six beams.

A first assessment of the beams that cross an absorber reveals that the emittance reduction increases with growing input emittance, with the 1.5 mm beams being slightly heated rather than cooled. It must be noted that at this stage no corrections for systematic biases are applied and no systematic uncertainties are included in the figures. It is further observed that while emittance slightly decreases at the TKU stations, it increases at the last three TKD stations. This heating occurs due to the larger $\beta_\perp$ at these stations, which makes scattering the dominant effect.

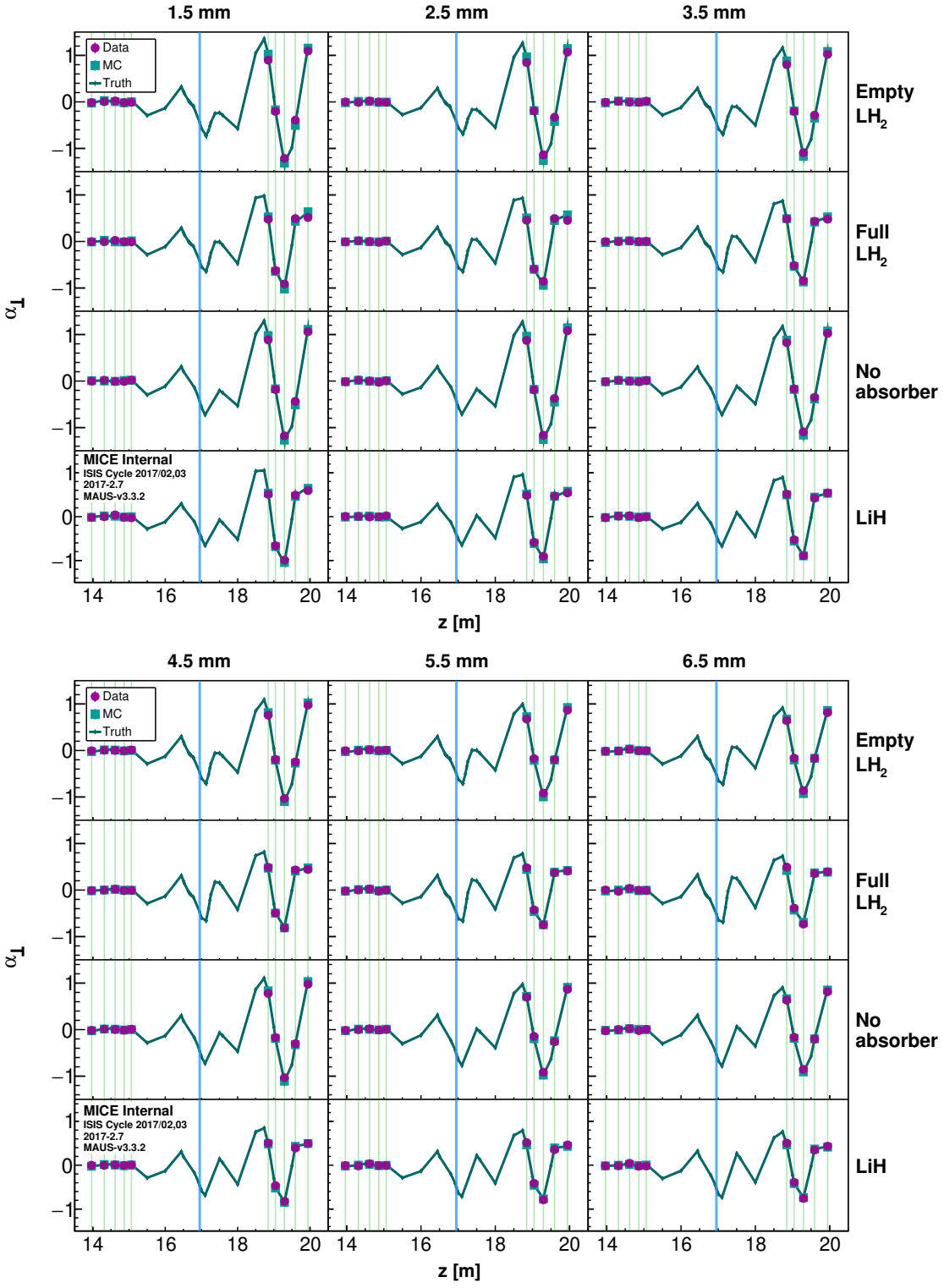

Figure 4.36: Evolution of the transverse Twiss parameter $\alpha_\perp$ through the cooling channel for the six matched beams. The vertical blue line represents the central position of the absorber, while the vertical green lines indicate the position of the five stations in each tracker.

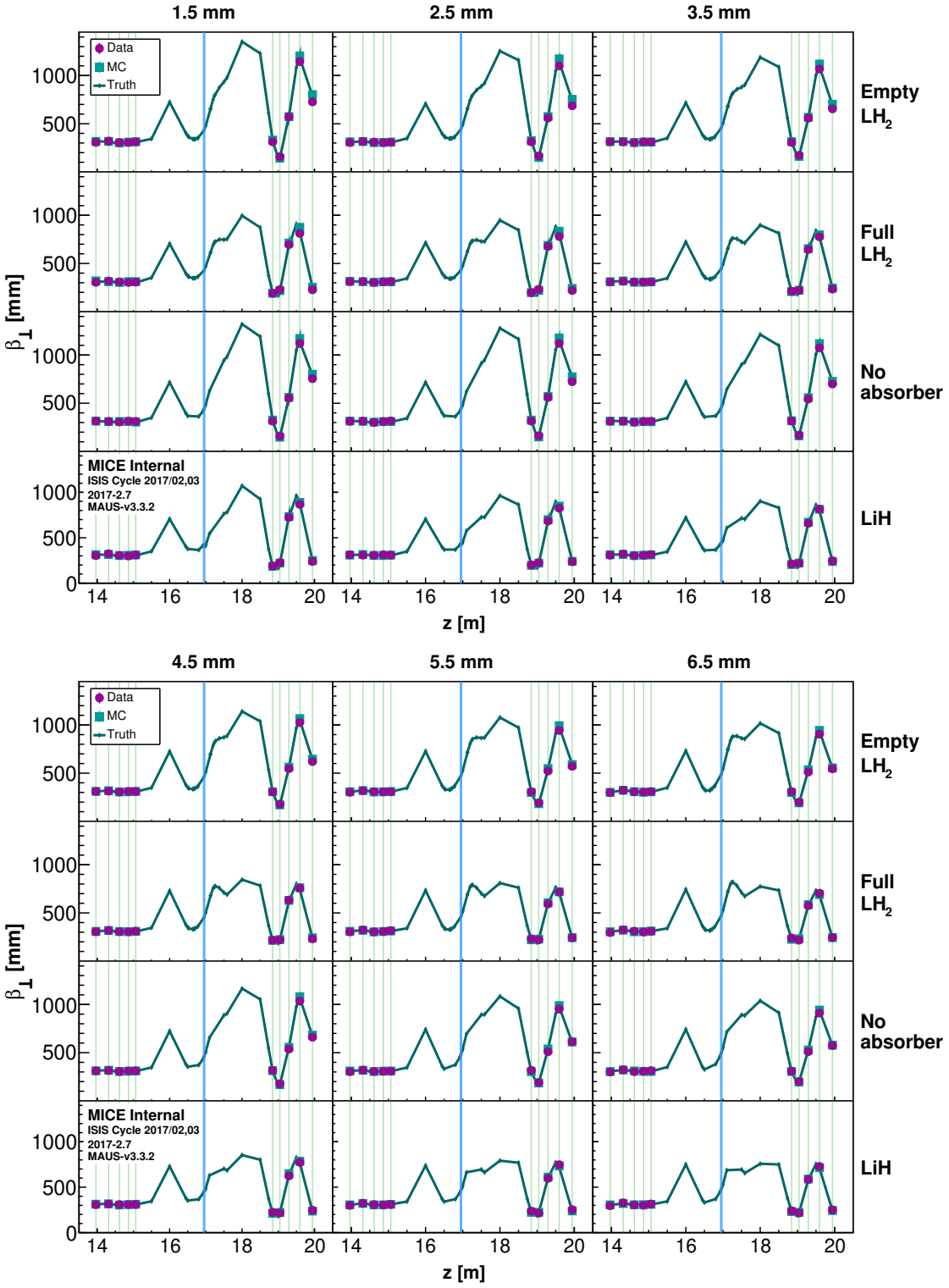

Figure 4.37: Evolution of the transverse Twiss parameter $\beta_\perp$ through the cooling channel for the six matched beams. The vertical blue line represents the central position of the absorber, while the vertical green lines indicate the position of the five stations in each tracker.

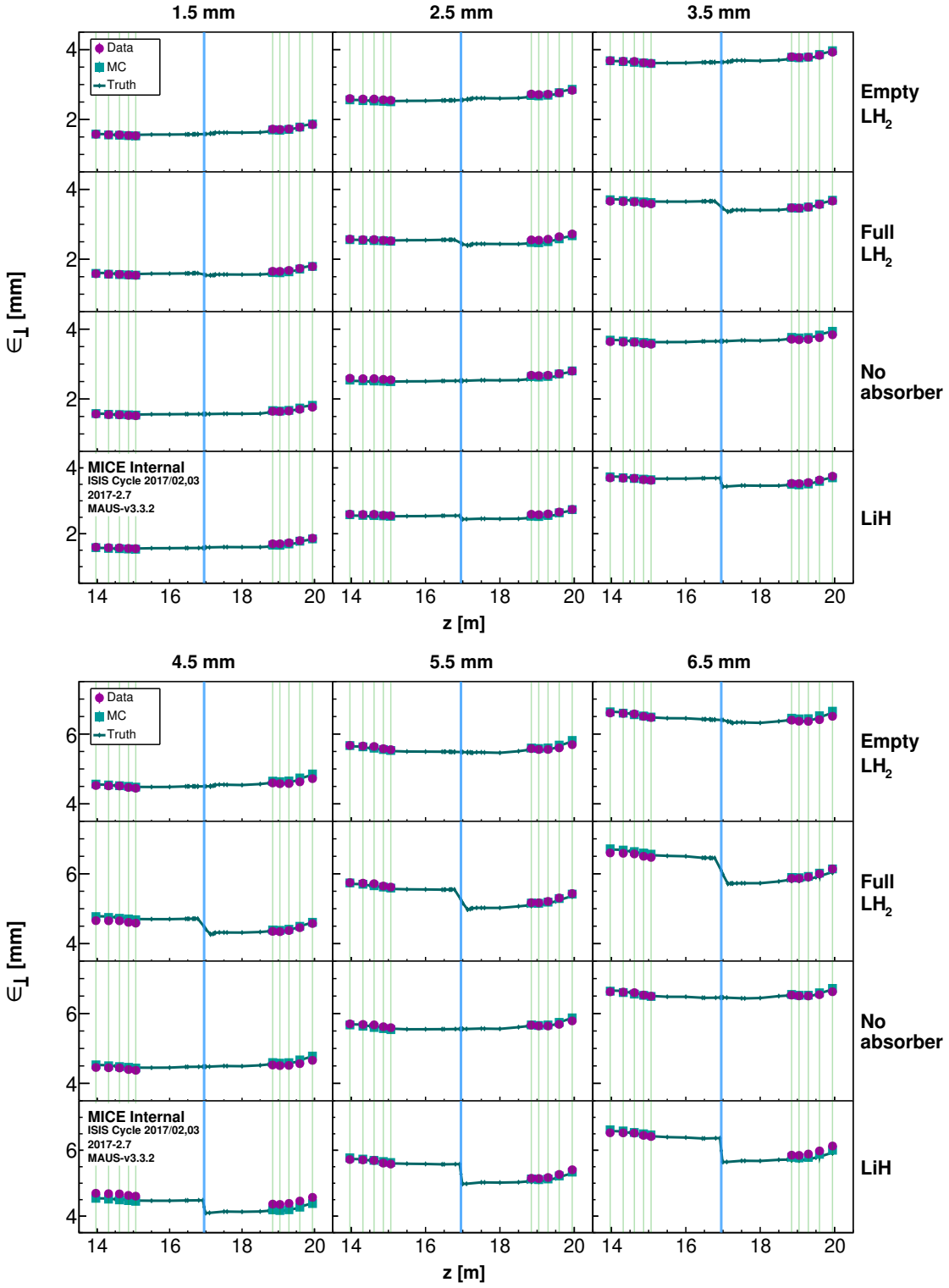

Figure 4.38: Evolution of the transverse RMS emittance $\epsilon_\perp$ through the cooling channel for the six matched beams. The vertical blue line represents the central position of the absorber, while the vertical green lines indicate the position of the five stations in each tracker.

4.5 Emittance Reduction

The main goal of this analysis is to study the emittance reduction induced by the presence of a liquid hydrogen or lithium hydride absorber in the path of muon beams with input emittance in the $[1.5, 2.5, ..., 6.5]$ mm range. The effect is to be studied as a function of input emittance. The emittance change measured by the pair of MICE scintillating fibre trackers is defined as

$$\Delta\epsilon_\perp = \epsilon_\perp^d - \epsilon_\perp^u, \tag{4.10}$$

where $\epsilon_\perp^d$ is the emittance measured at the downstream tracker reference plane and $\epsilon_\perp^u$ is the emittance measured at the upstream tracker reference plane.

4.5.1 Model

Starting from the cooling equation shown in 2.52, one can express the beam emittance change induced by an absorber material of thickness, z, as a function of the input emittance, $\epsilon_\perp^u$, as follows:

$$\Delta\epsilon_\perp(\epsilon_\perp^u) \approx (\epsilon_\perp^{eqm} - \epsilon_\perp^u)\left[1 - \exp\left(-\frac{|dE/dz|}{\beta^2 E}z\right)\right], \tag{4.11}$$

where $\epsilon_\perp^{eqm}$ is the equilibrium emittance as defined in 2.53. During the integration of the cooling equation, the approximation that all beam parameters apart from the emittance remain constant is made.

The mean energy loss rate at the absorber is described by the Bethe-Bloch formula [92],

$$\left|\frac{dE}{dz}\right| = K\rho\frac{Z}{A}\frac{q^2}{\beta^2}\left[\ln\left(\frac{2m_e c^2\beta^2}{I(1-\beta^2)}\right) - \beta^2\right], \tag{4.12}$$

where $K = 4\pi N_A r_e^2 m_e c^2$ is a constant, m_e the electron mass, r_e the classical electron radius, N_A the Avogadro number, ρ the material density, q the particle charge, I the mean excitation energy of the atoms in the material, Z and A the atomic and mass numbers of the material. The radiation length of composite materials is calculated as

$$\frac{1}{X_0} = \sum_i \frac{a_i}{X_i}, \tag{4.13}$$

where X_i is the radiation length of the i^{th} component element and a_i the corresponding mass fraction.

The total emittance change experienced by a MICE beam depends on the type and amount of material it traverses between the TKU and TKD reference planes. The lithium hydride absorber was a disk 65 mm thick, with a radius of 225 mm. The isotopic composition of the lithium used to produce it was 95.52% ^{6}Li and 4.48% ^{7}Li. The filled 22 l liquid hydrogen vessel was 350 mm thick along the beam axis, and had a radius of 150 mm. The vessel windows were made from the Al 6061 T651 alloy [93][94]. As well as passing through the absorber module, the muon beam crossed an additional pair of aluminium windows, one placed at the downstream end of SSU and the other one at the upstream end of SSD. The characteristics of the materials discussed above are shown in table 4.6. The model will be used to provide an approximate theoretical expectation for the cooling performance as a function of input emittance, for comparison with the measurement.

Property \ Material	MICE LiH	Liquid H_2	Al 6061 T651
Density, ρ [g/cm^3]	0.693 [95]	0.07053 [96]	2.727
$\langle Z/A \rangle$	0.56716	0.99212	0.48145
I [eV]	36.5	21.8	166
X_0 [cm]	102.04	866	8.68

Table 4.6: Material properties of the MICE lithium hydride and liquid hydrogen absorbers, as well as those of the aluminium alloy used for the windows [97].

4.5.2 Correction Terms

In order to accurately estimate the cooling performance of the MICE absorbers, all sources of systematic bias must be accounted for. Two types of biases are considered in this analysis - a reconstruction bias due to the detector resolution and correlations between the phase space variables, and another bias introduced by the requirement that events be fully transmitted through the channel, i.e., have a reconstructed track in each tracker.

Reconstruction Bias Correction

Emittance is a statistical quantity that depends on the phase space distribution width and all correlations between the phase space variables. In a particle-by-

particle experiment, even if the phase space variables are accurately measured, their corresponding widths experience a smearing due to statistical fluctuations in the measurement, i.e., detector resolution. The measured distribution of a variable is the convolution between its true underlying distribution and the measurement error distribution. This smearing introduces a systematic increase in the measured emittance.

Additionally, any correlations between the measurement error and the true variables can introduce further bias. For example, a negative correlation between the true value of a phase space variable and the corresponding measurement error would lead to a measured distribution width narrower than the width of the true distribution. Both effects can be estimated and accounted for, assuming a well calibrated detector.

One way to estimate the systematic shift is by studying the impact of the measurement error on the covariance matrix of the reconstructed distribution. Let $\mathbf{m}$ be the measured (reconstructed) phase space vector of a particle. It is related to the true phase space vector, $\mathbf{t}$, through

$$\mathbf{m} = \mathbf{t} + \boldsymbol{\delta}, \tag{4.14}$$

where $\boldsymbol{\delta}$ is the statistical error on the measurement. The covariance matrix of the measured phase space distribution can be expressed in component form as follows:

$$\begin{aligned}
\Sigma^m_{ij} &= \mathrm{cov}[m_i, m_j] = \langle m_i m_j \rangle - \langle m_i \rangle \langle m_j \rangle \\
&= \langle (t_i + \delta_i)(t_j + \delta_j) \rangle - \langle t_i + \delta_i \rangle \langle t_j + \delta_j \rangle \\
&= \langle t_i t_j \rangle - \langle t_i \rangle \langle t_j \rangle \\
&\quad + \langle t_i \delta_j \rangle - \langle t_i \rangle \langle \delta_j \rangle \\
&\quad + \langle \delta_i t_j \rangle - \langle \delta_i \rangle \langle t_j \rangle \\
&\quad + \langle \delta_i \delta_j \rangle - \langle \delta_i \rangle \langle \delta_j \rangle \\
&= \mathrm{cov}[t_i, t_j] + \mathrm{cov}[t_i, \delta_j] + \mathrm{cov}[\delta_i, t_j] + \mathrm{cov}[\delta_i, \delta_j].
\end{aligned} \tag{4.15}$$

This equation can be written in matrix form as

$$\boldsymbol{\Sigma}^m = \boldsymbol{\Sigma}^t + \mathbf{R} + \mathbf{R}^T + \mathbf{C}, \tag{4.16}$$

where $\mathbf{\Sigma}^m$ is the measured covariance matrix, $\mathbf{\Sigma}^t$ is the true covariance matrix and $\mathbf{R}$ and $\mathbf{C}$ are the two covariance matrix correction terms. The $\mathbf{R}$ matrix contains the effects due to the correlations between the true phase space variables and the measurement errors, while the $\mathbf{C}$ matrix contains the covariances of the individual measurement errors. The diagonal terms of $\mathbf{C}$ give the measurement resolutions of the corresponding phase space variables. Once the individual correction terms are computed, they can be applied to the reconstructed covariance matrix as a correction matrix given by

$$\mathbf{M}_{\text{corr}} = -\mathbf{R} - \mathbf{R}^T - \mathbf{C}. \tag{4.17}$$

An alternative, simpler method, is to calculate the systematic shift (correction) at the emittance level, rather than the covariance matrix, as

$$\epsilon_{\text{corr}} = \langle \epsilon_{\text{reco}} \rangle - \epsilon_{\text{true}}, \tag{4.18}$$

where ϵ_{true} is the emittance of the true simulated ensemble and $\langle \epsilon_{\text{reco}} \rangle$ is the mean emittance calculated by splitting the reconstructed simulated ensemble into N independent subsamples of equal size. This procedure allows for a straightforward estimation of the correction on the emittance change, through

$$\begin{aligned} \Delta\epsilon_{\text{corr}} &= \Delta\epsilon_{\text{reco}} - \Delta\epsilon_{\text{true}} \\ &= (\langle \epsilon^d_{\text{reco}} \rangle - \langle \epsilon^u_{\text{reco}} \rangle) - (\epsilon^d_{\text{true}} - \epsilon^u_{\text{true}}) \\ &= (\langle \epsilon^d_{\text{reco}} \rangle - \epsilon^d_{\text{true}}) - (\langle \epsilon^u_{\text{reco}} \rangle - \epsilon^u_{\text{true}}) \\ &= \epsilon^d_{\text{corr}} - \epsilon^u_{\text{corr}}\,, \end{aligned} \tag{4.19}$$

where ϵ^u_{corr} and ϵ^d_{corr} are the estimated systematic shifts for the upstream and downstream trackers.

A hybrid Monte Carlo simulation is used to estimate the systematic shift and make a correction. The hybrid simulation is different from the full experiment simulation through the location where and the method through which the particles are generated. A kernel density estimation algorithm is applied to the reconstructed data ensemble at TKU station 5 to estimate its underlying density. Particles are then generated by sampling from the KDE density at TKU station 5 and tracked

to the end of TKD. This allows for an optimised production of ensembles with sizes large enough to ensure the statistical fluctuations are suppressed to a level below the magnitude of the systematic shift.

Six simulated beams with input emittances in the 1.5 - 6.5 mm range and with sample sizes up to $\sim 0.5 \times 10^6$ events are produced to estimate the emittance offsets in each tracker. Each reconstructed sample is split into multiple subsamples of 5000 particles and the offset is calculated as the difference between the mean reconstructed emittance and the true emittance. The systematic offsets for the upstream tracker, downstream tracker and the emittance change are shown for two different scenarios in figure 4.39.

In the first scenario, shown in black squares, no corrections are applied to the reconstruction procedure prior to the estimation of the emittance offset. In the upstream tracker, the correlations between the true phase space variables and the measurement errors dominate over the smearing due to detector resolution and lead to a negative systematic shift. The effect is stronger with decreasing input emittance. In the downstream tracker, the measurement error correlations remain the dominating component but have an opposite effect, causing a positive shift. Combined with the detector smearing, this leads to an overall positive systematic offset that is stronger at lower emittances. The systematic shift on the emittance change, calculated using equation 4.19, is positive for all input emittances analysed and it increases with decreasing input emittance. This is applied as a correction to the reconstructed values of emittance change.

In the second scenario, shown in cyan squares, the emittance offset is estimated after the application of the covariance matrix correction defined in equation 4.17. In both trackers, the baseline offset (black squares) is removed and the updated values are consistent with zero. This demonstrates that the covariance matrix correction is an equally valid method to account for the reconstruction bias.

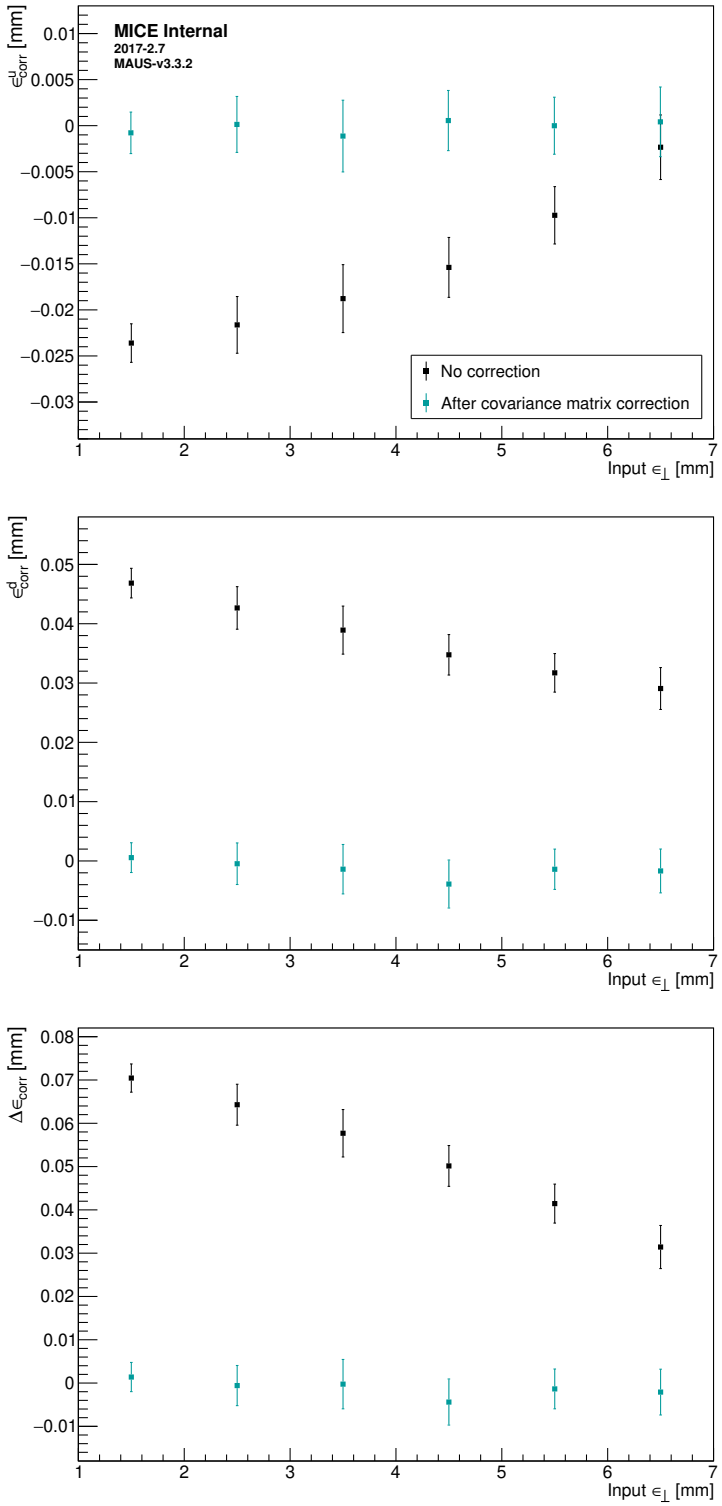

Figure 4.39: Systematic offsets on emittance reconstruction in the (top) upstream and (centre) downstream trackers, and on the (bottom) reconstructed emittance change. Offsets are shown for two scenarios: one where there are no corrections made prior to their calculation (black) and one where the covariance matrix correction is applied before their calculation (cyan).

Full Transmission Correction

The requirement that each analysed event has a reconstructed track in both trackers and survives all downstream selection criteria introduces an additional bias. Under this selection requirement, a fraction of the particles that survive all the PID and upstream tracker cuts is removed from the analysis as they do not have a valid reconstructed track in the downstream tracker (from $\sim$ 2% for 1.5 mm beams to $\sim$ 14% for 6.5 mm beams). This may be due to scraping of the apertures and exiting the channel before reaching the downstream tracker, exiting the tracking fiducial volume, or due to reconstruction inefficiency in TKD.

When an absorber material is present in the path of the beam, the lack of a reconstructed downstream track (via the above-mentioned mechanisms) for a fraction of the particles in the upstream reconstructed ensemble is attributed to multiple scattering in the absorber (heating). Removal of these particles from the upstream ensemble due to the full transmission requirement leads to an upstream ensemble that will, by design, experience less heating in the absorber, i.e., artificial cooling. The effect is expected to be more prominent in beams with large input emittances, which are more susceptible to scraping the apertures.

The procedure devised to estimate the artificial cooling bias is based on the hybrid Monte Carlo simulation discussed in the previous subsection. The aim is to compare the emittance change suffered at the absorber by beams that are fully transmitted into TKD, with the emittance change in beams that are not required to be fully transmitted and pass only the upstream cuts. An accurate bias estimate requires that the emittance change for the latter kind of beams is not skewed by particle losses or scraping. Since the particle losses occur overwhelmingly downstream of the absorber, the study is carried out at the absorber location, i.e., the input and output emittances are calculated at the locations of the upstream and downstream boundaries of the absorber module. To access the beam phase space distribution at the absorber boundaries, the true simulation ensemble corresponding to the reconstructed simulation ensemble is used.

Beams with input emittances in the $\sim$ 1.0 - 6.5 mm range and with sample sizes of order 10^5 muons are simulated to estimate the correction as a function of input emittance. The true emittance change measured at the absorber module for beams that are fully transmitted and beams that are partially transmitted into the downstream tracker, as well as the estimated correction, are shown in figure

4.40 for the four absorber settings. In the absence of any material between the entry and exit planes of the absorber module ('No absorber'), emittance changes of order 10^{-3} mm are observed for both types of beams. No bias is observed in the fully transmitted beams. By contrast, a bias becomes apparent when the LiH absorber is installed. The beams that suffer transmission losses downstream of the absorber show linear cooling across it, as expected from equation 4.11, while the fully transmitted beams show additional cooling that grows with input emittance. The two cooling trends are fitted with a linear and a polynomial function, respectively. The correction is calculated as the difference between the emittance change trend of the fully transmitted beams and that of the partially transmitted beams.

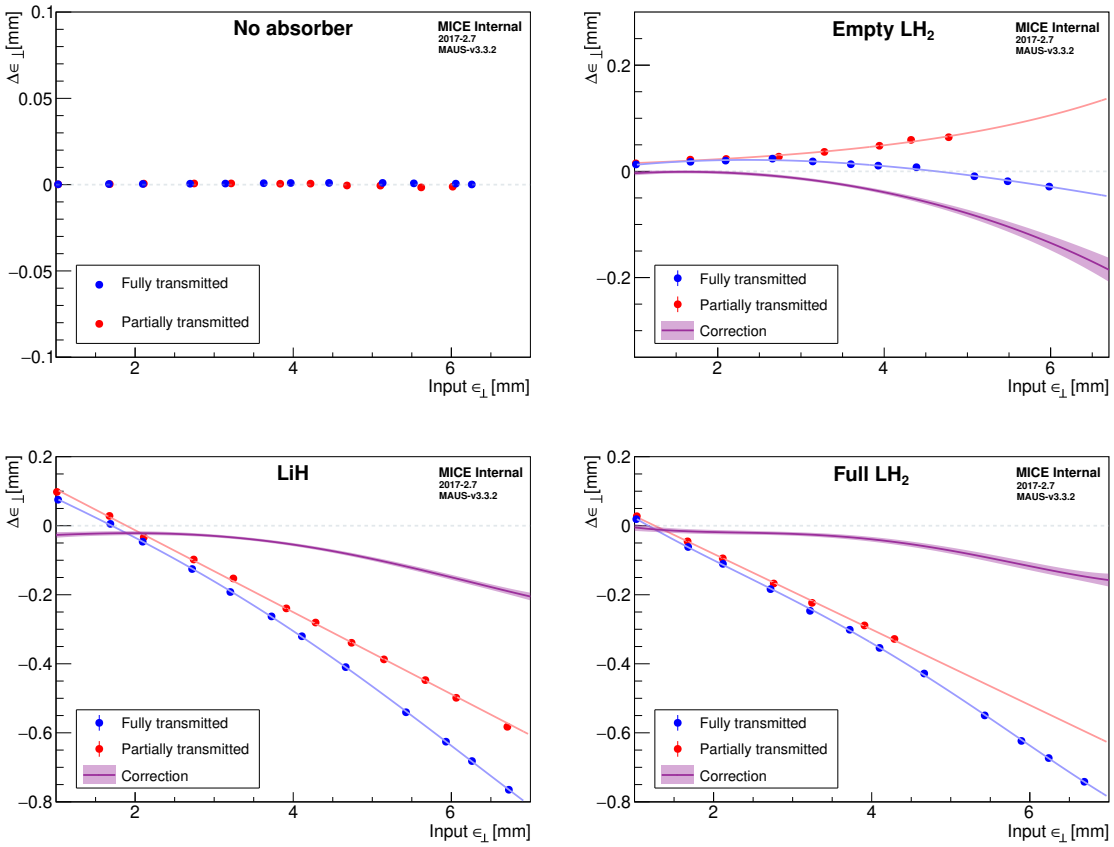

Figure 4.40: True emittance change measured at the absorber module for beams that are (blue) fully and (red) only partially transmitted into TKD. When estimated, the correction is shown by the magenta line. The lighter magenta band gives the 68.3 % confidence interval in the correction function. Results are shown for the four absorber settings, which are explicitly stated on the corresponding subfigure.

A similar bias effect is observed when the full liquid hydrogen vessel ('Full LH_2') is installed. Determining the cooling trend for the beams that are only partially transmitted in TKD becomes more difficult, as the tails of the beams with input emittances larger than $\sim$ 5 mm scrape the radial aperture of the vessel near the downstream Al window. This occurs as the beam is expanding rapidly due to the absence of the M1 coil. Some of the scraping particles exit the channel and some scatter back into the beam, rendering the emittance change measurement unreliable. Hence, these beams are discarded from the study. Nonetheless, a linear cooling trend is assumed over the entire range of input emittances, which is well determined by the beams with emittances lower than $\sim$ 5 mm.

When the vessel is empty ('Empty LH_2'), the beams expand even more rapidly while crossing the absorber module. The beams that are partially transmitted in TKD are heated due to a combination of scattering in the downstream vessel window and non-linear dynamics experienced by the tails of the distribution. The heating is seen to increase non-linearly, and beams with emittances larger than $\sim$ 5 mm are discarded from the study due to scraping. The fully transmitted beams do not contain the heated particles that are subsequently lost downstream of the absorber. Thus, the beams with emittances larger than $\sim$ 5 mm appear to be slightly cooled. The correction for this bias is estimated as the difference between the two trends.

4.5.3 Uncertainties

The uncertainty on the emittance change measurement is compounded of statistical uncertainties and uncertainties on the correction for the systematic bias. The statistical errors stem from fluctuations in the stochastic processes that the beam is subjected to and from fluctuations in the systematic correction. While the statistical error in the correction estimation can, in practice, be reduced by increasing the simulation sample sizes, this cannot be achieved for the reconstructed data whose sample size is fixed. For the reconstructed data and simulation, the statistical uncertainty on the emittance change is estimated by resampling the beams and calculating the bootstrapped 68.3% confidence intervals [98].

The correction procedure assumes a perfect knowledge of the detector system and the magnetic field. As in reality our knowledge is limited, a systematic uncertainty on the emittance change measurement arises. To understand this uncertainty, alterations to the simulation of the detector system are introduced. The resulting

shift in the correction is treated as the uncertainty. In each tracker, the following alterations are introduced one-by-one [99]:

- Tracker displaced in the horizontal plane by 3 mm;
- Tracker rotated in the horizontal plane by 3 mrad;
- Centre Coil field strength varied by 1% (see section 4.2.1);
- End Coils field strength varied by 5%;
- Tracker glue density varied by 50%.

Additionally, as the TOF01 time influences the sample selection indirectly through the contribution to the longitudinal momentum reconstruction, a TOF01 time variation of 60 ps is studied. This variation corresponds to the mean discrepancy observed between the reconstructed data and simulation. The shifts in the correction induced by the individual parameter alterations are added in quadrature to form the total systematic uncertainty.

The effect on the correction generated by the simulation alterations in the two trackers is shown in figure 4.41, for beams with input emittances in the [1.5, 2.5, ..., 6.5] mm array. The TOF01 effect is presented together with the TKU alterations. The dominant systematic uncertainty is due to the field strength in the Centre Coil and is proportional to the input emittance. This behaviour is expected as the field strength in the tracking region plays a central role in the momentum reconstruction. The effects due to the End1 and End2 Coils also have a significant contribution to the total systematic uncertainty. The larger shift due to the End1 Coil field variation is attributed to its placement in the vicinity of the tracker reference plane, where the emittance measurement is performed.

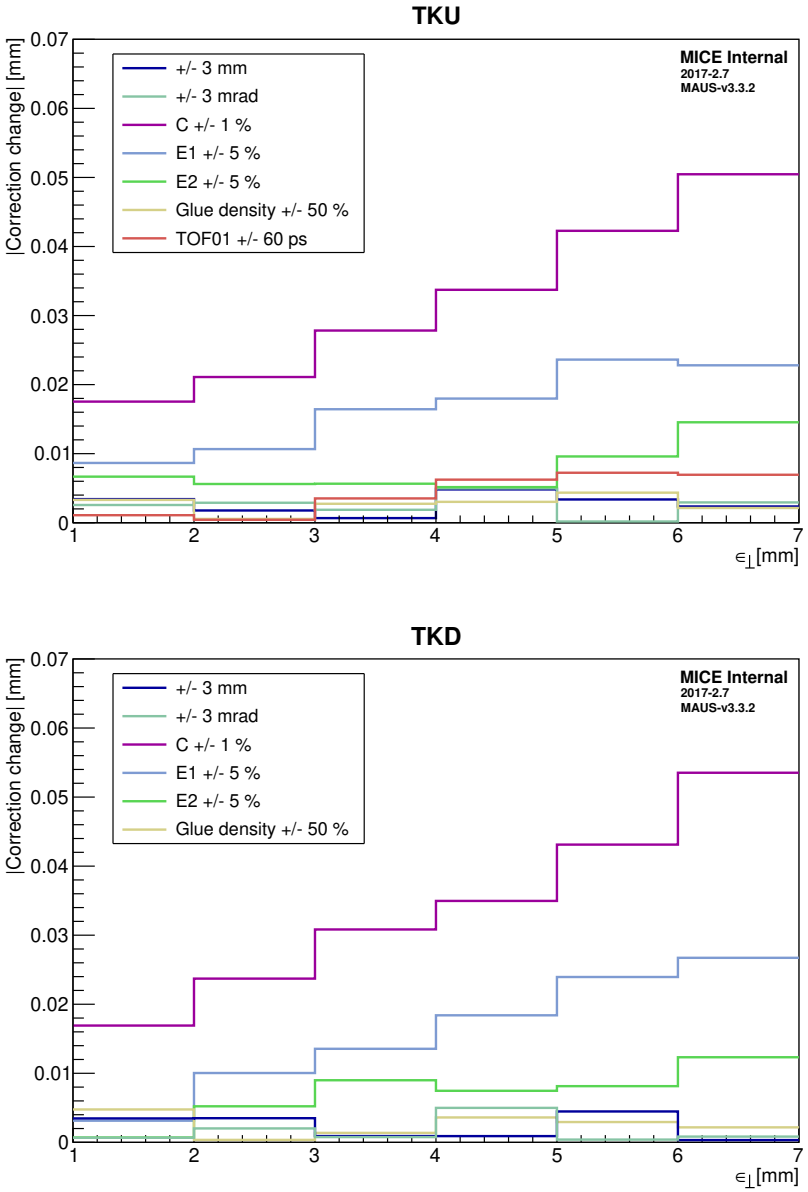

Figure 4.41: Systematic uncertainties on the emittance change correction induced by (top) upstream tracker and TOF01 and (bottom) downstream tracker simulation alterations.

4.5.4 Cooling Results

Figure 4.42 shows the emittance change induced by the liquid hydrogen and the lithium hydride absorbers, as well as the corresponding control empty cases, for beams with input emittances in the [1.5, 2.5, ..., 6.5] mm range. The measurement uncertainty depicted by the coloured bands is dominated by systematic uncertainties. A very good agreement between data and simulation is observed in all configurations. Additionally, the reconstructed data agree well with the model prediction computed using equation 4.11. The model includes the contributions from the Al windows. For each absorber configuration, the beam parameters at the absorber and the Al windows used in the model calculation are informed from the true simulation of the 3.5 mm beam.

The control cases show no cooling effects – slight heating occurs due to the SSU and SSD Al windows and optical aberrations in the empty channel ('No absorber') case, while additional heating caused by scattering in the liquid hydrogen vessel windows is observed in the 'Empty LH_2' case. The 'LiH' and 'Full LH_2' absorbers demonstrate emittance reduction for beams with emittances larger than $\sim$ 2.5 mm. This is a clear signal of ionisation cooling, a direct consequence of the presence of an absorber material in the path of the beam. Furthermore, the improvement of the measured cooling performance due to beam matching is striking, considering that the reconstructed 4 mm unmatched parent beams do not show significant cooling. The emittance change measurements for the reconstructed data are listed in table 4.7, with the associated statistical and systematic uncertainties.

For beams with 140 MeV/c momentum and $\beta_\perp = 450$ mm at the absorber, the theoretical equilibrium emittances of the MICE liquid hydrogen and lithium hydride absorbers (excluding the contributions from the Al windows) are $\sim$ 1.5 mm and $\sim$ 2.4 mm, respectively. By performing a linear fit to the data cooling trends in figure 4.42, the effective equilibrium emittances of the absorber modules are estimated to be at 2.3 $\pm$ 0.5 mm for liquid hydrogen and 2.6 $\pm$ 0.5 mm for lithium hydride. These results indicate that the effective cooling performance of the liquid hydrogen absorber is degraded by scattering in the vessel windows. It is marginally better, but within the margin of uncertainty, than that of the lithium hydride disk. It is worth noting that the heating in the vessel windows is larger than the amount predicted by simulations of the initial MICE Step IV design, due to a lack of adequate focusing in the absence of the M1D coil.

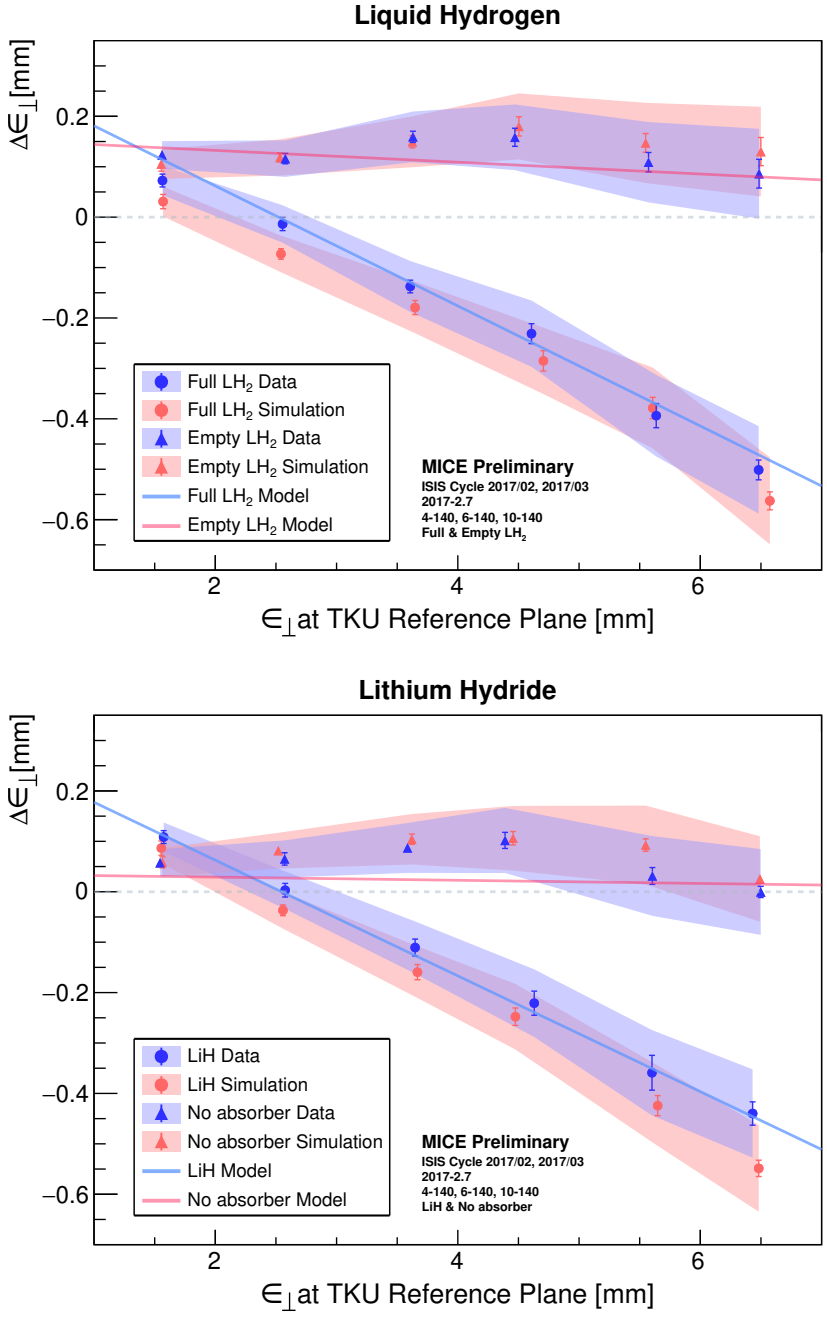

Figure 4.42: Emittance change between the upstream and the downstream tracker reference planes as a function of emittance at the upstream tracker (TKU), for 140 MeV/c beams crossing (top) the liquid hydrogen and (bottom) the lithium hydride MICE absorbers. Results for the control cases, 'Empty LH_2' and 'No absorber', are also shown. The measured effect is shown in blue, while the simulation is shown in red. The statistical uncertainty is indicated by the error bars, while the total error is shown by the semi-transparent fill. The solid lines represent an approximate theoretical model for the (light blue) absorber and (light pink) control cases.

	$\Delta\epsilon_\perp$ [mm]	
Input $\epsilon_\perp$ [mm]	Empty LH_2	Full LH_2
1.5	0.123 ± 0.009 ± 0.026	0.073 ± 0.013 ± 0.026
2.5	0.116 ± 0.010 ± 0.035	-0.014 ± 0.013 ± 0.035
3.5	0.159 ± 0.011 ± 0.048	-0.138 ± 0.013 ± 0.048
4.5	0.158 ± 0.018 ± 0.063	-0.231 ± 0.020 ± 0.063
5.5	0.109 ± 0.019 ± 0.077	-0.394 ± 0.024 ± 0.077
6.5	0.086 ± 0.028 ± 0.084	-0.501 ± 0.020 ± 0.084
Input $\epsilon_\perp$ [mm]	No absorber	LiH
1.5	0.058 ± 0.008 ± 0.026	0.109 ± 0.013 ± 0.026
2.5	0.065 ± 0.012 ± 0.035	0.003 ± 0.014 ± 0.035
3.5	0.087 ± 0.007 ± 0.048	-0.111 ± 0.017 ± 0.048
4.5	0.102 ± 0.016 ± 0.063	-0.221 ± 0.024 ± 0.063
5.5	0.031 ± 0.017 ± 0.077	-0.359 ± 0.034 ± 0.077
6.5	0.000 ± 0.011 ± 0.084	-0.440 ± 0.023 ± 0.084

Table 4.7: Measured emittance change for 140 MeV/c momentum beams crossing the four different absorber configurations in the MICE 'flip mode' (2017-2.7 magnetic channel setting). The statistical errors are listed followed by the systematic errors.

Chapter 5

Canonical Angular Momentum Change in MICE 'Flip Mode'

The preferred solution for linear cooling channels is a periodic lattice of solenoid magnets, as it provides strong cylindrically symmetric focusing at the absorbers, which enhances cooling. Nonetheless, if the beam traverses an absorber in a region of significant solenoidal field, the magnitude of the beam canonical angular momentum increases. The periodic nature of such interactions in a cooling channel would lead to a build-up of canonical angular momentum. This is detrimental to cooling, as it can make the beam increasingly harder to focus and can cause a mismatch.

The proposed solutions to maintain an approximately constant and close to zero canonical angular momentum throughout the cooling section are based on alternating the solenoid field polarity. Within such solutions, any build-up generated before the field flip location is cancelled out after it. The MICE cooling cell was designed to enable operation in a magnetic configuration that produced a field polarity flip at the absorber, known as the 'flip mode'.

Aside from the 'flip mode', MICE also collected data in the so-called 'solenoid mode', a configuration in which the field had a positive polarity throughout the magnetic channel. The analysis presented in this chapter focuses on the change in canonical angular momentum experienced by beams that are cooled in the MICE 'flip mode'.

5.1 Expected Rate of Change

The rate of change per unit length of the beam's mean canonical angular momentum upon passage through an absorber material can be calculated by taking the derivative with respect the longitudinal coordinate, z, of the equation 2.42, as follows:

$$\begin{aligned}\frac{d\langle L_{canon}\rangle}{dz} \simeq \frac{d\langle xp_y\rangle}{dz} - \frac{d\langle yp_x\rangle}{dz} + \frac{qB_z}{2}\left(\frac{d\langle x^2\rangle}{dz} + \frac{d\langle y^2\rangle}{dz}\right) \\ + \frac{q}{2}\frac{dB_z}{dz}\left(\langle x^2\rangle + \langle y^2\rangle\right).\end{aligned} \tag{5.1}$$

By applying the product rule to the first two terms and using $dx/dz = p_x/p_z$ and $dy/dz = p_y/p_z$, the equation can be rewritten as

$$\begin{aligned}\frac{d\langle L_{canon}\rangle}{dz} \simeq \left\langle x\frac{dp_y}{dz}\right\rangle - \left\langle y\frac{dp_x}{dz}\right\rangle + \frac{qB_z}{2}\left(\left\langle 2x\frac{p_x}{p_z}\right\rangle + \left\langle 2y\frac{p_y}{p_z}\right\rangle\right) \\ + \frac{q}{2}\frac{dB_z}{dz}\left(\langle x^2\rangle + \langle y^2\rangle\right).\end{aligned} \tag{5.2}$$

Using the equation for the change of the total momentum with time (assuming zero electric field), i.e.,

$$\frac{d\mathbf{p}}{dt} = v_z\frac{d\mathbf{p}}{dz} = q\mathbf{v}\times\mathbf{B} - \frac{\mathbf{p}}{p}\left|\frac{dE}{dz}\right|, \tag{5.3}$$

expressions for dp_x/dz and dp_y/dz are found as

$$\begin{aligned}\frac{dp_x}{dz} &= q(-B_y + \frac{p_y}{p_z}B_z) - \frac{p_x}{v_z p}\left|\frac{dE}{dz}\right|, \\ \frac{dp_y}{dz} &= q(B_x - \frac{p_x}{p_z}B_z) - \frac{p_y}{v_z p}\left|\frac{dE}{dz}\right|.\end{aligned} \tag{5.4}$$

By substituting the 5.4 expressions in the first two terms of equation 5.2, and using the first order approximations for the transverse magnetic field components $B_x = -\frac{x}{2}\frac{dB_z}{dz}$ and $B_y = -\frac{y}{2}\frac{dB_z}{dz}$, the following is obtained:

$$\begin{aligned}\frac{d\langle L_{canon}\rangle}{dz} \simeq qB_z\left(-\left\langle x\frac{p_x}{p_z}\right\rangle - \left\langle y\frac{p_y}{p_z}\right\rangle\right) + \frac{q}{2}\frac{dB_z}{dz}\left(-\langle x^2\rangle - \langle y^2\rangle\right) \\ - \frac{1}{\langle v_z p\rangle}\left|\frac{dE}{dz}\right|\left(\langle xp_y\rangle - \langle yp_x\rangle\right) + qB_z\left(\left\langle x\frac{p_x}{p_z}\right\rangle + \left\langle y\frac{p_y}{p_z}\right\rangle\right) \\ + \frac{q}{2}\frac{dB_z}{dz}\left(\langle x^2\rangle + \langle y^2\rangle\right).\end{aligned} \tag{5.5}$$

The terms containing the particle charge, q, cancel out, and the simplified expression reads

$$\begin{aligned}\frac{d\langle L_{canon}\rangle}{dz} &\simeq -\frac{1}{\beta^2 E}\left|\frac{dE}{dz}\right|(\langle xp_y\rangle - \langle yp_x\rangle),\\ &\simeq -\frac{1}{\beta^2 E}\left|\frac{dE}{dz}\right|\langle L_{kin}\rangle,\\ &\simeq \frac{1}{\beta^2 E}\left|\frac{dE}{dz}\right|\left[\frac{qB_z}{2}(\langle x^2\rangle + \langle y^2\rangle) - \langle L_{canon}\rangle\right],\end{aligned} \tag{5.6}$$

where $\beta^2 E \simeq \langle v_z p\rangle$.

A change in the mean canonical angular momentum occurs only for beams with non-zero kinetic angular momentum at the absorber. When $\langle L_{kin}\rangle = 0$, the canonical angular momentum reaches an equilibrium value, i.e.,

$$\begin{aligned}\langle L_{canon}\rangle^{eqm} &= \frac{qB_z}{2}(\langle x^2\rangle + \langle y^2\rangle),\\ &= mc\epsilon_\perp\beta_\perp\frac{qB_z}{\langle p_z\rangle},\end{aligned} \tag{5.7}$$

where the definition for the betatron function in equation 2.37 was used to obtain the final expression.

Beams that have a zero or low mean canonical angular momentum before the interaction with an absorber placed in uniform magnetic field, experience a change in this quantity that carries the sign of the field. However, if the field is non-uniform and changes polarity over the region of the absorber, the change in canonical angular momentum is dictated by the interplay between the field, the beam size and beam energy. This is the case of the MICE 'flip mode', where the field is anti-symmetric with respect to the z location of the absorber centre, as shown in figure 5.1. The initial design of the 'flip mode' magnetic configuration allowed for a beam size approximately constant and symmetric about the absorber centre, within the absorber region. Under such conditions, the contribution due to the $\frac{qB_z}{2}(\langle x^2\rangle + \langle y^2\rangle)$ term in equation 5.6 in the upstream half of the absorber may be approximately cancelled out in the downstream half. The term proportional to $-\langle L_{canon}\rangle$ reduces the magnitude of any existing mean canonical angular momentum.

5.2 Equipment Settings

The data sets studied in this chapter are the same as the ones used to analyse the transverse emittance reduction in chapter 4. The details of the apparatus settings during data collection are presented in section 4.1.

Of particular importance for this analysis is the magnetic field polarity flip at the absorber, implemented to prevent canonical angular momentum increase. In MICE 'flip mode', the longitudinal magnetic field is anti-symmetric about the z position of the absorber centre. The field is positive in the upstream half of the absorber and negative in the downstream half. MICE also operated in a magnetic configuration that produced a field with constant positive polarity throughout the whole cooling channel. In this configuration, known as the 'solenoid mode', the field across the absorber region is approximately constant at $\sim$ 1.9 T. An increase in canonical angular momentum is expected, as the beam has a negative mean kinetic angular momentum. A visual depiction of the on-axis longitudinal magnetic field in the two modes is shown in figure 5.1.

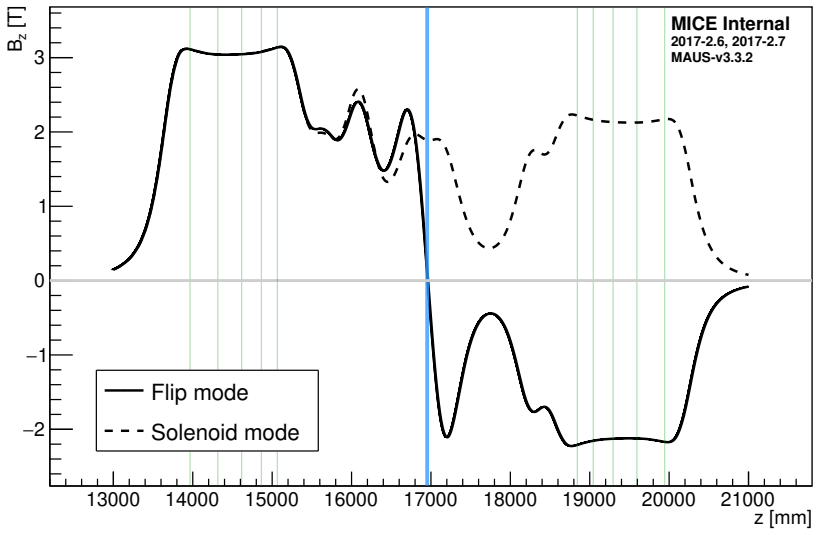

Figure 5.1: On-axis longitudinal magnetic field in the MICE (solid black line) 'flip mode' and (dashed black line) 'solenoid mode'. The corresponding MICE magnetic channel settings are 2017-2.7 and 2017-2.6, respectively. The vertical blue line indicates the position of the absorber centre and the vertical green lines show the locations of the tracker stations. The position along the cooling channel is reported in the global coordinate system of the experiment, where z = 0 at the D2 dipole.

5.3 Event Selection

The set of cuts applied at the event selection stage is the same as in the emittance reduction analysis. The event selection is discussed in detail in section 4.3, where the effects of the cuts, the beam phase space profiles and the beam optics evolution of the final samples are shown. The Monte Carlo simulations of the entire MICE experiment generated for the emittance analysis are also used in this study.

The 2D projections of the beam phase space on the (x, p_y) and (y, p_x) subspaces are shown in figures 5.2-5.5. The reconstructed data are presented in the top panel of each figure, with the reconstructed simulation shown in the bottom panel. The non-zero $x-y$ coupling induced by the solenoidal field is apparent. In each subspace, the correlation changes sign from the upstream to the downstream tracker due to the field polarity flip.

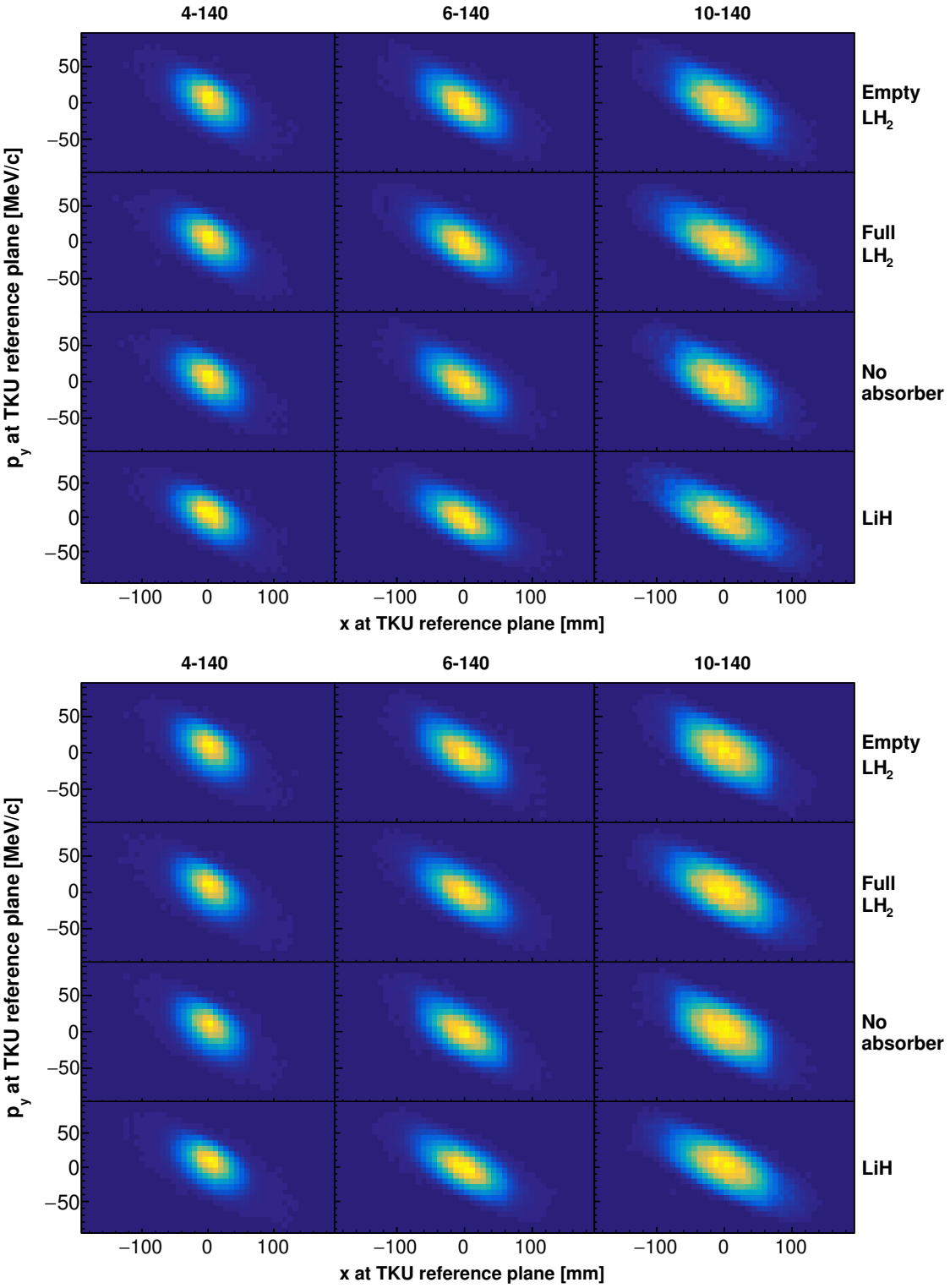

Figure 5.2: Distribution of the events in (x, p_y) at the TKU reference plane for (top) reconstructed data and (bottom) reconstructed simulation.

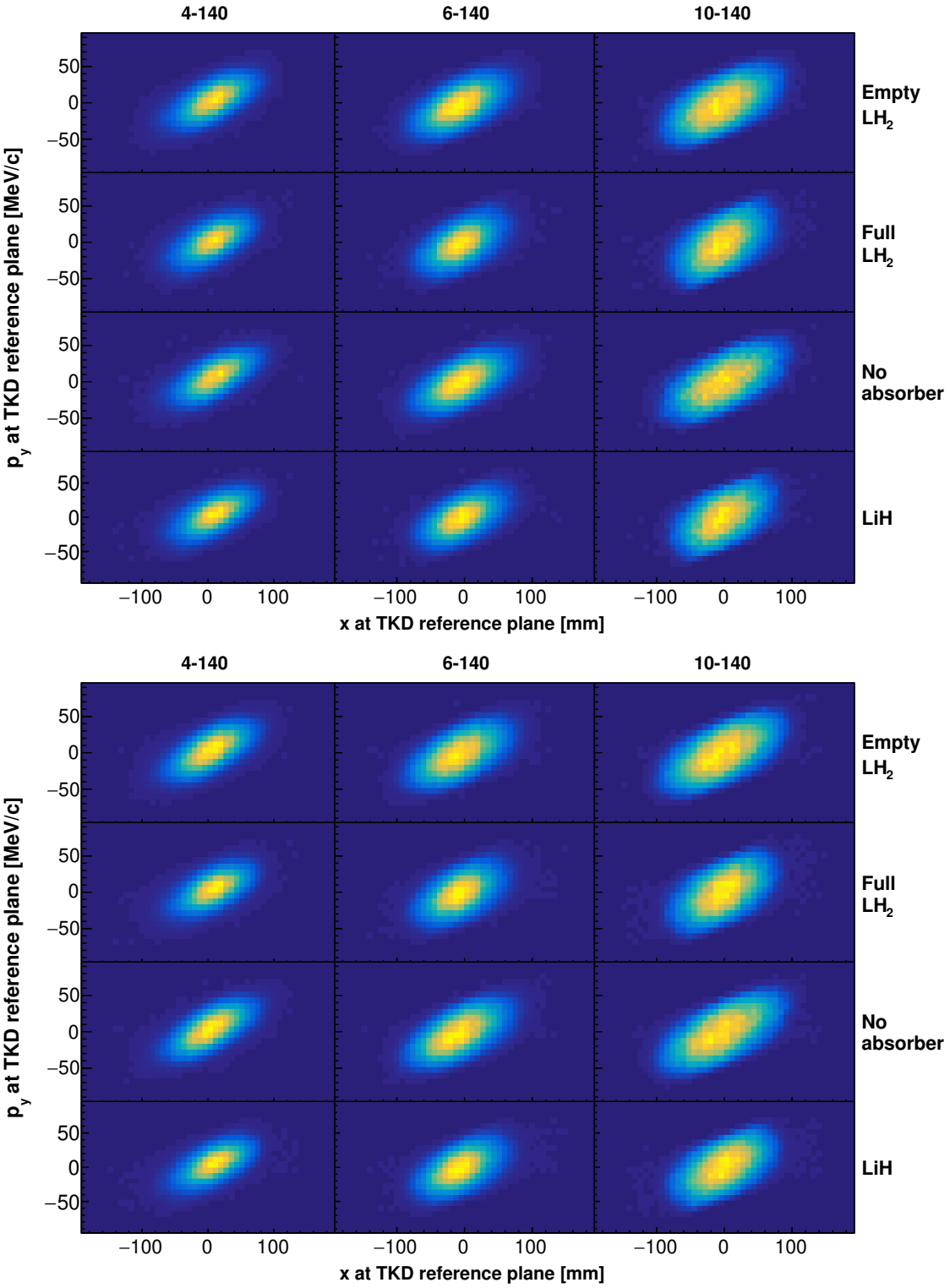

Figure 5.3: Distribution of the events in (x, p_y) at the TKD reference plane for (top) reconstructed data and (bottom) reconstructed simulation.

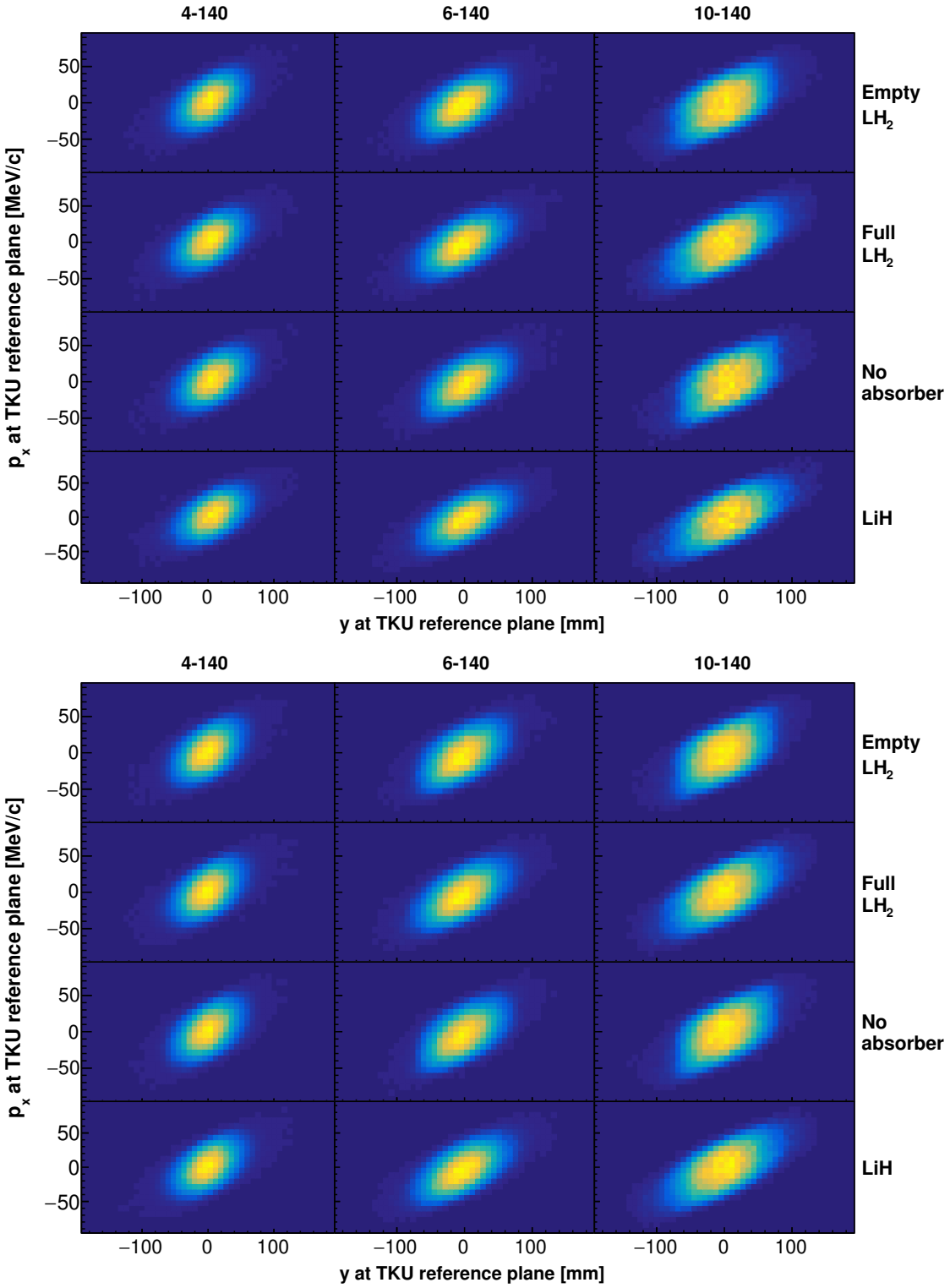

Figure 5.4: Distribution of the events in (y, p_x) at the TKU reference plane for (top) reconstructed data and (bottom) reconstructed simulation.

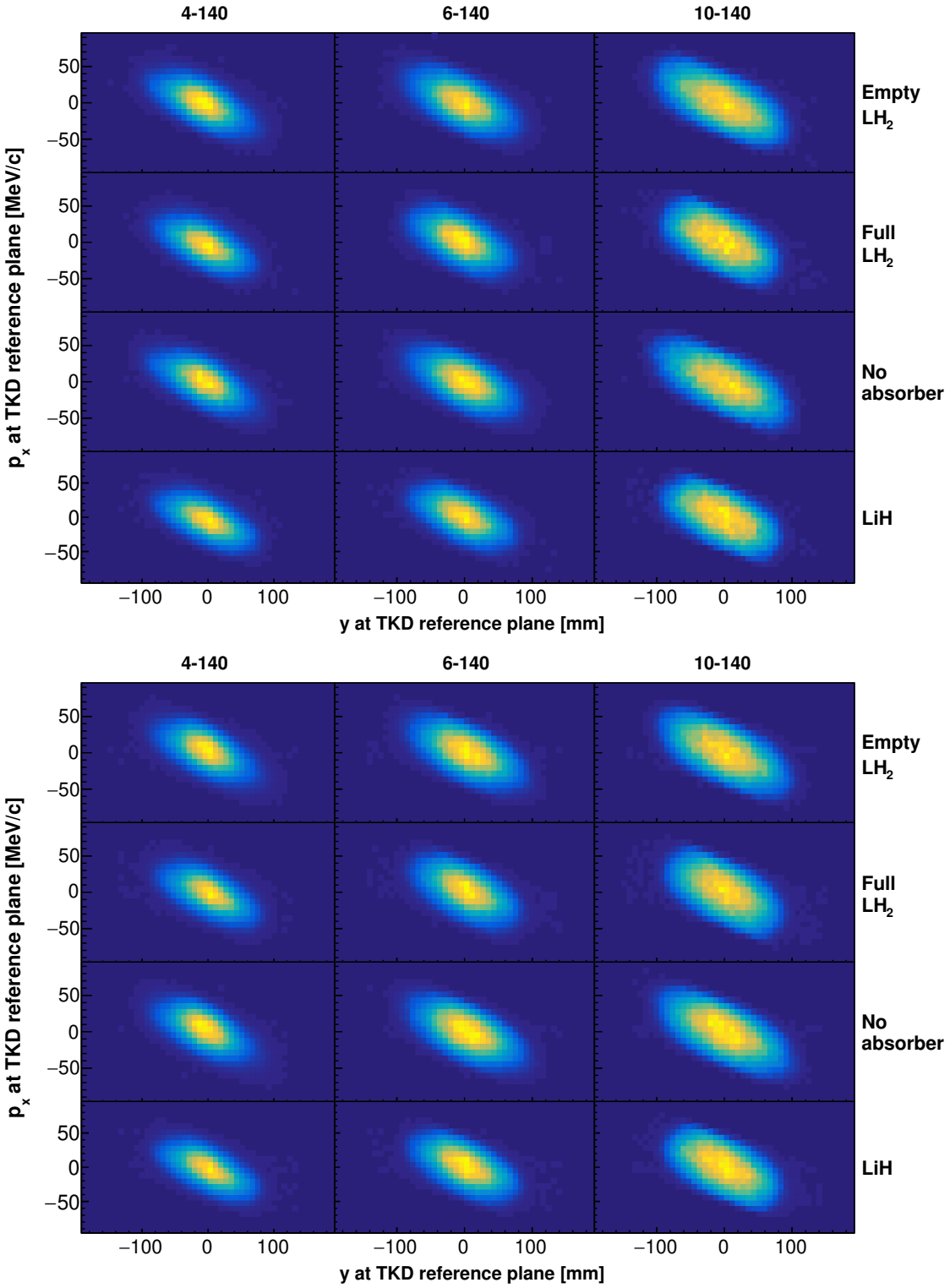

Figure 5.5: Distribution of the events in (y, p_x) at the TKD reference plane for (top) reconstructed data and (bottom) reconstructed simulation.

5.4 Canonical Angular Momentum Change

For each muon in the final ensemble, the canonical angular momentum at all tracker stations is computed as

$$L_{canon} \simeq xp_y - yp_x + \frac{qB_z}{2}r^2. \tag{5.8}$$

The expression is derived from equation 2.40, by using the linear approximation of the vector potential.

The canonical angular momentum distributions at the upstream and downstream tracker reference planes are shown in figure 5.6. The data are represented by the black solid circles, while the MC simulation is shown in yellow fill. The vertical dashed line indicates zero canonical angular momentum. Good agreement between data and simulation is observed at this level of comparison. The upstream distributions peak around zero and have a slight positive skew. This positive mean canonical angular momentum is acquired as the MICE beams, which are produced with $\langle L_{canon} \rangle \approx 0$, interact with the variable-thickness diffuser in a region with strong positive magnetic field, just upstream of TKU. The downstream distributions are observed to behave similarly at this scale of comparison.

For each particle, the change in canonical angular momentum between the upstream and the downstream trackers is calculated as

$$\Delta L_{canon} = L^d_{canon} - L^u_{canon}, \tag{5.9}$$

where L^d_{canon} and L^u_{canon} are the canonical angular momenta measured at the downstream and upstream tracker reference planes. The canonical angular momentum change distributions of the twelve beams are shown in figure 5.7. The data are well reproduced by simulation. The most probable values tend towards zero, but the distributions are slightly asymmetric and negatively skewed, except for the 'No absorber' cases, where the skew is less apparent.

In the presence of an absorber material, the skew is enhanced and the width of the distribution grows. The aluminium windows of the empty liquid hydrogen vessel also introduce a widening of the distribution. These effects can also be observed in figure 5.8, which shows the canonical angular momentum change as a function of the canonical angular momentum at TKU. A negative correlation is noted for beams that

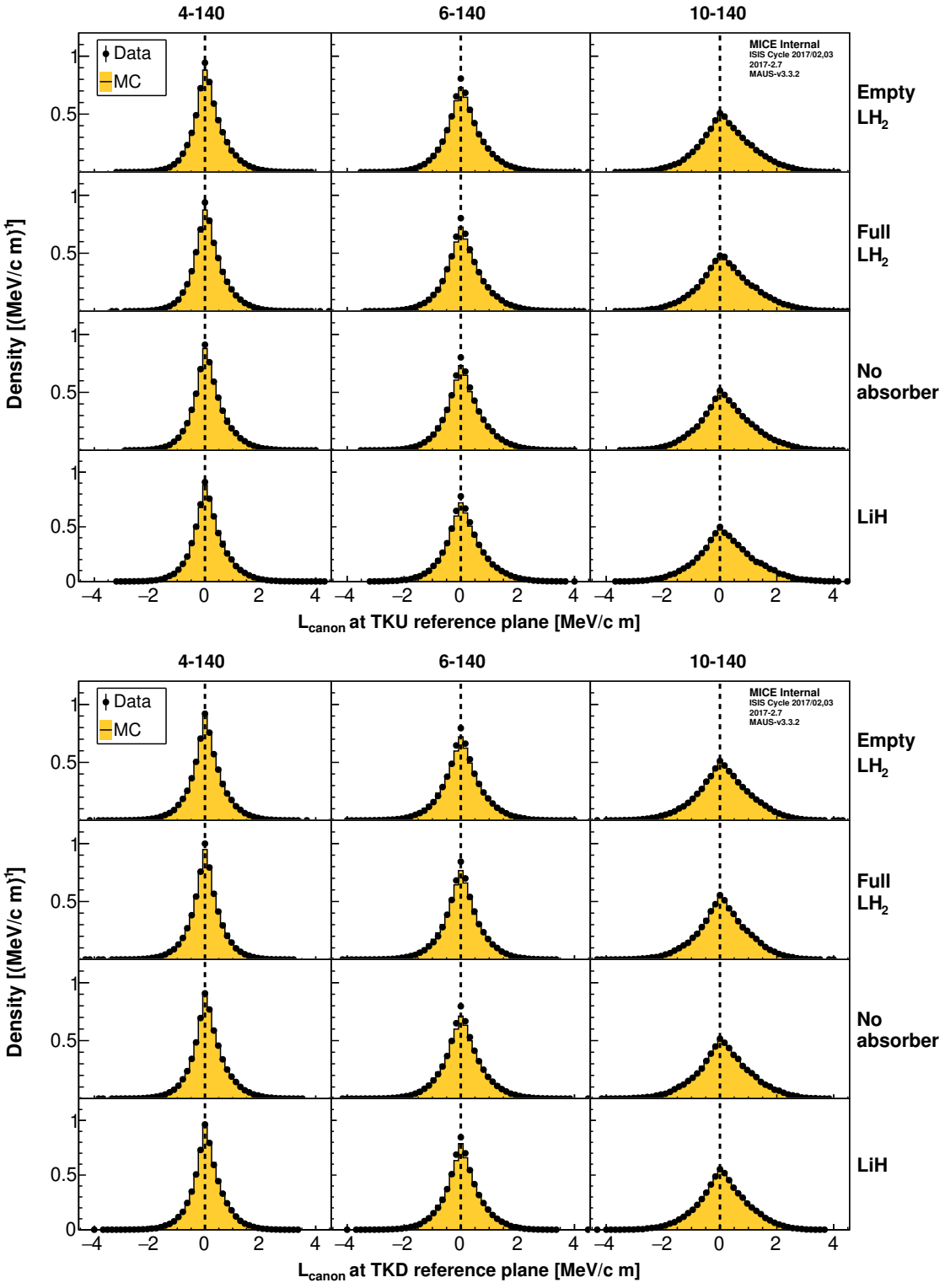

Figure 5.6: Canonical angular momentum distribution at (top) TKU and (bottom) TKD reference planes.

traverse the liquid hydrogen and lithium hydride absorbers. This is expected from equation 5.6, which can be applied to individual particles as well. The quantities presented so far in this section are not corrected for any detector effects. The mean canonical angular momentum change will be presented and discussed after the application of a correction for detector bias.

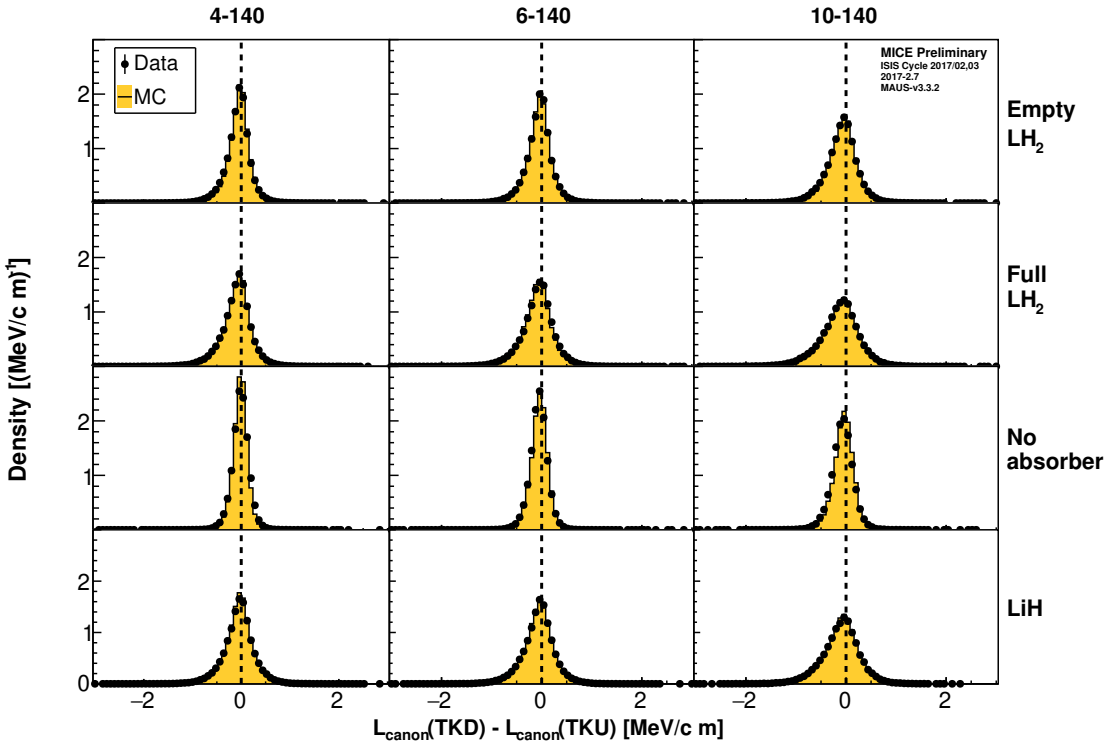

Figure 5.7: Distribution of canonical angular momentum change between the upstream and downstream tracker reference planes.

5.4.1 Correction Term

In section 4.5.2, the effect of the phase space variables measurement error on the reconstructed emittance was discussed. In a similar fashion, any correlations between the measurement errors and the true variables, as well as correlations between the individual measurement errors, can introduce a systematic shift in the measured canonical angular momentum. Additionally, any bias in the reconstructed transverse variables can introduce a similar effect.

The correction for the systematic shift can be calculated in each tracker as

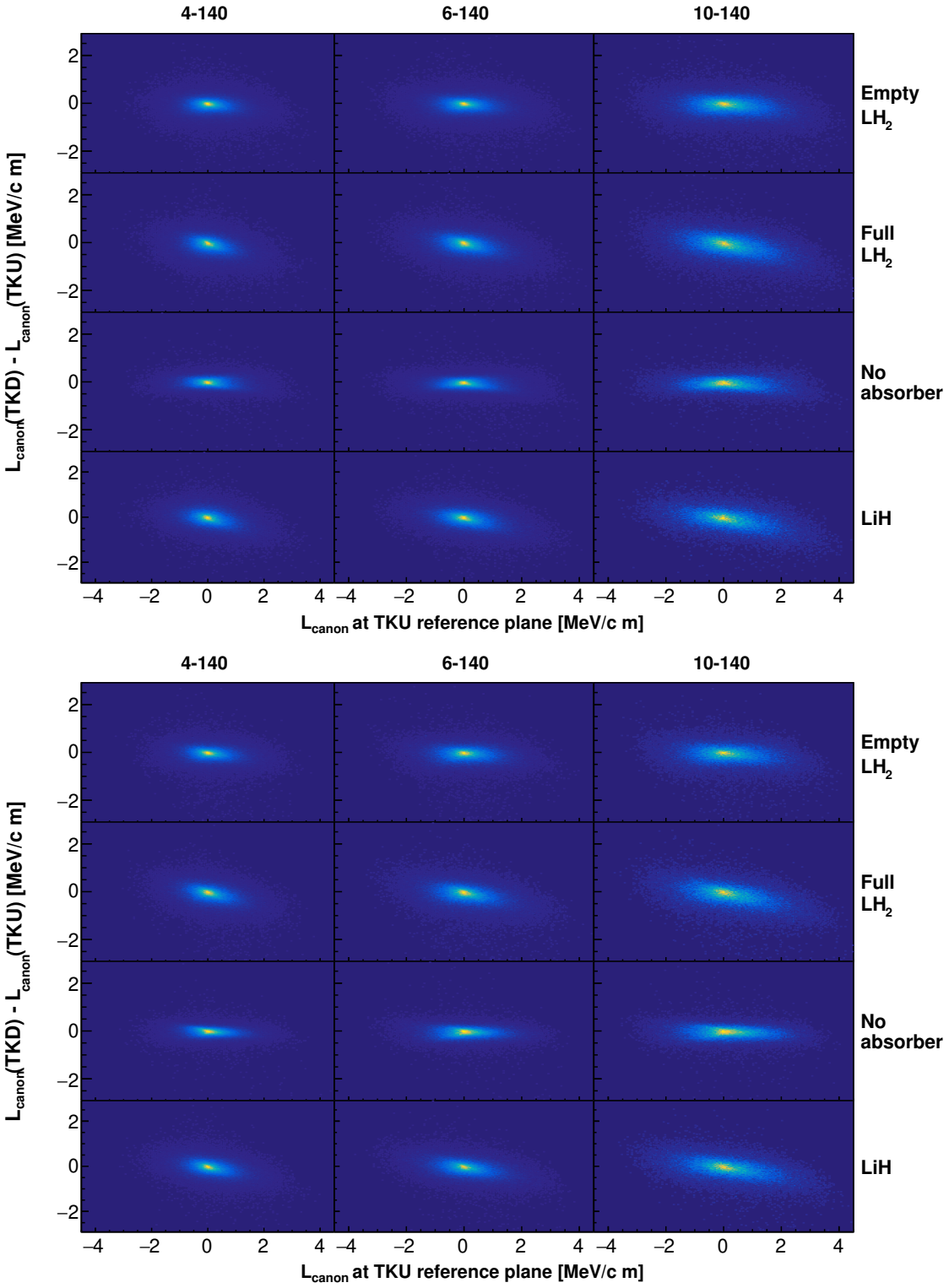

Figure 5.8: Distribution of canonical angular momentum change as a function of the canonical angular momentum at TKU, for (top) reconstructed data and (bottom) reconstructed simulation.

$$L_{corr} = \langle L_{reco} \rangle - \langle L_{true} \rangle, \tag{5.10}$$

where $\langle L_{true} \rangle$ is the mean canonical angular momentum of the true simulated ensemble and $\langle L_{reco} \rangle$ is the mean canonical angular momentum of the reconstructed simulated ensemble. Then the correction on the canonical angular momentum change reads

$$\Delta L_{corr} = L^{d}_{corr} - L^{u}_{corr}, \tag{5.11}$$

where L^{u}_{corr} and L^{d}_{corr} are the systematic shifts for the upstream and downstream trackers.

The systematic shifts are estimated using the Monte Carlo simulations produced to calculate the emittance corrections, which are described in section 4.5.2. The systematic uncertainties on these shifts are presented in section 5.4.2. The calculated corrections for the upstream tracker, downstream tracker and the canonical angular momentum change, for the three beam line settings, are shown in figure 5.9. In each tracker, the shifts are predominantly caused by the correlations between the true phase space variables and the measurement errors. However, the shifts change sign between the two trackers, from positive in TKU to negative in TKD. The bias on the canonical angular momentum change is negative across all beam line settings, and its magnitude increases with beam emittance.

An additional bias is introduced by the linear approximation made to the vector potential. However, the even order derivatives of the on-axis longitudinal magnetic field with respect to z at the location of the two tracker reference planes are small. Therefore, the effect on the canonical angular momentum change is estimated be of the order of 10^{-5} MeV/c m, which can be considered negligible.

5.4.2 Uncertainties

The statistical uncertainty on the mean canonical angular momentum change originates from fluctuations in the stochastic processes that the beam undergoes and from fluctuations in the simulation used to calculate the systematic correction. The component that arises from the finite sampling of the stochastic processes is estimated by resampling the beams and calculating the bootstrapped 68.3% confidence intervals [98].

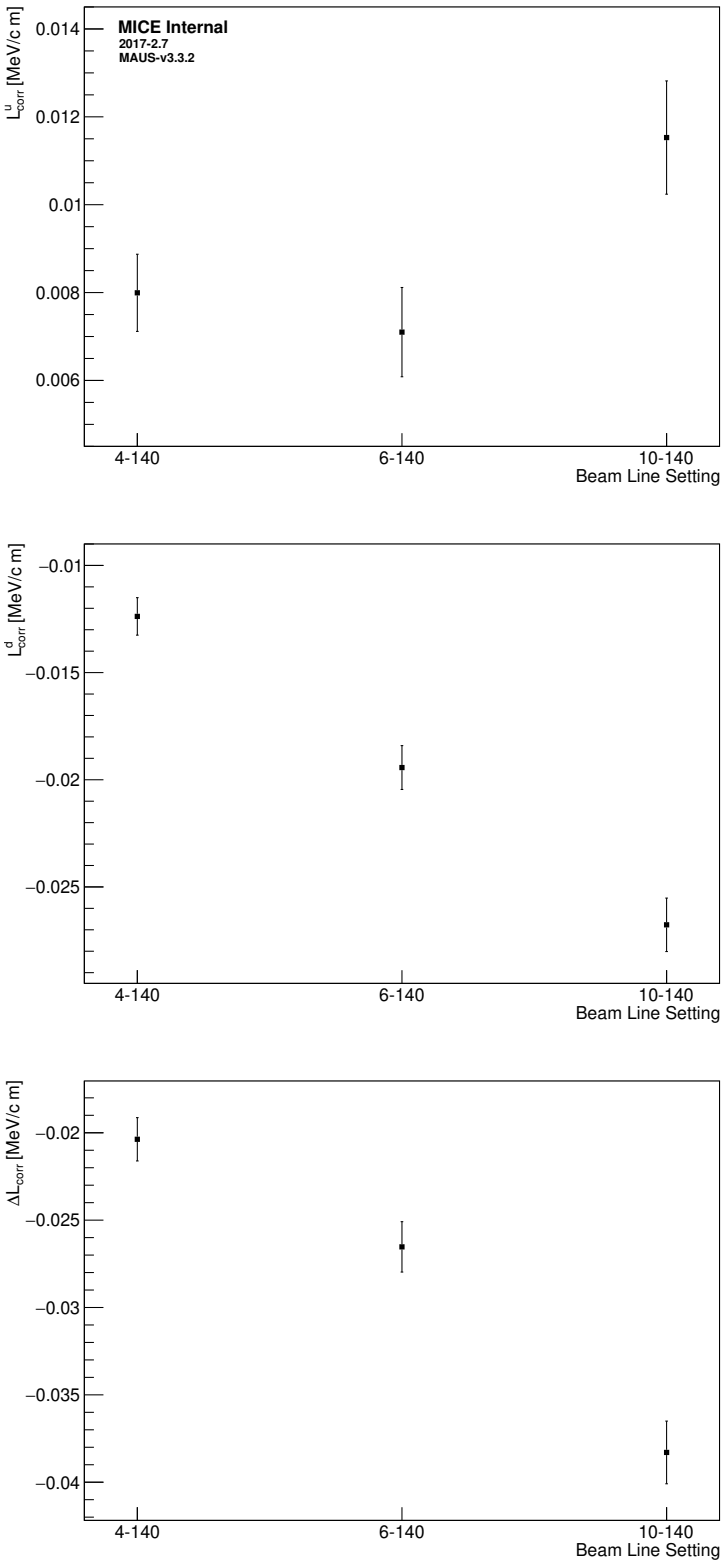

Figure 5.9: Systematic offsets on canonical angular momentum reconstruction in the (top) upstream and (centre) downstream trackers and on the (bottom) reconstructed canonical angular momentum change. The corrections are estimated for the three beam line settings.

The systematic uncertainty on the mean canonical angular momentum change is estimated using the simulations containing the detector system alterations presented in section 4.5.3. The variations that occur in the correction term due to the different alterations are presented in figure 5.10, for the three beam line settings. Those are added in quadrature to form the total systematic uncertainty on the measurement. Similar to the emittance case, the uncertainty on the solenoid field dominates. However, the effect due to the End1 Coil field variation is in this case larger than the one due to the Centre Coil.

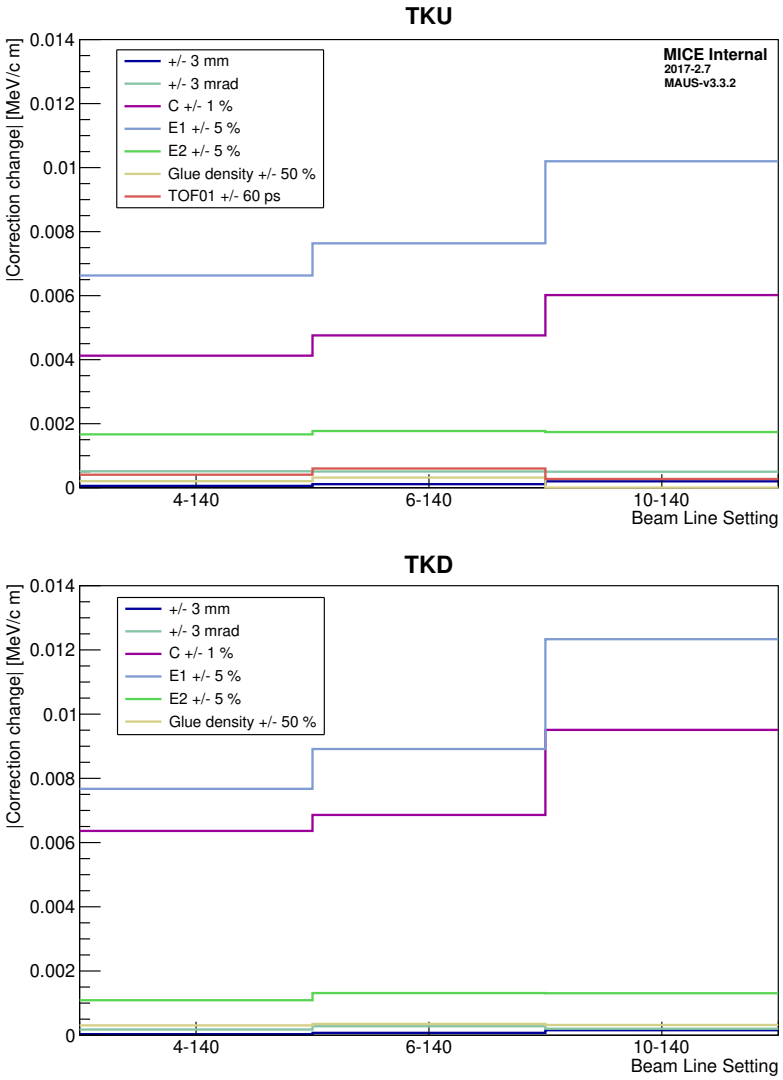

Figure 5.10: Systematic uncertainties on the canonical angular momentum change correction induced by (top) upstream tracker and TOF01 and (bottom) downstream tracker simulation alterations, for the three beam line settings.

5.4.3 Results

The means of the canonical angular momentum change distributions, corrected for the detector reconstruction offsets, are shown in table 5.1. The measurement uncertainty is dominated by the systematic uncertainty. No correction for analysing only a fully transmitted ensemble is applied.

	$\langle \Delta L_{canon} \rangle$ [MeV/c m]	
Beam Line Setting	Empty LH_2	Full LH_2
4-140	-0.0498 ± 0.0014 ± 0.0128	-0.0854 ± 0.0016 ± 0.0128
6-140	-0.0334 ± 0.0016 ± 0.0146	-0.0587 ± 0.0018 ± 0.0146
10-140	-0.0588 ± 0.0021 ± 0.0197	-0.1002 ± 0.0025 ± 0.0197
Beam Line Setting	No absorber	LiH
4-140	0.0033 ± 0.0014 ± 0.0128	-0.0321 ± 0.0017 ± 0.0128
6-140	-0.0362 ± 0.0015 ± 0.0146	-0.0427 ± 0.0018 ± 0.0146
10-140	-0.0420 ± 0.0022 ± 0.0197	-0.0745 ± 0.0029 ± 0.0197

Table 5.1: Measured mean canonical angular momentum change for 140 MeV/c momentum beams crossing the four different absorber configurations in the MICE 'flip mode' (2017-2.7 magnetic channel setting). The statistical errors are listed followed by the systematic errors.

The 'No absorber' and 'Empty LH_2' cases show a mean reduction, except for the '4-140', 'No absorber' data set. This effect can be explained by the presence of the aluminium windows. In the 'No absorber' configuration, the beam traverses one aluminium window placed just downstream of TKU and another one situated just upstream of TKD. The 'Empty LH_2' configuration contains the additional liquid hydrogen vessel windows. Any beam interactions with an absorber material in the upstream half of the MICE cooling channel lead to an increase in the mean canonical angular momentum, while the downstream counterparts of such interactions lead to a decrease. The net change is influenced by the interplay between the magnetic field, the beam size, and the mean canonical angular momentum and energy, as prescribed by equation 5.6.

It can be noted from the betatron function evolution presented in figure 4.23, that the size of the beam is larger in the region between the absorber centre and TKD than in the region between TKU and the absorber centre. As such, for any pair of aluminium windows, the beam size at the downstream window is larger. As the field has the same magnitude, but opposite polarity (negative), at the location

of the downstream window, the term in equation 5.6 proportional to $\frac{qB_z}{2}(\langle x^2\rangle + \langle y^2\rangle)$ causes a canonical angular momentum reduction which is larger in magnitude than the increase induced by the upstream window. Additionally, the term proportional to $-\langle L_{canon}\rangle$ causes a canonical angular momentum magnitude reduction in both the upstream and downstream windows.

When the liquid hydrogen and lithium hydride absorbers are placed in the path of the beam, an additional mean canonical angular momentum reduction is observed. This can be explained by two factors. First, a beam with positive mean canonical angular momentum is expected to undergo a reduction in this quantity, irrespective of the field, due to energy loss at the absorber. Second, the field and beam size dependent term generates a reduction in the downstream half of the absorber which is larger than the increase in the upstream half. This effect is caused by the relatively steep increase in beam size across the absorber region, as shown in the bottom panel of figure 4.23, combined with a decrease in beam energy.

For comparison, preliminary results from the MICE 'solenoid mode' analysis on the mean canonical momentum change show increases as large as 0.194 MeV/c m and 0.222 MeV/c m in the presence of the lithium hydride disk and the full liquid hydrogen vessel, respectively [100]. The results presented here demonstrate the potential of a cooling cell with flipped polarity magnetic field at the absorber to suppress the mean canonical angular momentum. A cooling section formed of an array of such cells could maintain the mean canonical angular momentum close to zero.

Chapter 6

Conclusions

The Muon Ionisation Cooling Experiment (MICE) was designed to demonstrate the feasibility of ionisation cooling as a technique to reduce the muon beam phase volume, and to provide the first measurement of normalised transverse emittance reduction in a muon beam. In MICE Step IV, the cooling cell consisted in an absorber module situated within a superconducting focusing coil. The trajectory and momentum of each muon were individually measured before and after passing through the absorber module by a pair of identical scintillating fibre trackers. The MICE solenoidal magnetic channel was capable to produce a longitudinal magnetic field that flipped polarity at the absorber. Known as the 'flip mode', this configuration was designed to avoid an increase in the magnitude of the canonical angular momentum at the absorber.

MICE reconstructed several million individual muon tracks passing through a liquid hydrogen or lithium hydride absorber, for a variety of magnetic channel settings and input beams. A first MICE analysis on muon cooling reported an increase in the number of low-amplitude muons, and in the beam phase space density for beams that traversed the absorber [22]. This work was focused on improving the measurement of the cooling signal and quantifying the effect of the 22 l liquid hydrogen and the 65 mm thick lithium hydride absorbers on the normalised transverse emittance of muon beams with 140 MeV/c momentum, in the MICE 'flip mode' configuration.

Inadequate beam matching into the upstream spectrometer solenoid resulted in a suboptimal beam betatron function at the absorber. This hindered the cooling signal measurement due to additional multiple Coulomb scattering in the absorber. A

novel beam selection technique based on rejection sampling and kernel density estimation was developed and used to obtain beam subsamples with a suitable betatron function, which improved the measurement of the cooling performance. Furthermore, the procedure enabled the selection of beams with specific input emittances, a feature that was exploited to gain insight into the equilibrium emittance of each absorber module.

The emittance change induced by the liquid hydrogen and the lithium hydride absorbers was measured for six properly matched beams with input emittances in the [1.5, 2.5, ..., 6.5] mm range. Emittance reduction was observed for beams with input emittance larger than ~ 2.5 mm, as shown in figure 4.42. The effect is growing linearly with the input emittance, and is a clear ionisation cooling signal. Moreover, the measurements are consistent with the simulations and the theoretical model derived from the cooling equation 2.52. The effective equilibrium emittances for the two absorber modules were estimated at 2.3 ± 0.5 mm (liquid hydrogen) and 2.6 ± 0.5 mm (lithium hydride).

This is the first direct measurement of normalised transverse emittance reduction of a muon beam via ionisation cooling. It demonstrates the viability of this novel cooling technique as a means to produce low-emittance muon beams. The demonstration of ionisation cooling by the MICE collaboration constitutes a substantial and encouraging breakthrough in the R&D efforts to deliver high-brightness muon beams suitable for a high intensity Neutrino Factory or a Muon Collider.

Additionally, a study of the beam canonical angular momentum change induced by the liquid hydrogen and the lithium hydride absorbers in the MICE 'flip mode' was conducted. The absorbers were found to produce a reduction in the positive mean canonical angular momentum of the beam, as presented in figure 5.7 and table 5.1. The measurement is well reproduced by the simulation. The canonical angular momentum increase in the upstream half of the absorber is superseded by a reduction of a larger magnitude in the downstream half. This effect is attributed to energy loss at the absorber, which is situated at the field polarity flip, combined with an increasing beam size across the absorber region. The result of this novel analysis confirms the potential of the field polarity flip as a tool to maintain a low-magnitude beam canonical angular momentum within the cooling stage of a future muon based facility.

Bibliography

[1] G. Aad et al. "Observation of a new particle in the search for the Standard Model Higgs boson with the ATLAS detector at the LHC". In: *Physics Letters B* 716.1 (2012), pp. 1–29. DOI: 10.1016/j.physletb.2012.08.020.

[2] S. Chatrchyan et al. "Observation of a new boson at a mass of 125 GeV with the CMS experiment at the LHC". In: *Physics Letters B* 716.1 (2012), pp. 30–61. DOI: 10.1016/j.physletb.2012.08.021.

[3] Z. Maki, M. Nakagawa, and S. Sakata. "Remarks on the Unified Model of Elementary Particles". In: *Progress of Theoretical Physics* 28.5 (1962), pp. 870–880. DOI: 10.1143/PTP.28.870.

[4] B. Pontecorvo. "Neutrino Experiments and the Problem of Conservation of Leptonic Charge". In: *Sov. Phys. JETP* 26.984-988 (1968), p. 165.

[5] C. M. Ankenbrandt et al. "Status of muon collider research and development and future plans". In: *Phys. Rev. ST Accel. Beams* 2 (8 Aug. 1999), p. 081001. DOI: 10.1103/PhysRevSTAB.2.081001.

[6] J. -P. Delahaye et al. *Muon Colliders*. 2019. DOI: 10.48550/arXiv.1901.06150.

[7] M. Boscolo, J. -P. Delahaye, and M. Palmer. "The future prospects of muon colliders and neutrino factories". In: *Reviews of Accelerator Science and Technology: Volume 10: The Future of Accelerators*. 2019, pp. 189–214. DOI: 10.1142/9789811209604_0010.

[8] S. Geer. "Neutrino beams from muon storage rings: Characteristics and physics potential". In: *Physical Review D* 57.11 (1998), p. 6989.

[9] K. Abe et al. "Constraint on the matter-antimatter symmetry-violating phase in neutrino oscillations". In: *Nature* 580 (2020), pp. 339–344. DOI: 10.1038/s41586-020-2177-0.

[10] S. Choubey et al. *International Design Study for the Neutrino Factory, Interim Design Report*. Tech. rep. 2011. DOI: 10.48550/arXiv.1112.2853.

[11] M. A. Palmer. "An Overview of the US Muon Accelerator Program". In: *Proceedings of COOL13, Murren, Switzerland* (2013).

[12] J. -P. Delahaye et al. *Enabling Intensity and Energy Frontier Science with a Muon Accelerator Facility in the US: A White Paper Submitted to the 2013 US Community Summer Study of the Division of Particles and Fields of the American Physical Society*. 2013. DOI: 10.48550/arXiv.1308.0494.

[13] P. Kyberd et al. *nuSTORM: Neutrinos from STORed Muons*. 2012. DOI: 10.48550/arXiv.1206.0294.

[14] R. D. Ryne et al. "Design Concepts for Muon-Based Accelerators". In: *Proc. 6th International Particle Accelerator Conference (IPAC'15), Richmond, VA, USA, May 3-8, 2015*. 2015, pp. 2633–2636. DOI: 10.18429/JACoW-IPAC2015-WEPWA057.

[15] D. Möhl et al. "Physics and technique of stochastic cooling". In: *Physics Reports* 58.2 (1980), pp. 73–102. DOI: 10.1016/0370-1573(80)90140-4.

[16] V. V. Parkhomchuk and A. N. Skrinskii. "Electron cooling: 35 years of development". In: *Physics-Uspekhi* 43.5 (2000), pp. 433–452. DOI: 10.1070/pu2000v043n05abeh000741.

[17] A. A. Kolomenski and A. N. Lebedev. *The Effect of Radiation on the Motion of Relativistic Electrons in a Synchrotron*. 1956. URL: https://cds.cern.ch/record/1241617/files/p447.pdf.

[18] S. Schröder et al. "First Laser Cooling of Relativistic Ions in a Storage Ring". In: *Physical Review Letters* 64.24 (1990), p. 2901. DOI: 10.1103/PhysRevLett.64.2901.

[19] A. N. Skrinskii and V. V. Parkhomchuk. "Methods of cooling beams of charged particles". In: *Sov. J. Particles Nucl.(Engl. Transl.)* 12.3 (1981), pp. 223–247.

[20] D. Neuffer. "Principles and Applications of Muon Cooling". In: *Part. Accel.* 14 (1983), pp. 75–90. URL: https://cds.cern.ch/record/142710/files/p75.pdf.

[21] *MICE Website*. URL: http://mice.iit.edu/.

[22] MICE Collaboration. "Demonstration of cooling by the Muon Ionization Cooling Experiment". In: *Nature* 578.7793 (2020), pp. 53–59. DOI: 10.1038/s41586-020-1958-9.

[23] J. Liouville. "Note sur la Théorie de la Variation des constantes arbitraires". In: *Journal de Mathématiques Pures et Appliquées* 3 (1838), pp. 342–349. URL: http://eudml.org/doc/234417.

[24] T. Kibble and F. H. Berkshire. *Classical Mechanics*. World Scientific Publishing Company, 2004.

[25] M. Conte and W. W. MacKay. *An Introduction To The Physics Of Particle Accelerators*. World Scientific Publishing Company, 2008.

[26] H. Wiedemann. *Particle Accelerator Physics*. 4th ed. Springer Nature, 2015. DOI: 10.1007/978-3-319-18317-6.

[27] E. D. Courant and H. S. Snyder. "Theory of the Alternating-Gradient Synchrotron". In: *Annals of Physics* 3.1 (1958), pp. 1–48. DOI: 10.1016/0003-4916(58)90012-5.

[28] E. T. Jaynes. *Probability Theory: The Logic of Science*. Cambridge University Press, 2003.

[29] G. Penn and J. S. Wurtele. "Beam Envelope Equations for Cooling of Muons in Solenoid Fields". In: *Physical Review Letters* 85 (2000), pp. 764–767. DOI: 10.1103/PhysRevLett.85.764.

[30] G. Penn. *Beam Envelope Equations in a Solenoidal Field*. Tech. rep. Muon Collider Note 71. 2000.

[31] R. C. Fernow and R. B. Palmer. "Solenoidal ionization cooling lattices". In: *Phys. Rev. ST Accel. Beams* 10.6 (2007), p. 064001. DOI: 10.1103/PhysRevSTAB.10.064001.

[32] R. C. Fernow et al. "Transverse cooling in the muon collider". In: *AIP Conference Proceedings*. Vol. 472. 1. 1999, pp. 233–242. DOI: 10.1063/1.58847.

[33] R. B. Palmer. "Emittance and Cooling Lecture II: Ionization Cooling". In: *MICE Collaboration Meeting 38* (2014).

[34] T. O. Raubenheimer, F. -J. Decker, and J. T. Seeman. "Beam Distribution Function after Filamentation". In: *Proceedings Particle Accelerator Conference*. Vol. 5. 1995, pp. 3291–3293. DOI: 10.1109/PAC.1995.505858.

[35] Dieter Möhl. "Sources of Emittance Growth". In: *CAS - CERN Accelerator School: Intermediate Accelerator Physics* (2006), pp. 245–270. DOI: 10.5170/CERN-2006-002.245.

[36] S. Turner. *CAS CERN Accelerator School 5th General Accelerator Physics Course*. 1994.

[37] G. Ha et al. *Bunch Shaping in Electron Linear Accelerators*. 2021. DOI: 10.48550/arxiv.2111.00520.

[38] A. J. Dragt. "Numerical third-order transfer map for solenoid". In: *Nuclear Instruments and Methods in Physics Research Section A: Accelerators, Spectrometers, Detectors and Associated Equipment* 298.1-3 (1990), pp. 441–459. DOI: 10.1016/0168-9002(90)90647-O.

[39] A. J. Dragt. *Lie Methods for Nonlinear Dynamics with Applications to Accelerator Physics*. 2019. URL: https://www.physics.umd.edu/dsat/docs/TOC12Nov2019.pdf.

[40] R. C. Fernow and J. C. Gallardo. "Muon transverse ionization cooling: Stochastic approach". In: *Physical Review E* 52.1 (1995), p. 1039. DOI: 10.1103/PhysRevE.52.1039.

[41] R. C. Fernow and J. C. Gallardo. "Validity of the differential equations for ionization cooling". In: *AIP Conference Proceedings*. Vol. 352. 1. 1996, pp. 170–177. DOI: 10.1063/1.49357.

[42] H. A. Bethe. "Molière's Theory of Multiple Scattering". In: *Physical Review* 89.6 (1953), p. 1256. DOI: 10.1103/PhysRev.89.1256.

[43] G. R. Lynch and O. I. Dahl. "Approximations to multiple Coulomb scattering". In: *Nuclear Instruments and Methods in Physics Research Section B: Beam Interactions with Materials and Atoms* 58.1 (1991), pp. 6–10. DOI: 10.1016/0168-583X(91)95671-Y.

[44] D. V. Neuffer and R. B. Palmer. "Progress toward a high-energy, high-luminosity μ^+-μ^- collider". In: *AIP Conference Proceedings*. Vol. 356. 1. 1996, pp. 344–358. DOI: 10.1063/1.49615.

[45] G. Gregoire et al. *Proposal to the Rutherford Appleton Laboratory: An International Muon Ionization Cooling Experiment (MICE)*. Tech. rep. MICE Note 21. 2003. URL: http://mice.iit.edu/mnp/MICE0021.pdf.

[46] MICE Collaboration. "Lattice design and expected performance of the Muon Ionization Cooling Experiment demonstration of ionization cooling". In: *Physical Review Accelerators and Beams* 20.6 (2017). ISSN: 24699888. DOI: 10.1103/PhysRevAccelBeams.20.063501.

[47] D. Rajaram and V. C. Palladino. "The Status of MICE Step IV". In: *Proc. 6th International Particle Accelerator Conference (IPAC'15), Richmond, VA, USA, May 3-8, 2015*. 2015, pp. 4000–4002. DOI: 10.18429/JACoW-IPAC2015-THPF122.

[48] D. J. S. Findlay. "ISIS-pulsed neutron and muon source". In: *2007 IEEE Particle Accelerator Conference (PAC)*. 2007, pp. 695–699. DOI: 10.1109/PAC.2007.4441104.

[49] C. N. Booth et al. "The design, construction and performance of the MICE target". In: *Journal of Instrumentation* 8.03 (2013), P03006. DOI: 10.1088/1748-0221/8/03/p03006.

[50] S. Blot et al. "Proton Contamination Studies in the MICE Muon Beam Line". In: *Particle Accelerator Proceedings*. 2011, pp. 4–9.

[51] MICE Collaboration. "The MICE Muon Beam on ISIS and the beam-line instrumentation of the Muon Ionization Cooling Experiment". In: *Journal of Instrumentation* 7.05 (2012), P05009. DOI: 10.1088/1748-0221/7/05/p05009.

[52] MICE Collaboration. "Pion contamination in the MICE muon beam". In: *Journal of Instrumentation* 11.03 (2016), P03001. DOI: 10.1088/1748-0221/11/03/p03001.

[53] V. Blackmore et al. "Particle Tracking and Beam Matching Through the New Variable Thickness MICE Diffuser". In: *Proceedings 2011 Particle Accelerator Conference (PAC'11)*. Vol. 28. 2011.

[54] B. Wang et al. "The Design and Construction of the MICE Spectrometer Solenoids". In: *IEEE Transactions on Applied Superconductivity* 19.3 (2009), pp. 1348–1351. DOI: 10.1109/TASC.2009.2018057.

[55] A. Bross. "Spectrometer solenoid plans for Step IV". In: *MICE Collaboration Meeting 44* (2016). URL: https://indico.cern.ch/event/485764/.

[56] H. Witte et al. "Partial return yoke for MICE-general concept and performance". In: *North American Particle Accelerator Conference (NA-PAC 13)*. THPBA09. 2013, pp. 1247–1249.

[57] S. Q. Yang et al. "The Mechanical and Thermal Design for the MICE Focusing Solenoid Magnet System". In: *IEEE Transactions on Applied Superconductivity* 15.2 (2005), pp. 1259–1262. DOI: 10.1109/TASC.2005.849556.

[58] V. Bayliss et al. "The liquid-hydrogen absorber for MICE". In: *Journal of Instrumentation* 13.09 (2018), T09008. DOI: 10.1088/1748-0221/13/09/t09008.

[59] P. Snopok, G. Kafka, and J. Cobb. "Solid Absorber Program Status for MICE Step IV". In: *Proceedings of IPAC2011, San Sebastián, Spain* (2011), p. 859. URL: https://accelconf.web.cern.ch/ipac2011/papers/mopz028.pdf.

[60] P. Snopok, D. Neuffer, and C. Rogers. *Polyethylene Wedge Absorber in MICE*. Tech. rep. MICE Note 507. 2017. URL: http://mice.iit.edu/mnp/MICE0507.pdf.

[61] M. Ellis et al. "The design, construction and performance of the MICE scintillating fibre trackers". In: *Nuclear Instruments and Methods in Physics Research Section A: Accelerators, Spectrometers, Detectors and Associated Equipment* 659.1 (2011), pp. 136–153. DOI: 10.1016/j.nima.2011.04.041.

[62] A. Dobbs et al. "The Reconstruction Software for the MICE Scintillating Fibre Trackers". In: *Journal of Instrumentation* 11.12 (2016), T12001. DOI: 10.1088/1748-0221/11/12/t12001.

[63] D0 Collaboration. "The upgraded D0 detector". In: *Nuclear Instruments and Methods in Physics Research A* 565 (2006), pp. 463–537. DOI: 10.1016/j.nima.2006.05.248.

[64] MICE Collaboration. "Performance of the MICE diagnostic system". In: *Journal of Instrumentation* 16.08 (2021), P08046. DOI: 10.1088/1748-0221/16/08/p08046.

[65] M. Bonesini. *The design of the MICE TOF0 detector*. Tech. rep. MICE Note 145. 2006. URL: http://mice.iit.edu/micenotes/public/pdf/MICE0145/MICE0145.pdf.

[66] R. Bertoni et al. *The construction and laboratory tests for MICE TOF0/1 detectors*. Tech. rep. MICE Note 241. 2008. URL: http://mice.iit.edu/micenotes/public/pdf/MICE0241/MICE0241.pdf.

[67] R. Bertoni et al. "The design and commissioning of the MICE upstream time-of-flight system". In: *Nuclear Instruments and Methods in Physics Research Section A: Accelerators, Spectrometers, Detectors and Associated Equipment* 615.1 (2010), pp. 14–26. DOI: 10.1016/j.nima.2009.12.065.

[68] R. Bertoni et al. *The construction of the MICE TOF2 detector*. Tech. rep. MICE Note 286. 2010. URL: http://mice.iit.edu/micenotes/public/pdf/MICE0286/MICE0286.pdf.

[69] M. Rayner. "The development of a novel technique for characterizing the MICE muon beam and demonstrating its suitability for a muon cooling measurement". PhD thesis (University of Oxford). 2011.

[70] L. Cremaldi et al. "A Cherenkov Radiation Detector with High Density Aerogels". In: *IEEE Transactions on Nuclear Science* 56.3 (2009), pp. 1475–1478. DOI: 10.1109/TNS.2009.2021266.

[71] M. Adinolfi et al. "The KLOE electromagnetic calorimeter". In: *Nuclear Instruments and Methods in Physics Research Section A: Accelerators, Spectrometers, Detectors and Associated Equipment* 482.1-2 (2002), pp. 364–386. DOI: 10.1016/S0168-9002(01)01502-9.

[72] MICE Collaboration. "The MICE Particle Identification System". In: *Nuclear Physics B-Proceedings Supplements* 215.1 (2011), pp. 316–318. DOI: 10.1016/j.nuclphysbps.2011.04.042.

[73] E. Overton. "Studies and Developments within the Muon Ionisation Cooling Experiment". PhD thesis (University of Sheffield). 2014.

[74] MICE Collaboration. "Electron-muon ranger: performance in the MICE muon beam". In: *Journal of Instrumentation* 10.12 (2015), P12012. DOI: 10.1088/1748-0221/10/12/p12012.

[75] MICE Collaboration. "A totally active scintillator calorimeter for the Muon Ionization Cooling Experiment (MICE). Design and construction". In: *Nuclear Instruments and Methods in Physics Research Section A: Accelerators, Spectrometers, Detectors and Associated Equipment* 732 (2013), pp. 451–456. DOI: 10.1016/j.nima.2013.08.026.

[76] R. Asfandiyarov et al. "MAUS: the MICE analysis user software". In: *Journal of Instrumentation* 14.04 (2019), T04005. DOI: 10.1088/1748-0221/14/04/t04005.

[77] T. J. Roberts and D. M. Kaplan. "G4beamline simulation program for matter-dominated beamlines". In: *2007 IEEE Particle Accelerator Conference (PAC)*. 2007, pp. 3468–3470. DOI: 10.1109/PAC.2007.4440461.

[78] S. Agostinelli et al. "GEANT4—a simulation toolkit". In: *Nuclear instruments and methods in physics research section A: Accelerators, Spectrometers, Detectors and Associated Equipment* 506.3 (2003), pp. 250–303. DOI: 10.1016/S0168-9002(03)01368-8.

[79] R. Brun and F. Rademakers. "ROOT—An object oriented data analysis framework". In: *Nuclear instruments and methods in physics research section A: accelerators, spectrometers, detectors and associated equipment* 389.1-2 (1997), pp. 81–86. DOI: 10.1016/S0168-9002(97)00048-X.

[80] R. Bayes et al. *Towards Revised Step IV MICE Optics in the Absence of M1 SSD*. Tech. rep. MICE Note 475. 2015. URL: http://mice.iit.edu/micenotes/public/pdf/MICE0475/MICE0475.pdf.

[81] A. Dobbs et al. *The Reconstruction Software for the MICE Scintillating Fibre Trackers*. Tech. rep. MICE Note 451. 2016. URL: http://mice.iit.edu/micenotes/public/pdf/MICE0451/MICE0451.pdf.

[82] C. J. Hunt. "High Precision Track Reconstruction and First Emittance Measurements in the MICE Step IV Cooling Channel". PhD thesis (Imperial College London). 2016.

[83] F. Drielsma. "Measurement of the increase in phase space density of a muon beam through ionization cooling". PhD thesis (University of Geneva). 2018.

[84] V. Blackmore and J. Tarrant. *As-Built Solenoid Coil Dimensions and Locations in MICE Step IV*. Tech. rep. MICE Note 464. 2015. URL: http://mice.iit.edu/micenotes/public/pdf/MICE0464/MICE0464.pdf.

[85] F. Garnier, P. A. Giudici, and F. Bergsma. "Magnet Measurement Device for MICE". In: *MICE Collaboration Meeting 29* (2011).

[86] J. Langlands. "Measuring and Modelling the Magnetic Field of the MICE Spectrometer Solenoids". PhD thesis (University of Sheffield). 2018.

[87] J. von Neumann. "Various Techniques Used in Connection with Random Digits". In: *National Bureau of Standards Applied Mathematics Series* 12 (1951), pp. 36–38.

[88] M. T. Wells, G. Casella, and C. P. Robert. "Generalized Accept-Reject sampling schemes". In: *A Festschrift for Herman Rubin*. Vol. 45. Institute of Mathematical Statistics, 2004, pp. 342–348. DOI: 10.1214/lnms/1196285403.

[89] B. W. Silverman. *Density Estimation for Statistics and Data Analysis*. 1st ed. Routledge, 1998. DOI: https://doi.org/10.1201/9781315140919.

[90] D. W. Scott. *Multivariate Density Estimation: Theory, Practice, and Visualization*. John Wiley & Sons, 2015.

[91] J. S. Marron and M. P. Wand. "Exact Mean Integrated Squared Error". In: *The Annals of Statistics* 20.2 (1992), pp. 712–736. DOI: 10.1214/aos/1176348653.

[92] C. Leroy and P. -G. Rancoita. *Principles of Radiation Interaction in Matter and Detection*. World Scientific, 2011.

[93] M. Green et al. *Does One Know the Properties of a MICE Solid or Liquid Absorber to Better than 0.3 Percent?* Tech. rep. MICE Note 155. 2006. URL: http://mice.iit.edu/micenotes/public/pdf/MICE0155/MICE0155.pdf.

[94] S. Lim et al. "Tensile behavior of friction-stri-welded Al 6061-T651". In: *Metallurgical and Materials Transactions A* 35.9 (2004), pp. 2829–2835. DOI: 10.1007/s11661-004-0230-5.

[95] G. Kafka, C. M. Lei, and Bross A. *Lithium Hydride Heat Conduction and Density Study*. Tech. rep. MICE Note 448. 2012. URL: http://mice.iit.edu/micenotes/public/pdf/MICE0448/MICE0448.pdf.

[96] C. Brown and C. Rogers. *Systematic Uncertainties in the lH2 absorber*. Tech. rep. MICE Note 524. 2018. URL: http://mice.iit.edu/micenotes/public/pdf/MICE0524/MICE0524.pdf.

[97] Particle Data Group. "Review of Particle Physics". In: *Progress of Theoretical and Experimental Physics* 2020.8 (2020), p. 083C01. DOI: 10.1093/ptep/ptaa104.

[98] T. J. DiCiccio and B. Efron. "Bootstrap Confidence Intervals". In: *Statistical science* 11.3 (1996), pp. 189–228. DOI: 10.1214/ss/1032280214.

[99] C. T. Rogers. *First Observation of Normalised Emittance Reduction through Ionisation Cooling*. Tech. rep. MICE Internal Note. 2019.

[100] T. W. Lord. "Transverse Emittance Change and Canonical Angular Momentum Growth in MICE 'Solenoid Mode' with Muon Ionization Cooling". In: *Proc. IPAC'21*. 2021. DOI: 10.18429/JACoW-IPAC2021-WEPAB277.

[101] J. H. Cobb. *Statistical Errors on Emittance Measurements*. Tech. rep. MICE Note 268. 2009. URL: http://mice.iit.edu/micenotes/public/pdf/MICE0268/MICE0268.pdf.

Appendix A

Statistical Error on the Emittance Change Measurement

The measurements of the upstream and downstream emittances in MICE are highly correlated as they are performed on the same sample of muons. As a result, the statistical error on the emittance change is expected to be less than the error obtained by the addition in quadrature of the individual emittance measurement errors. Here an analytical expression for the statistical error on the emittance change that includes the effect of the correlation is derived. This work follows and is built upon the framework developed in [101].

Let ϵ_u and ϵ_d be the normalised 4D emittances measured upstream and downstream of the absorber, and $\Delta\epsilon = \epsilon_d - \epsilon_u$ the emittance change caused by the absorber. Assuming that ϵ_u and ϵ_d are measured precisely, then the statistical error on the emittance change depends only on the stochastic processes that the beam is subjected to between the two measurements, i.e., scattering in the absorber. If no absorber is present, then the statistical error is zero.

Since the error cannot depend on the locations of the two measurements, it is convenient to consider that ϵ_u and ϵ_d are measured at an infinitely thin absorber. Furthermore, assuming a cylindrically symmetric beam with no $x - y$ coupling at the two measurement locations, the upstream and downstream emittances can be expressed as

$$\epsilon_u^2 = \frac{1}{(mc)^2}\left(\sigma_{xx}\sigma_{p_xp_x} - \sigma_{xp_x}^2\right) \tag{A.1}$$

and

$$\epsilon_d^2 = \frac{1}{(mc)^2}\left(\sigma_{xx}\sigma_{q_xq_x} - \sigma_{xq_x}^2\right) \tag{A.2}$$

where $q_x = \alpha p_x + s$ is the muon x momentum after the absorber, s is the momentum kick due multiple scattering in the absorber ($\langle s \rangle = 0$) and $(1-\alpha)$ is the fraction of the momentum lost in the absorber. Using the q_x definition, the variance $\sigma_{q_xq_x}$ and covariance σ_{xq_x} can be expressed as

$$\sigma_{q_xq_x} = \alpha^2\sigma_{p_xp_x} + 2\alpha\sigma_{p_xs} + \sigma_{ss}, \tag{A.3}$$

and

$$\sigma_{xq_x} = \alpha\sigma_{xp_x} + \sigma_{xs}. \tag{A.4}$$

The measured emittance change on a muon sample of size n can then be written as

$$\begin{aligned}\Delta\epsilon &= (mc)^{-1}[S_{xx}(\alpha^2 S_{p_xp_x} + 2\alpha S_{p_xs} + S_{ss}) - (\alpha S_{xp_x} + S_{xs})^2]^{1/2} \\ &\quad - (mc)^{-1}[S_{xx}S_{p_xp_x} - S_{xp_x}^2]^{1/2} \\ &= (mc)^{-1}(a-b),\end{aligned} \tag{A.5}$$

where S_{xx}, $S_{p_xp_x}$, S_{xp_x}, S_{p_xs}, S_{xs} and S_{ss} are the sample estimates of σ_{xx}, $\sigma_{p_xp_x}$, σ_{xp_x}, σ_{p_xs}, σ_{xs} and σ_{ss}, and the substitution in the last line is made for the brevity of the algebra. In the approximation that the variances and covariances are completely uncorrelated, the error on the emittance change can be calculated as

$$\begin{aligned}\sigma_{\Delta\epsilon}^2 &= \left(\frac{\partial\Delta\epsilon}{\partial S_{xx}}\right)^2 \mathrm{Var}(S_{xx}) + \left(\frac{\partial\Delta\epsilon}{\partial S_{p_xp_x}}\right)^2 \mathrm{Var}(S_{p_xp_x}) \\ &\quad + \left(\frac{\partial\Delta\epsilon}{\partial S_{ss}}\right)^2 \mathrm{Var}(S_{ss}) + \left(\frac{\partial\Delta\epsilon}{\partial S_{xs}}\right)^2 \mathrm{Var}(S_{xs}) \\ &\quad + \left(\frac{\partial\Delta\epsilon}{\partial S_{xp_x}}\right)^2 \mathrm{Var}(S_{xp_x}) + \left(\frac{\partial\Delta\epsilon}{\partial S_{p_xs}}\right)^2 \mathrm{Var}(S_{p_xs}),\end{aligned} \tag{A.6}$$

where the partial derivatives are

$$\frac{\partial\Delta\epsilon}{\partial S_{xx}} = \frac{1}{mc}\left(\frac{\alpha^2 S_{p_xp_x} + 2\alpha S_{p_xs} + S_{ss}}{2a} - \frac{S_{p_xp_x}}{2b}\right), \tag{A.7}$$

$$\frac{\partial \Delta\epsilon}{\partial S_{p_x p_x}} = \frac{1}{mc}\left(\frac{\alpha^2 S_{xx}}{2a} - \frac{S_{xx}}{2b}\right), \tag{A.8}$$

$$\frac{\partial \Delta\epsilon}{\partial S_{ss}} = \frac{1}{mc}\frac{S_{xx}}{2a}, \tag{A.9}$$

$$\frac{\partial \Delta\epsilon}{\partial S_{xs}} = \frac{1}{mc}\frac{-2(\alpha S_{xp_x} + S_{xs})}{2a}, \tag{A.10}$$

$$\frac{\partial \Delta\epsilon}{\partial S_{xp_x}} = \frac{1}{mc}\left[\frac{-2\alpha(\alpha S_{xp_x} + S_{xs})}{2a} + \frac{2S_{xp_x}}{2b}\right], \tag{A.11}$$

and

$$\frac{\partial \Delta\epsilon}{\partial S_{p_x s}} = \frac{1}{mc}\frac{2\alpha S_{xx}}{2a}. \tag{A.12}$$

The variance of a sample variance and the variance of a sample covariance are defined as

$$\mathrm{Var}(S_{ii}) = \frac{2}{n-1}\sigma_{ii}^2 \tag{A.13}$$

and

$$\mathrm{Var}(S_{ij}) = \frac{1+\rho_{ij}^2}{n-1}\sigma_{ii}\sigma_{jj}, \tag{A.14}$$

where ρ_{ij} is the correlation coefficient between the variables i and j. If the emittance measurements are performed at a beam waist, $S_{xpx} = 0$. Furthermore, since s is not correlated with x, nor p_x, the sample covariances S_{xs} and $S_{p_x s}$ are also vanishing. Substituting the equations A.7-A.14 in equation A.6 and replacing the sample variances (S_{ii}) and covariances (S_{ij}) with their expectation values (σ_{ii} and σ_{ij}) yields

$$\begin{aligned}\sigma_{\Delta\epsilon}^2 =& \frac{1}{mc}\left[\left(\frac{\alpha^2\sigma_{p_x p_x} + \sigma_{ss}}{2a} - \frac{\sigma_{p_x p_x}}{2b}\right)^2 \frac{2}{n-1}\sigma_{xx}^2 + \left(\frac{\alpha^2\sigma_{xx}}{2a} - \frac{\sigma_{xx}}{2b}\right)^2 \frac{2}{n-1}\sigma_{p_x p_x}^2\right. \\ &\left. + \left(\frac{\sigma_{xx}}{2a}\right)^2 \frac{2}{n-1}\sigma_{ss}^2 + \left(\frac{2\alpha\sigma_{xx}}{2a}\right)^2 \frac{1}{n-1}\sigma_{p_x p_x}\sigma_{ss}\right].\end{aligned} \tag{A.15}$$

The expression for the statistical error on the emittance change measurement can

be simplified to

$$\sigma_{\Delta\epsilon} = \left\{ \frac{1}{n-1} \left[\epsilon_u^2 + \epsilon_d^2 - \epsilon_u \epsilon_d \left(1 + \frac{\alpha^2 \epsilon_u^2}{\epsilon_d^2} \right) \right] \right\}^{-\frac{1}{2}} \tag{A.16}$$

The correlation between the upstream and downstream measurements is reflected in the negative term. In the absence of an absorber, i.e., $\alpha = 1$ and $\epsilon_u = \epsilon_d$, the error is zero.

The expression in equation A.16 was found to significantly underestimate the statistical errors for the reconstructed data and simulation. This effect can be attributed to the ideal nature of the model, which does not account for the statistical fluctuations inherent to the tracker measurement. Furthermore, a few of the model assumptions do not hold for the MICE beams. For example, the beams experience $x - y$ coupling in the trackers ($\sigma_{xp_y} \neq 0$), and $\alpha_\perp$ is not zero ($\sigma_{xp_x} \neq 0$) at the downstream reference plane. The analytical expression derived here was used only in the full transmission correction study, where the emittance change of the true simulation ensembles was measured at the absorber. For the reconstructed data and the reconstructed simulation ensembles, the statistical error on the emittance change was estimated using bootstrapped confidence intervals [98].

Appendix B

Beam Sampling

The 2-dimensional projections of the transverse beam phase space on the transverse position (x, y) and transverse momentum (p_x, p_y) subspaces, measured at the TKU and TKD reference planes are shown in section B.1 and B.2, respectively.

B.1 TKU - 2D projections

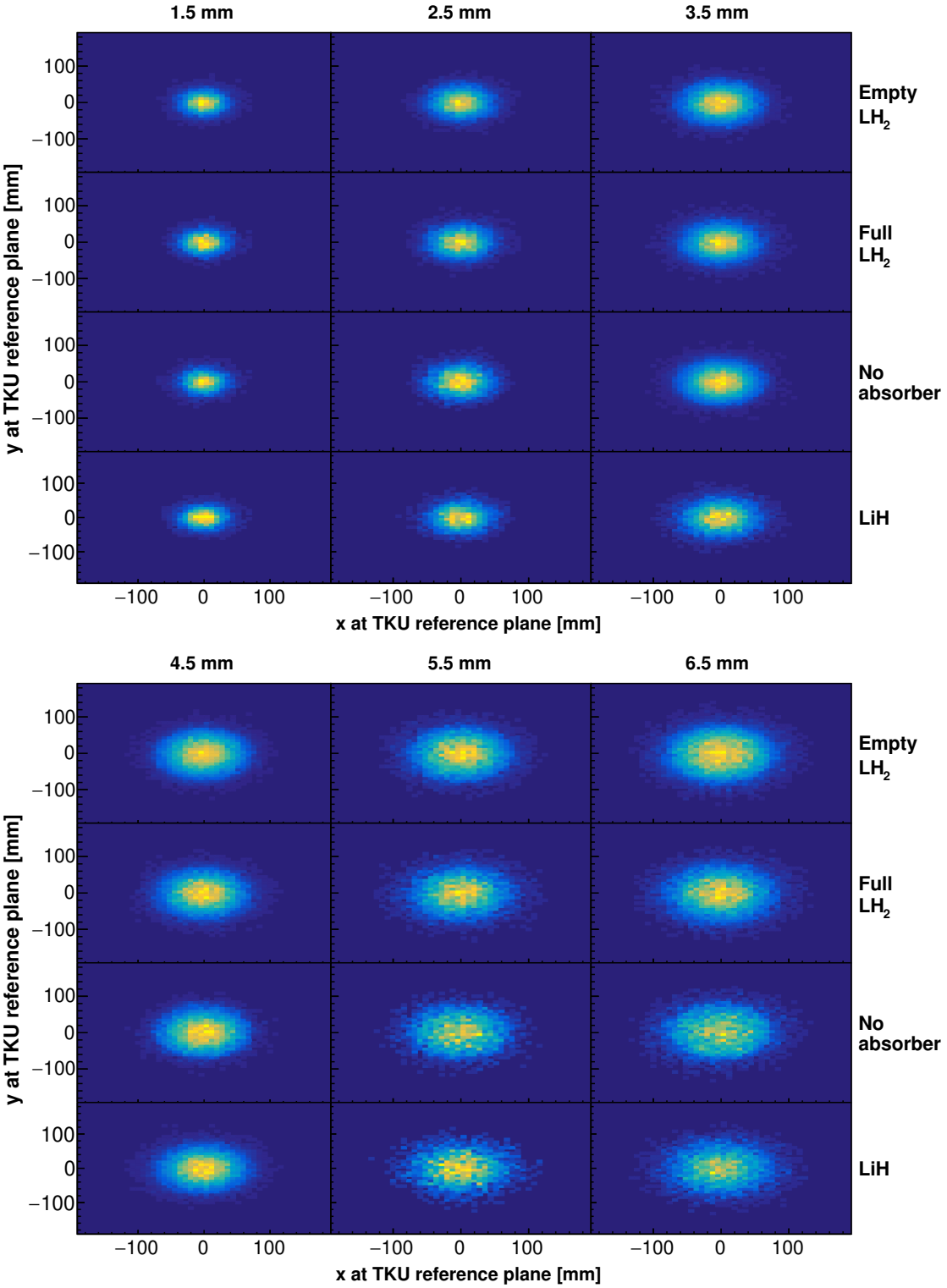

Figure B.1: Distribution of the events in (x, y) at the TKU reference plane for the six matched beams (reconstructed data).

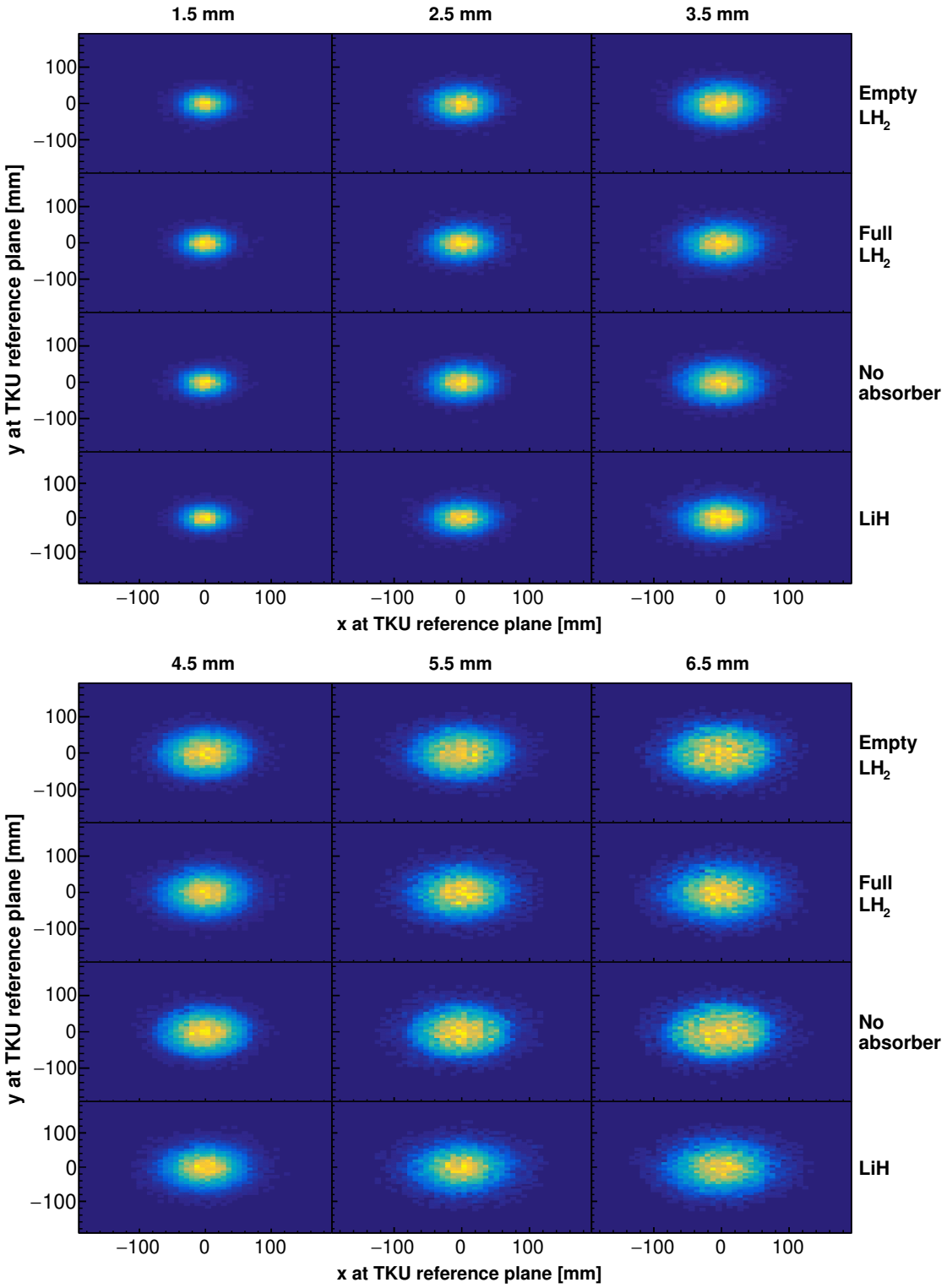

Figure B.2: Distribution of the events in (x, y) at the TKU reference plane for the six matched beams (reconstructed simulation).

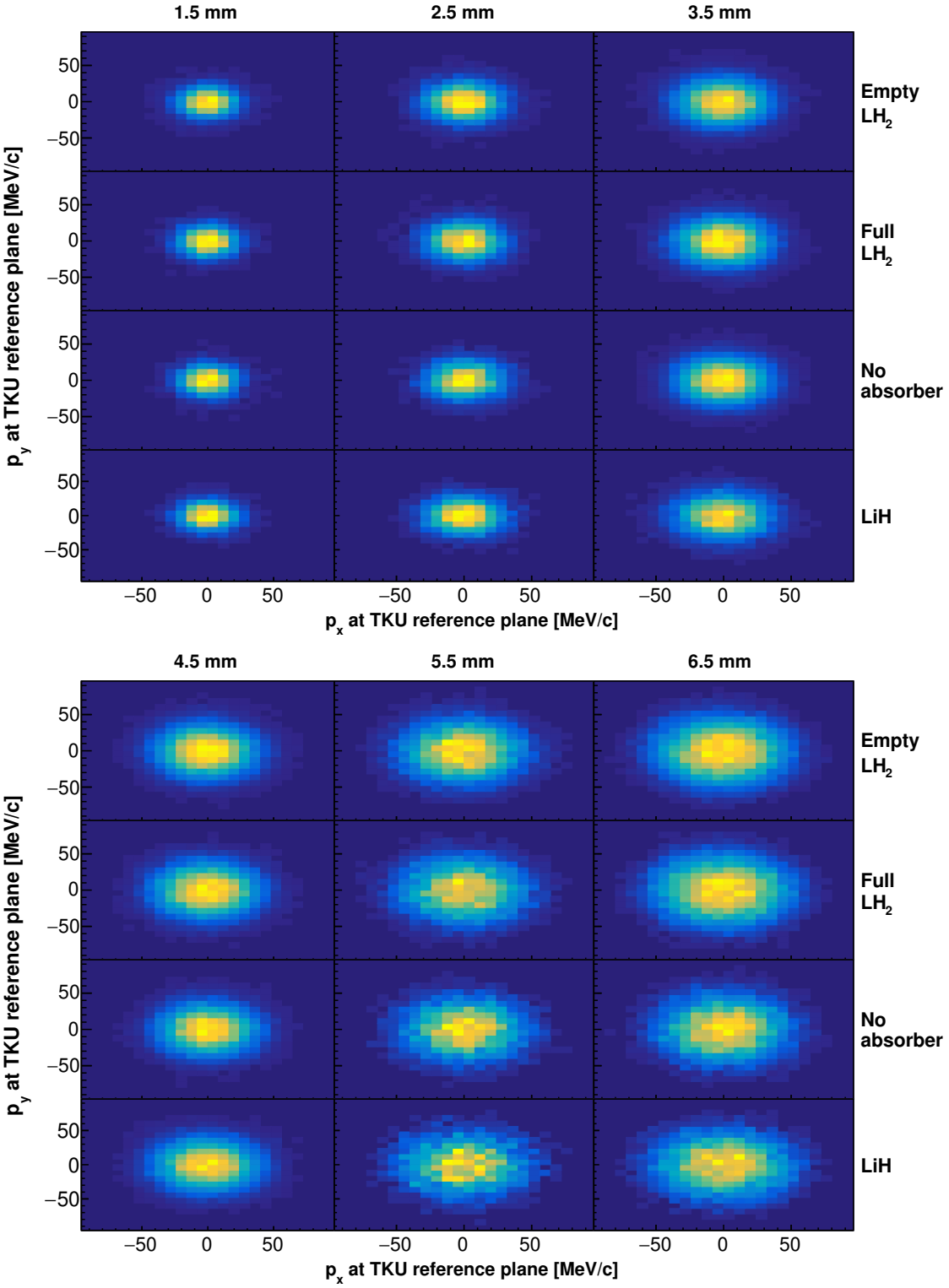

Figure B.3: Distribution of the events in (p_x, p_y) at the TKU reference plane for the six matched beams (reconstructed data).

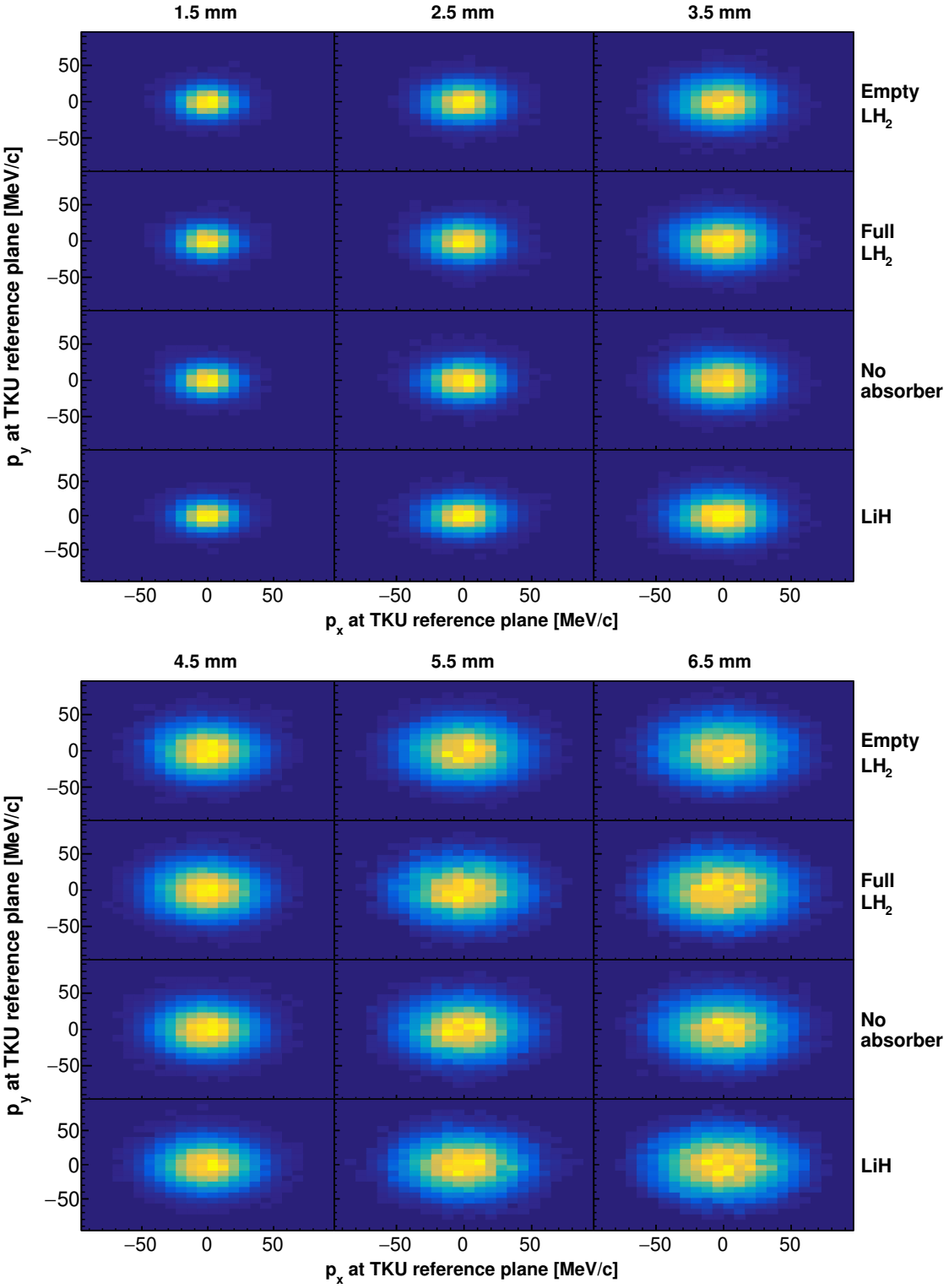

Figure B.4: Distribution of the events in (p_x, p_y) at the TKU reference plane for the six matched beams (reconstructed simulation).

B.2 TKD - 2D projections

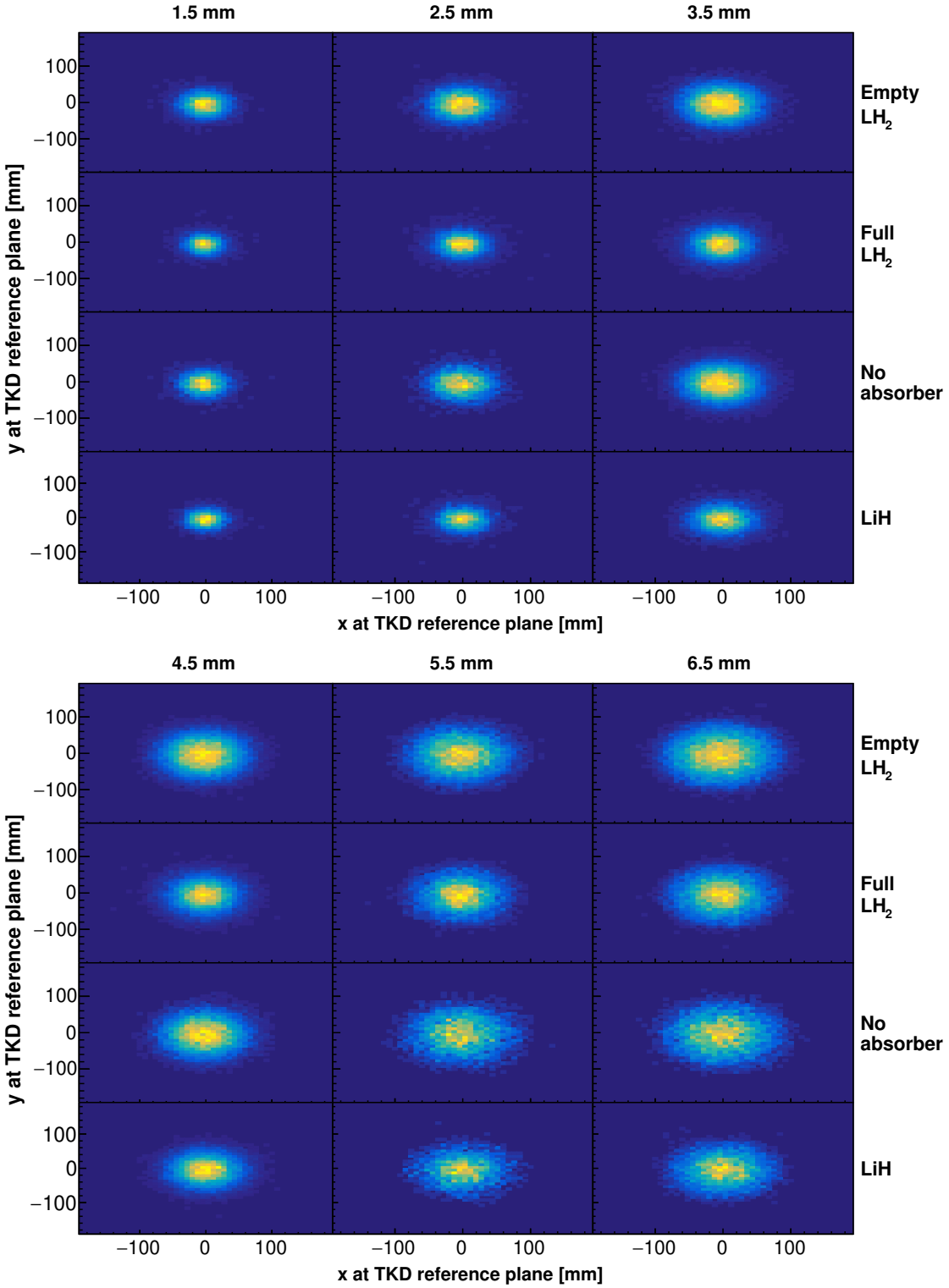

Figure B.5: Distribution of the events in (x, y) at the TKD reference plane for the six matched beams (reconstructed data).

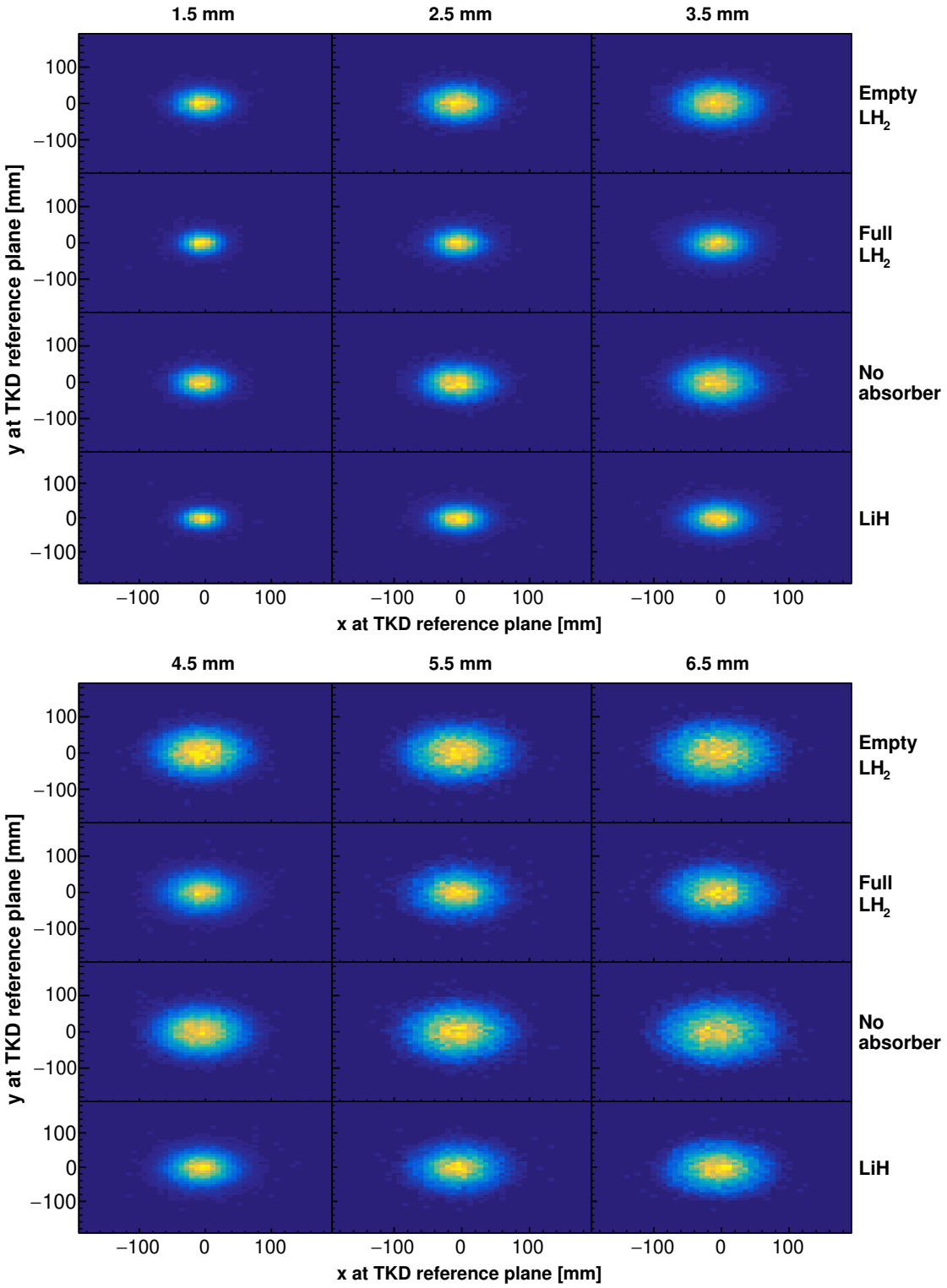

Figure B.6: Distribution of the events in (x, y) at the TKD reference plane for the six matched beams (reconstructed simulation).

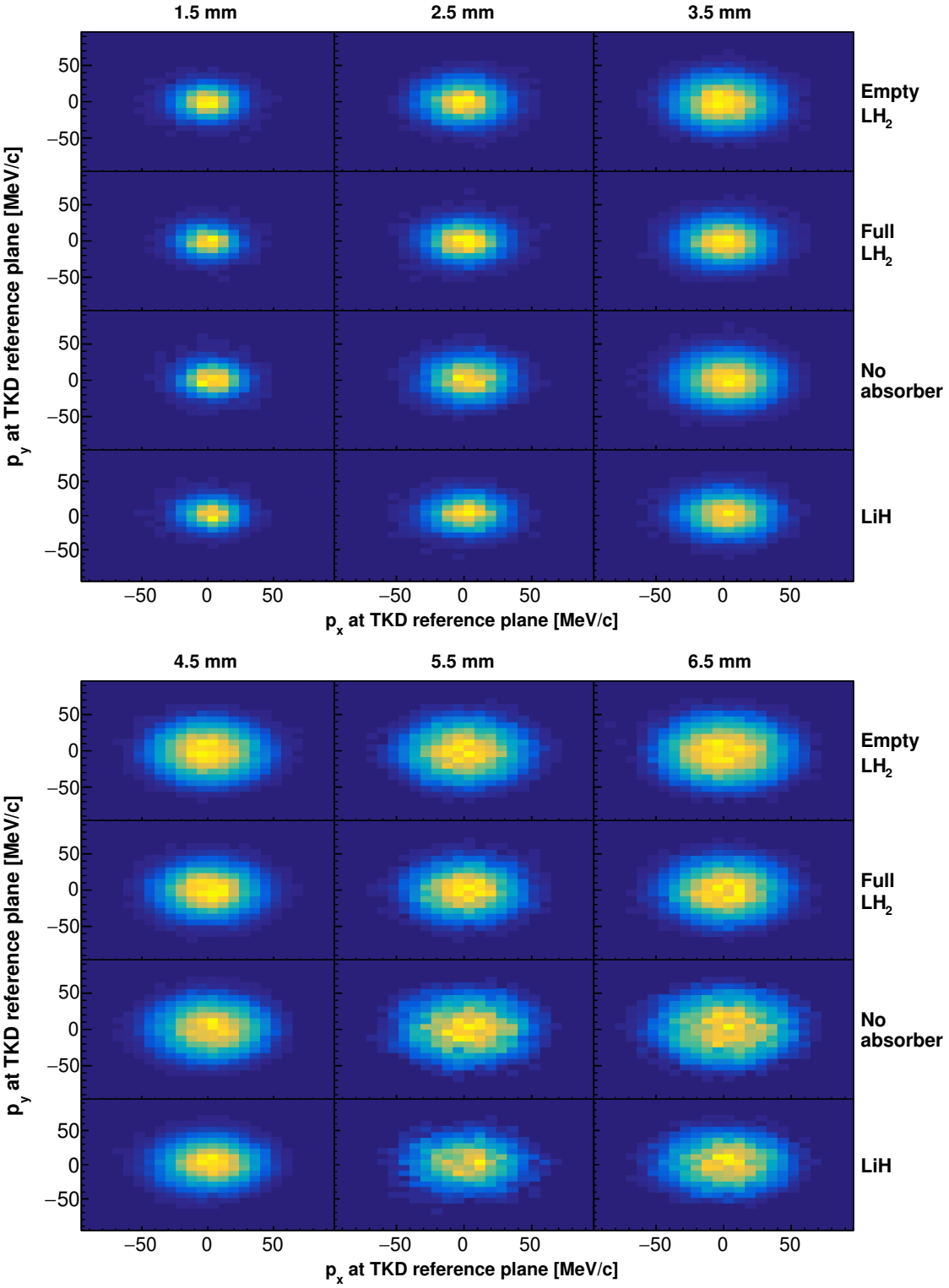

Figure B.7: Distribution of the events in (p_x, p_y) at the TKD reference plane for the six matched beams (reconstructed data).

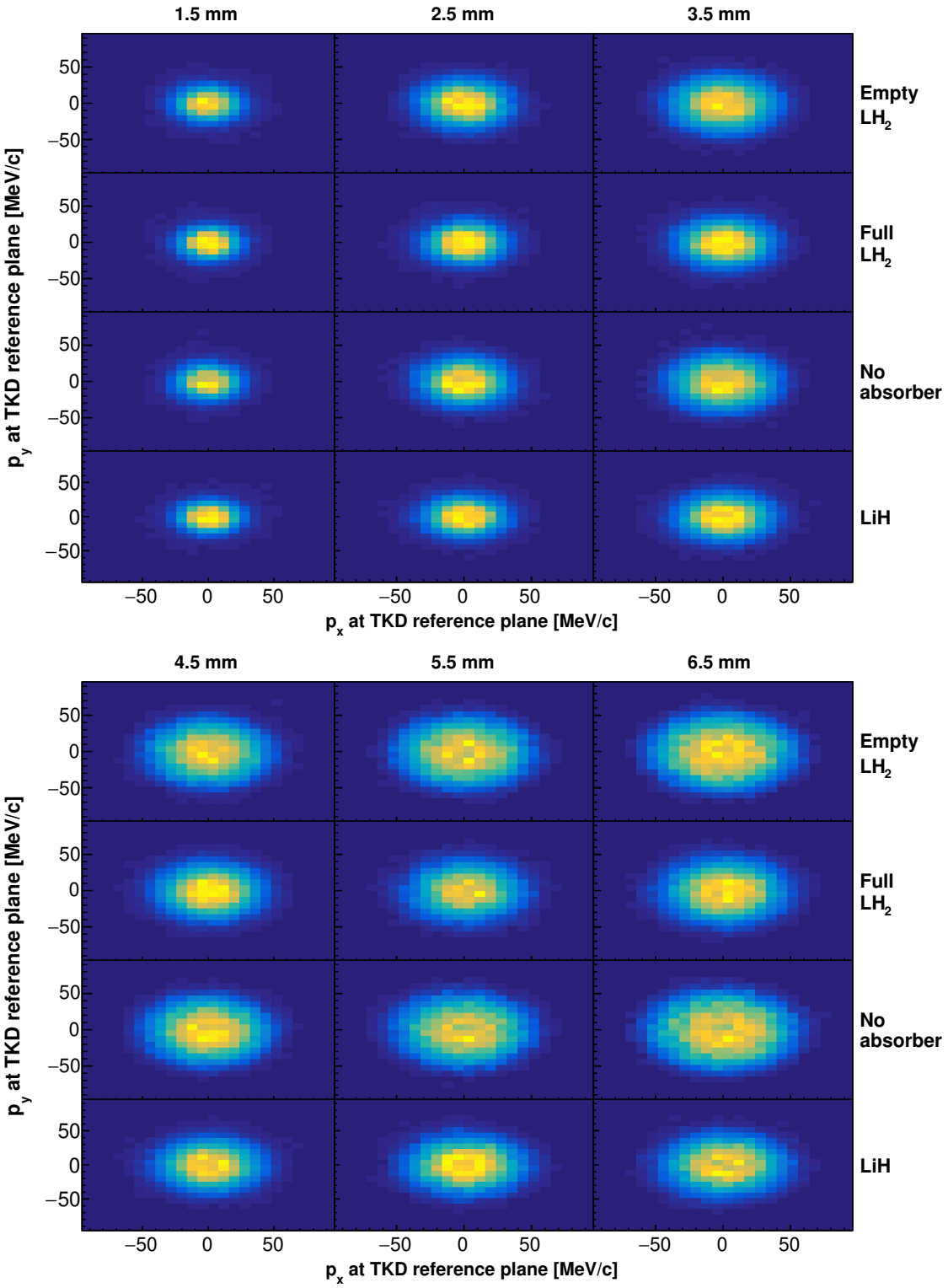

Figure B.8: Distribution of the events in (p_x, p_y) at the TKD reference plane for the six matched beams (reconstructed simulation).